A High Resolution Imaging Search for Brown Dwarf Companions Around High Mass Stars

by

Jasmine I Garani

A Thesis Presented in Partial Fulfillment
of the Requirements for the Degree
Master of Science

Approved May 2022 by the
Graduate Supervisory Committee:

Jennifer Patience, Chair
Molly Simon
Michael Line
Eric Nielsen

ARIZONA STATE UNIVERSITY

August 2022

ABSTRACT

This thesis presents the results of a brown dwarf companion direct imaging survey. Over a total of 4 nights, 200 B and A stars were imaged using the Keck telescope and the Near Infrared Camera 2 (NIRC2). Presented here are preliminary results from the nights of 04 June 2014 and 17 December 2013.

Brown dwarfs are partially degenerate objects that have masses between approximately 13 M_{Jup} and 75 M_{Jup}. Currently, the number of brown dwarf companions found around high mass stars is small. Finding brown dwarfs as companions to B and A stars will allow astronomers to study these objects when they are young and bright, giving key insights into their formation and evolution.

A pipeline was written specifically for these data sets that includes dark subtraction, flat field correction, bad pixel correction, distortion correction, centering, filtering, and point spread function (PSF) subtraction. This subtraction was accomplished using the Karhunen-Loéve Image Processing (KLIP) algorithm which employs principal component analysis and Karhunen-Loève (KL) transforms to subtract out starlight and artifacts from the images and allow for easier detection of a candidate companion.

Only candidate companions from the night of 04 June 2014 were analyzed, with 95 candidate companions found around 22 stars. Due to a lack of some necessary images, 91 companions around 20 stars were analyzed and their masses were found to be approximately 6 M_{Jup} to 150 M_{Jup} with projected separations from the host star of approximately 100AU to 900AU. An upper limit of 6.6% was placed on stellar companion frequency and an upper limit of 93% was placed on brown dwarf companion frequency. This survey achieved a median sensitivity of ΔK of 12.6 at 1" and a ΔK of 15.1 at 3.6". Further observations will be required to determine whether the candidates found are true co-moving companions or background stars not bound to

the host star.

DEDICATION

To my mom, dad, and sister.

ACKNOWLEDGMENTS

First, I would like to acknowledge and thank my committee, Dr. Jennifer Patience, Dr. Molly Simon, and Dr. Michael Line, as well as Dr. Hiliary Hartnett, Rebeccca Dial, Rebecca Polley, and Rose Petrini. Without these excellent members of SESE I would never have made it this far in my graduate career.

Next, I would like to acknowledge Eric Nielsen, who chose me to work for him through the SETI REU program in 2016. I started this project six years ago, and without his continual involvement I never would have finished it.

I also want to thank a number of the friends that I made while in SESE including Mara Karageozian, Mariah Heck, Logan Jensen, Marah Brinjikji, Em Waters, Austin Ware and Ed Buie II. You have all helped me through this journey and I truly appreciate your friendship. To those friends that I met outside of SESE, I want to say thank you to Rich and Aurora Jeanes and my other dojo mates for giving me a second home in Arizona. To my oldest friends, Kelsie Clearly and Brandy Blaise, thank you for sticking by me for all these years and encouraging me to pursue my goals.

I am also thankful for the many teachers I have had over the years including Sensei Steve Banchick and Sensei Dawn Croft. Sensei Steve, you gave me a lot of the life skills that I still use today and encouragement to achieve my goals. Sensei Dawn, you gave me a family when I moved to Arizona and the opportunity to continue my karate education.

Lastly and most importantly I want to thank my family. To my parents who have been super supportive of me throughout my whole life, I would not have made it through grad school without you. Thank you for always being proud of me. To my sister Tara, thank you for all our conversations and your stories. I am always happier after I talk to you, which has helped me a lot while in grad school.

TABLE OF CONTENTS

Page

LIST OF TABLES vii

LIST OF FIGURES viii

CHAPTER

1 INTRODUCTION 1

1.1 Overview of Brown Dwarfs 1

1.1.1 Brown Dwarf Overview 1

1.1.2 Discovery 4

1.1.3 Brown Dwarf Desert and Formation Models 4

1.2 B and A Stars 6

1.3 Mass-Age Degeneracy 9

1.4 Previous Surveys for Brown Dwarf Companions 10

1.5 Adaptive Optics 13

1.6 High-Contrast Imaging 15

1.7 Thesis Overview 17

2 OBSERVATIONS AND SAMPLE 18

2.1 Observations 18

2.2 Sample 20

3 DATA REDUCTION 24

3.1 Darks, Flats, Bad Pixels, and Distortion Correction 24

3.2 Centering and Smoothing 27

3.3 pyKLIP 28

4 RESULTS AND DISCUSSION 34

4.1 Results of Reduction 34

4.2 Separation Calculations 35

CHAPTER Page

4.3 Magnitude Difference Calculations 37
4.4 Mass Calculations 41
4.4.1 Absolute Magnitude Calculations 41
4.4.2 COND Model Interpolation 42
4.5 Attempted Reduction of 17 Dec 2013 44
5 SUMMARY AND FUTURE WORK 51
REFERENCES 54
APPENDIX
A STAR PROPERTIES FOR 04 JUNE 2014 AND 17 DEC 2013 60
B COMPANION PROPERTIES FOR 91 CANDIDATES FOUND FROM THE NIGHT OF 04 JUNE 2014 66
C POST pyKLIP IMAGES AND CONTRAST CURVES FOR ALL 04 JUNE 2014 STARS 70

LIST OF TABLES

Table Page

5.1 Proper Motions of Stars with Candidates from 04 June 2014 53

A.1 Star Properties 62

B.1 Candidate Companion Properties from 04 June 2014 67

LIST OF FIGURES

Figure		Page
1.1	Spectral Energy Distribution of a Brown Dwarf	2
1.2	Luminosity Evolution of Stars, Brown Dwarfs, and Planets	3
1.3	Brown Dwarf Desert	7
1.4	Color Magnitude Diagram	8
1.5	Multiplicity and Companion Frequency	9
1.6	Color-Magnitude Diagram of Brown Dwarfs	11
1.7	Stars Evolutionary Tracks	12
1.8	Benefits of Adaptive Optics	14
1.9	Adaptive Optics PSF	14
1.10	Adaptive Optics Diagram	16
2.1	NIRC2 Contrast Curve	20
2.2	Histogram of Star Distances	21
2.3	Color Magnitude Diagram of Sample	22
2.4	Age, Distance, and SpT of Sample	23
3.1	Raw and Dark Images	26
3.2	Flat Field	27
3.3	Types of Distortion	28
3.4	Image After Partial Reduction	29
3.5	pyKLIP Sections	32
3.6	Before and After pyKLIP	33
4.1	Before and After Reduction	36
4.2	Examples of 2 Candidate Companions	37
4.3	Magnitude Difference and Separations of Companions	38
4.4	Contrast Curve Examples	40

Figure Page

4.5 Magnitude Difference and Separation Contrast Curves 41
4.6 Saturated Stars Contrast Curves 42
4.7 Saturated vs. Unsaturated Stars 45
4.8 First Interpolation 46
4.9 Mass Interpolation 47
4.10 Mass vs. Projected Separation 48
4.11 Mass vs. Projected Separations Contrast Curves 49
4.12 17 December 2013 Rotation Problem 50
C.1 All Contrast Curves and Final Images 92

Chapter 1

INTRODUCTION

1.1 Overview of Brown Dwarfs

1.1.1 Brown Dwarf Overview

Brown dwarfs are partially degenerate objects that have masses between 13 and 75 M_{Jup}. Brown dwarfs are most luminous when they are young due to energy from gravitational collapse and brief deuterium burning. These objects are not massive enough to have stable hydrogen fusion like stars, so they continue to collapse until the electrons become partially degenerate and the degeneracy pressure prevents any further contraction (Basri, 2000; Burrows *et al.*, 2001). When they are bright, brown dwarfs are most easily observable in the infrared. The reason for this can be described by Wein's law which states that the peak wavelength of a black body is equal to 2900μm divided by temperature. This means that as the temperature decreases, the wavelength will increase. The minimum temperature that a star can be is approximately equal to 2900K (Dupuy and Liu, 2017), resulting in a peak wavelength around 1μm. Figure 1.1 shows the spectral energy distribution (SED) of brown dwarf 2MASS J14392839+1929150 (Filippazzo *et al.*, 2015). The blue portion starts around 1μm, which is approximately where the infrared part of the spectrum begins. Because as temperature decreases, the central wavelength increases, the lower the temperature of the brown dwarf, the more the peak of the SED moves into the infrared regime. Figure 1.1 demonstrates that many brown dwarfs peak in the infrared. Because of this, brown dwarfs are most commonly searched for and observed in the near-infrared wavelengths.

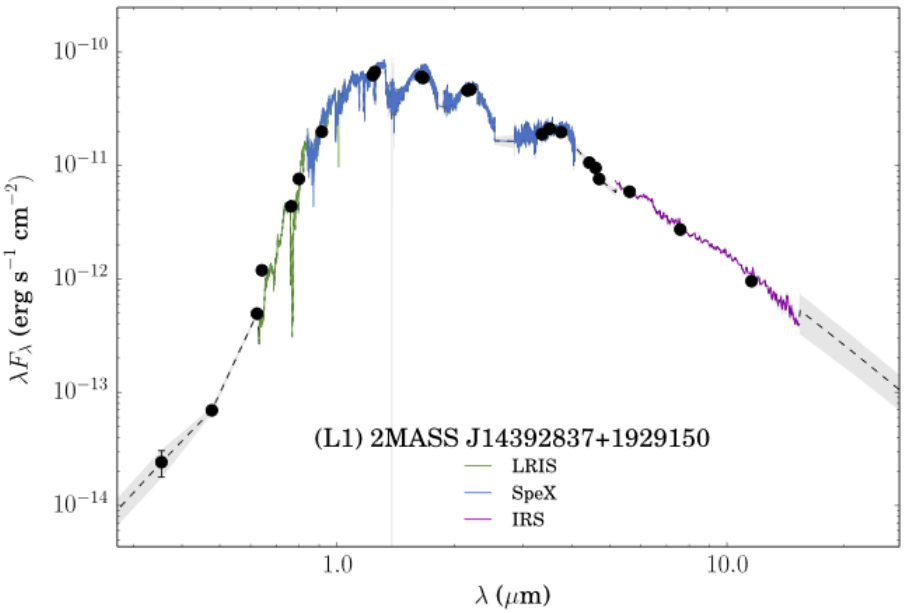

Figure 1.1: Spectral energy distribution of brown dwarf 2MASS J14392837+1929150. The distribution peaks in the near-infrared (NIR) shown by the blue data points, indicating that brown dwarfs are most luminous in this wavelength range. Because of this, brown dwarfs are usually observed in the NIR.

Brown dwarfs occupy the mass range between planets and stars, ranging in masses from approximately 13M$_{Jup}$ to 75M$_{Jup}$. The lower limit represents the division between planets and brown dwarfs and the upper limit represents the division between brown dwarfs and stars (Basri, 2000; Burrows *et al.*, 2001). Planets do not burn deuterium, and 13 M$_{Jup}$ is thought to be the minimum mass needed for deuterium burning (Basri, 2000; Burrows *et al.*, 2001). Due to insufficient mass, brown dwarfs are unable to burn hydrogen like stars (Basri, 2000; Burrows *et al.*, 2001). Stars fuse hydrogen while they are on the main sequence, which keeps their luminosities stable for long periods of time. Figure 1.2 shows how stellar, brown dwarf, and planetary luminosities change over time (Burrows *et al.*, 2001). Brown dwarfs, represented by the green lines, stay at a relatively constant luminosity for up to about 1.5 Gyrs, then the deuterium burning ceases and the brown dwarfs continuously cool over time. Planets

have no period of stable nuclear burning, therefore their luminosities dim immediately after formation.

Another method that has been used to distinguish brown dwarfs from low mass stars is the lithium test. Because brown dwarfs are fully convective, material is constantly moving between the core of the object and the atmosphere. Depending on spectral types, stars are generally hot enough at the core to burn lithium in approximately 100Myr. Many brown dwarfs, however, are too cool to burn lithium. Observations of brown dwarf atmospheres will show lithium to be present, while it will be absent from observations of stellar atmospheres (Basri, 1998, 2000; Burrows *et al.*, 2001).

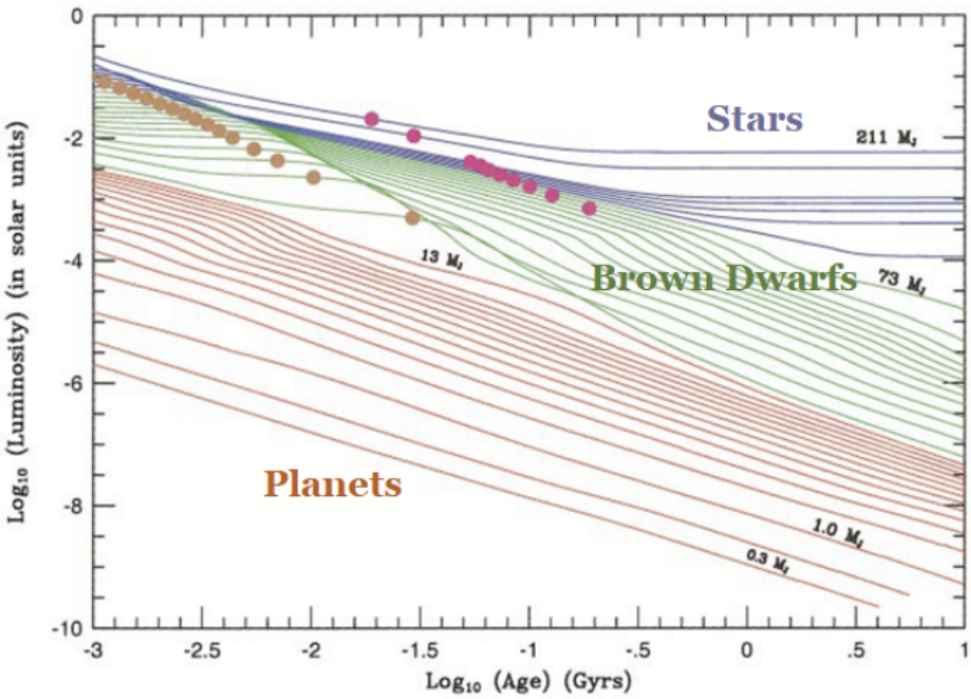

Figure 1.2: Luminosity evolution of stars, brown dwarfs, and planets. Stars cool until they start burning hydrogen and the temperature levels out while on the main sequence. Brown dwarfs maintain an approximately steady temperature during the deuterium burning phase. After this, they continuously cool. Planets cool continuously from their formation. (Adapted from Burrows *et al.* (2001)).

1.1.2 Discovery

Objects that we now know as brown dwarfs were first theorized as "black dwarfs" by Shiv S. Kumar in 1963 (Kumar, 1963). He used numerical models to show that there is a theoretical mass limit for stars to burn hydrogen and be on the main sequence. Stars below this limit contract until they become partially degenerate and never reach the main sequence (Kumar, 1963).

The theoretical prediction was confirmed by observations when the first brown dwarfs were identified in the 1990s with discoveries such as Teide 1, GL 299B, and three from the DEep Near-Infrared Survey (DENIS) (Rebolo *et al.*, 1995; Nakajima *et al.*, 1995; Delfosse *et al.*, 1997). Each of these brown dwarfs was found in a different environment. Teide 1 was found in the Pleiades Cluster (Rebolo *et al.*, 1995), GL 229B was found orbiting GL 229 (Nakajima *et al.*, 1995), and the three from the DEep Near-Infrared Survey (DENIS) were found in the field (Delfosse *et al.*, 1997). This thesis focuses on brown dwarfs that are companions to stars.

1.1.3 Brown Dwarf Desert and Formation Models

Figure 1.3a shows companions detected around solar-type stars with the radial velocity method where the middle gap is the so-called brown dwarf desert (Grether and Lineweaver, 2006). This desert is empirical from available data and not a theoretical hypothesis. The sample in this figure was corrected against biases and used criteria such as, surveys that did not focus on stellar companions, lack of close binaries in the surveys used, distance to the star, and separation of the star and it's companions to weed out the more biased observations. A complete explanation of how the sample was chosen is in Grether and Lineweaver (2006).

The middle area outlined in red in Figure 1.3b represents the lack of brown dwarfs,

and the sloping lines on either side show the trends for planets and stars as they change with mass. This suggests that planets and stars have two different formation mechanisms.

Recent research has started to change this idea of a lack of brown dwarfs as companions to stars. As more imaging surveys have been conducted with the intention of detecting brown dwarfs, surveys show that many brown dwarf companions do exist, but are at wider separations. The brown dwarf desert may only be < 0.2AU from the star (Troup *et al.*, 2016; Kiefer *et al.*, 2019). It is also possible that the lack of brown dwarfs in this range is not due to formation mechanisms, as would be suggested by Figure 1.3b (Grether and Lineweaver, 2006).

The formation mechanism for brown dwarfs is not entirely known, but it has been assumed that they form similarly to stars and their formation is what makes them orbit at large distances (Kiefer *et al.*, 2019). It is possible however, that dynamical interactions between the host star and a close companion such as tidal interactions are the cause for the wide separation brown dwarfs (Kiefer *et al.*, 2019). It has been thought that stars form through independent cloud collapse and planets form through core accretion (e.g. Troup *et al.* (2016)). Independent cloud collapse has also been thought to form brown dwarfs as well (Vorobyov and Basu, 2013). As the core of a cloud collapses, it heats up, which begins to form the center of a star. If the cloud is near or below the substellar mass limit, then it can form a substellar object such as a brown dwarf. However, this scenario may not be the most likely when looking at the volume density required in the cloud to form a brown dwarf mass object. In order for a cloud to be stable against gravitational collapse it must have a mass lower than what is known as the Jeans mass. In order to form a brown dwarf mass object at typical cloud temperatures, the necessary volume density to keep the mass of the cloud below the Jeans mass is closer to the volume densities of protostellar disks (Vorobyov

and Basu, 2013). This leads to the other possibility of brown dwarf formation; disk fragmentation. Disk fragmentation occurs when gravitational instability in a disk causes fragments to form that may become low mass stellar or substellar objects. Some models of this process are able to produce brown dwarf sized fragments but only at wide separations ($>\sim$170 AU), wider than the possible $<$0.2AU maximum of the brown dwarf desert (Boss, 2001; Vorobyov, 2013; Vorobyov and Basu, 2013). Recent studies have also tried to characterize the initial mass function (IMF) for brown dwarfs and stars (Gennaro and Robberto, 2020; Duchêne and Kraus, 2013). The IMFs produced by including the more recent information about brown dwarfs tend to produce continuous functions of companions with gradual variations, suggesting that high mass planets, brown dwarfs, and low mass stars may all form via the same mechanism (Gennaro and Robberto, 2020; Duchêne and Kraus, 2013). This thesis aims to observe more brown dwarfs at wider separations ($>$100AU) in order to measure occurrence rates, slope of the occurrence rate, and occurrence rate vs. semi-major axis in order to provide more data points for the empirical brown dwarf desert and more information for constructing formation models. As previously mentioned, the limit between planet and brown dwarfs is the deuterium burning limit, 13 M_{Jup}. By investigating formation mechanisms, a more robust distinction may be made between planets, brown dwarfs, and stars. It also may be possible to trace the deuterium limit to method of formation. One goal of this thesis work is to use the data gathered to inform these formation models and create this more detailed distinction.

1.2 B and A Stars

The objective of this survey is to detect brown dwarf companions around B and A stars, then measure occurrence rates and properties of the companions. B stars

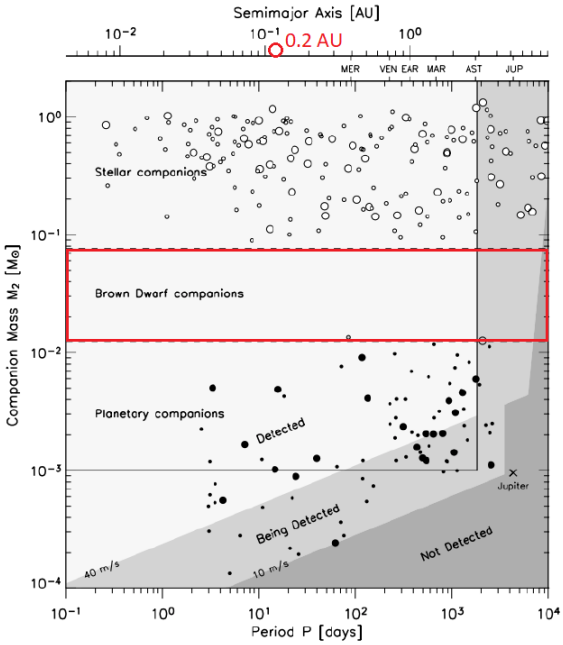

(a) Stellar, brown dwarf, and planetary companions detected with radial velocity before 2006. Red box is the brown dwarf desert and a separation of 0.2 AU is shown at the top. (Adapted by Grether and Lineweaver (2006).

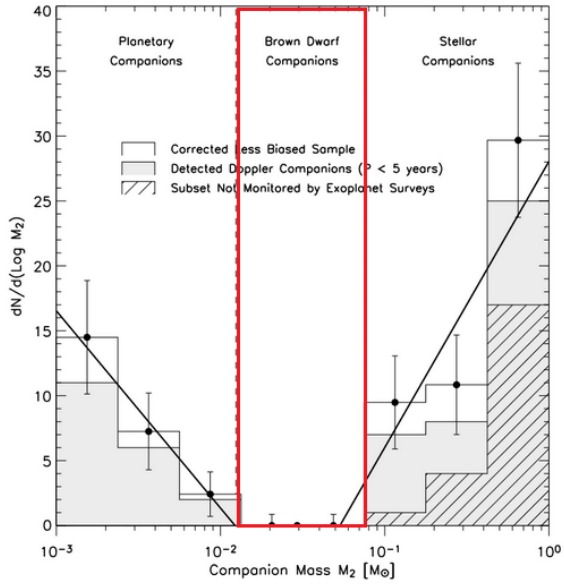

(b) Similar brown dwarf desert depiction with trends shown indicating two different formation models for planets and stars. Red box represents the brown dwarf desert. (Adapted from Grether and Lineweaver (2006).

Figure 1.3: Occurrence rates and measured parameters of companions from radial velocity surveys. This shows empirical evidence for the brown dwarf desert, as well as suggesting two different formation mechanisms for planetary and stellar companions based on the opposing slopes in Figure 1.3b.

have average effective temperatures between 10,500K and 30,000K and A stars have effective temperatures between 7,600K and 9,800K compared to the Sun's effective temperature of 5,777K (Carroll and Ostlie, 2017). Figure 1.4 shows a color magnitude diagram (CMD) of the main sequence from O-stars in the top left and Y-dwarfs in the bottom right (Pecaut and Mamajek, 2013). B-V color increases right across the x-axis while absolute magnitude increases up along the y-axis. B and A stars are on the high mass end of the spectral classes, younger, and have shorter life spans. Targeting younger stars is advantageous for detecting brown dwarfs through direct imaging, because the companion brown dwarf must be bright enough in the infrared to be visually seen in a telescope image. Since brown dwarfs cool over time, they will be brighter when the system is younger.

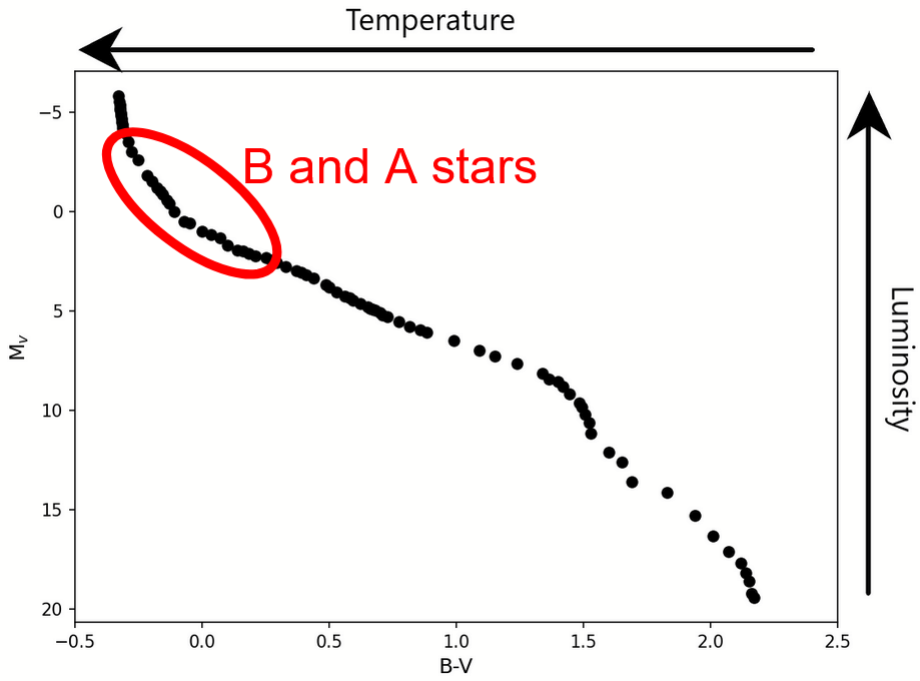

Figure 1.4: Color Magnitude Diagram (CMD) showing B and A stars in the upper left corner. Mass and temperature both increase left along the x-axis and luminosity increases upward along the y-axis (Pecaut and Mamajek, 2013).

B and A stars are also more likely to host stellar companions (Duchêne and Kraus,

2013; Raghavan *et al.*, 2010). In studies of stellar multiplicity (Duchêne and Kraus, 2013; Raghavan *et al.*, 2010) it has been shown that multiplicity fraction and companion fraction increase with increasing mass. Multiplicity fraction is the number of stars that host any number of companions. Companion fraction represents the number of companions that are hosted by each star. This trend of higher mass stars hosting a higher number of companions is shown in Figure 1.5 where the blue points represent multiplicity fraction and the red points represent companion fraction (Duchêne and Kraus, 2013).

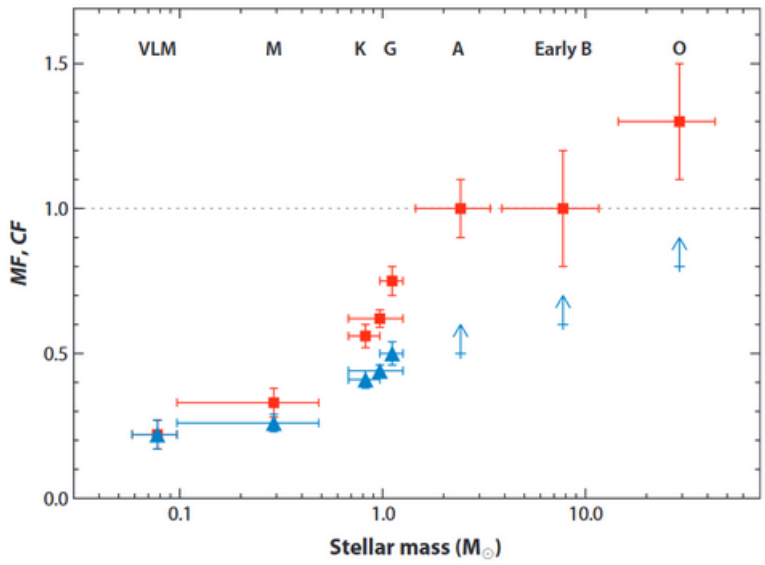

Figure 1.5: Multiplicity (blue) and companion (red) fractions for various spectral types. Multiplicity fraction represents the number of stars with at least one companion. Companion fraction represents the number of companions around the different types of stars. As the stars increase in mass, so does multiplicity and companion fractions, indicating that companions are more likely to be found around high mass stars (Adapted from Duchêne and Kraus (2013).

1.3 Mass-Age Degeneracy

As brown dwarfs evolve, they cool. Unlike stars, which are powered by a fusion source for much of their lives, most brown dwarfs do not follow the evolutionary track

of a typical black body. Figure 1.6 shows a CMD with theoretical isochrones for different mass brown dwarfs and their corresponding black bodies (Burrows *et al.*, 2001). The difference between the two is extremely apparent and creates a complication for measuring the ages and masses of brown dwarfs. Normally the ages of stars, which follow a black body evolutionary track, can be measured based on their place on a CMD. Because of the difference shown in this figure, it is difficult to determine the age and mass of an isolated brown dwarf. It is possible that the observed object is massive and old or young with a low mass. This problem lessens when the brown dwarf is part of a binary system where the host is a stellar object since it is possible to determine the age and mass of a star using its temperature, luminosity, spectra, or location on the HR-diagram, etc. Figure 1.7 shows another CMD for isochrones of A stars and demonstrates the evolutionary tracks of A stars moving off the main sequence (De Rosa *et al.*, 2013). If focus is put just on the solid lines, the lowest purple lines are the zero age main sequence A stars. Each line represents stars of different ages and stars with different positions on each line will have different masses. This figure assumes the same metallicity for all stars. As stars age, they will move right across the diagram and evolve off the main sequence. Position on such a diagram allows for the determination of the age of an A star. The age of the brown dwarf is assumed to be the age of the star it is orbiting. With brown dwarf evolutionary models (e.g. Baraffe *et al.* (2003)) the mass of the companion can be determined based on age and magnitude.

1.4 Previous Surveys for Brown Dwarf Companions

To date, only a few surveys have looked for or studied brown dwarfs with wide separations around higher-mass B and A stars. One companion search of A stars is the Volume-limited A-STar (VAST) survey, which observed 435 A stars within 75pc

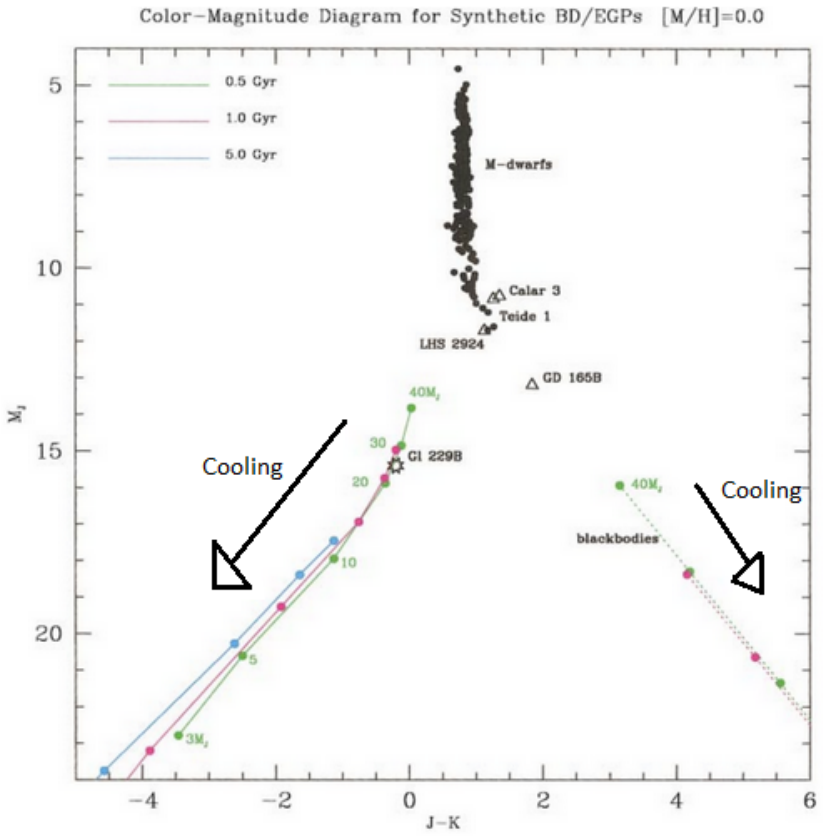

Figure 1.6: A color-magnitude diagram for modeled brown dwarfs vs. black bodies of the same mass. Brown dwarfs do not follow the path of the black body as it cools, which makes it difficult to determine it's age. Brown dwarfs on these paths can either be old with a high mass, or young with a low mass. (Adapted from Burrows *et al.* (2001)).

(De Rosa *et al.*, 2013). This survey, however, did not achieve a high enough sensitivity to image brown dwarf companions, only stellar companions. Two other surveys that observed companions around B and A types stars are the Gemini NICI Planet-Finding Campaign (henceforth referred to as NICI Campaign) (Nielsen *et al.*, 2013) and the Gemini Planet Imager Exoplanet Survey (GPIES) (Nielsen *et al.*, 2019). The NICI campaign searched for planets around 70 young B and A stars within 172pc, though most of the targets were within 100pc. The survey did not find any planets, but did detect 5 brown dwarf and low mass stellar companions. The campaign concluded that

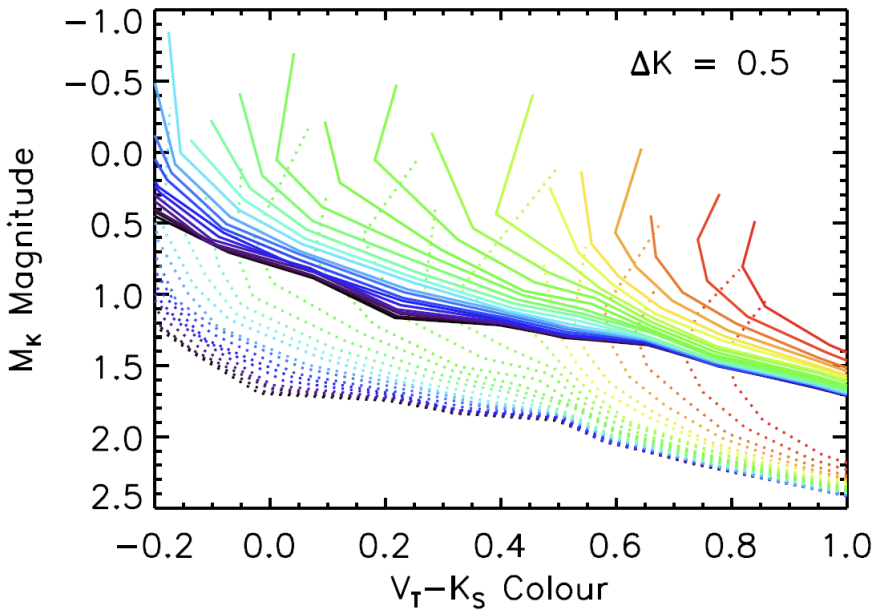

Figure 1.7: Isochrones for A star evolutionary tracks. Focusing on the solid lines, the bottom most lines (purple) represent the zero age main sequence. Each color represents a different age, and stars at different positions on each line will have different masses. As a star ages it moves from left to right across this figure. Position of a star on this CMD allows for the determination of that star's age. (Adapted from De Rosa *et al.* (2013)).

less than 10% of $2M_{\odot}$ stars host objects with masses larger than $10M_{Jup}$ at separations between 38 and 650 AU. The GPIES was able to detect 6 planetary mass companions along with 3 brown dwarfs. These detections come from the analysis of the first 300 stars in this survey, which are within 200pc and have spectral types of B, A, F, G, and K. With these results, the survey found that stars more massive than $1.5M_{\odot}$ are more likely to host planetary mass companions (5-$13M_{jup}$) at wider separations of 10-100AU than lower mass stars (Nielsen *et al.*, 2019). The calculated occurrence rate of planets around high mass stars from this survey is $9^{+5}_{-4}\%$, while the occurrence rate of brown dwarfs around all stars at these wider separations is a much smaller at $0.8^{+0.8}_{-0.5}\%$. GPIES also concluded that based on the brown dwarfs imaged, the most likely formation scenario for these objects is either core accretion or gravitational

instability. The substellar objects imaged are largely coplanar with their star's debris disk, indicating that they did form in the disk and not in the molecular cloud. GPIES was also able to conclude from parameter fitting that planets and brown dwarfs with separations between 10 and 100 AU follow different underlying distributions, so were likely formed through different mechanisms. With more observations, especially at separations beyond 100AU, as this survey will provide, more information can be added to these models in order to more tightly constrain formation scenarios and differences between brown dwarfs and planets.

1.5 Adaptive Optics

This survey uses direct imaging to detect companion brown dwarfs. Many such surveys use two main components, a camera system and an adaptive optics system. A simple camera system with no adaptive optics is mainly limited in image resolution by the ability of the telescope to see through the atmosphere (often called seeing-limited observations). Due to the fact that the atmosphere is always changing, more than just a higher altitude observation is needed to overcome the seeing limit. Figure 1.8 shows two images of the same object with and without adaptive optics (AO) from the same telescope (Beckers, 1993). Only with the AO system can the binary objects be resolved because it can correct for the atmospheric turbulence (often called diffraction-limited observations) (Beckers, 1993). The diffraction limit of a telescope is the theoretical resolution limit, which is proportional to wavelength and inversely proportional to diameter (Hampson *et al.*, 2021). With an AO system, the instrument can correct for enough of the atmospheric interference to approach this diffraction limit. Without adaptive optics, the resolution is limited by r_0, the scale of the atmospheric turbulence, and by τ_0, the time for the atmosphere to move a distance of r_0. When resolving two close objects, the narrower the PSF, the better resolution that can be achieved. Figure

1.9 shows that without an AO system, the PSF of an object is much wider than with an AO system (Beckers, 1993). Adaptive optics systems have allowed astronomers to observe faint companions as close as 10 AU to their bright host stars (Beckers, 1993).

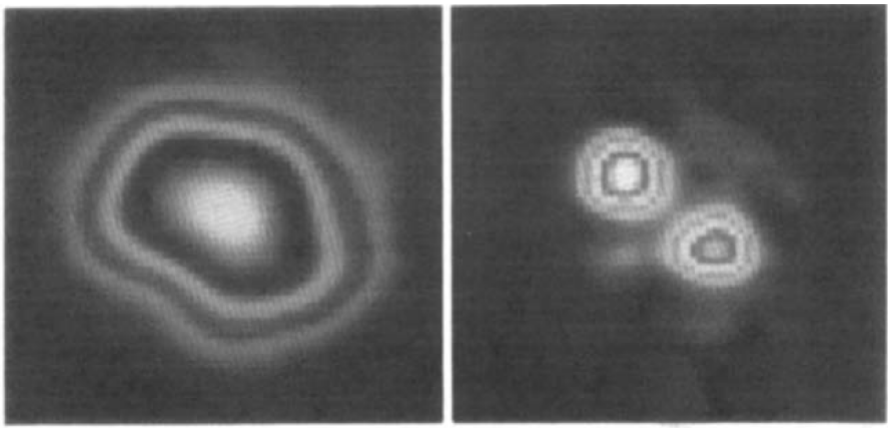

Figure 1.8: These two images show a binary observed with the same telescope with the AO system off (left) and the AO system on (right). The binary can only be resolved with use of the AO system, showing the capabilities and necessity of adaptive optics (Beckers, 1993).

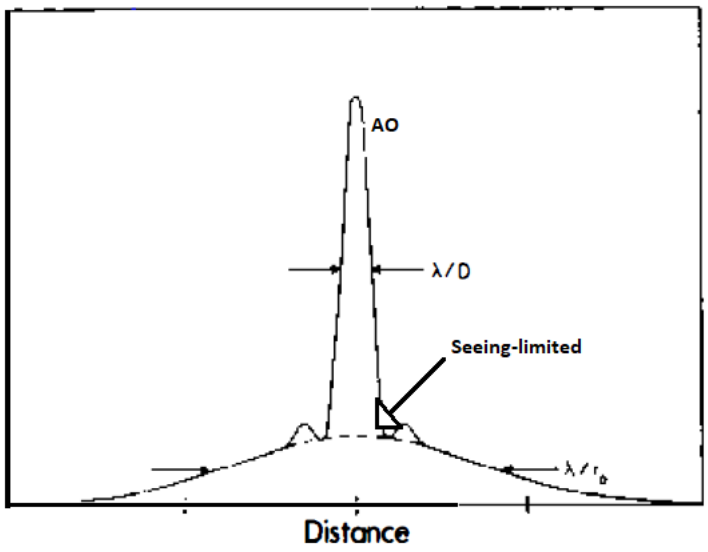

Figure 1.9: The difference in a star's PSF with (solid line) and without (dashed line) the use of an AO system. The lines over lap on the outskirts of each PSF, and the peak is in the same place, but the PSF with an AO system peaks much higher and is much narrower than the PSF without an AO system. (Adapted from Beckers (1993)).

AO systems work by correcting the incoming wavefront based on data collected from the atmosphere at that moment by looking at a guide star. As light moves through the atmosphere, it encounters areas where the indices of refraction change, leading to wavefronts that are delayed with respect to one another. As light enters a telescope with an AO system it first encounters a deformable mirror (shown in Figure 1.10). This mirror is programmed by a computer which calculates the necessary counter wave to correct the incoming wavefront. Some of the incoming light is directed through a wavefront sensor by a beam splitter, which measures the atmospheric disturbance using a bright star or object in the field. These measurements are translated through the computer to the deformable mirror. The incoming wavefronts are then corrected by the deformable mirror so they are flat, or all in the same phase, and go through the detector to be constructed into an image (Hampson *et al.*, 2021). The two main limitations of an AO system are the speed at which it can measure and apply the corrections before the atmosphere changes and the number of actuators on the deformable mirror that counteract the wavefront distortions. The time during which the atmosphere stays the same is described by the τ_0 parameter and the scale of the turbulence is the r_0 parameter. These parameters are both largest in the infrared wavelengths, especially in the K- and L- bands (Beckers, 1993), making them the most ideal wavelengths for observing close brown dwarf companions.

1.6 High-Contrast Imaging

Contrast is the ratio of the intensity of light between two objects. High-contrast imaging is necessary when trying to resolve an object that is in close proximity to another object that is at least 10^5 times brighter (Oppenheimer and Hinkley, 2009). Contrasts up to 10^{14} are often required to detect planetary and brown dwarf mass companions (Nielsen *et al.*, 2013) and the images taken are dominated by the light

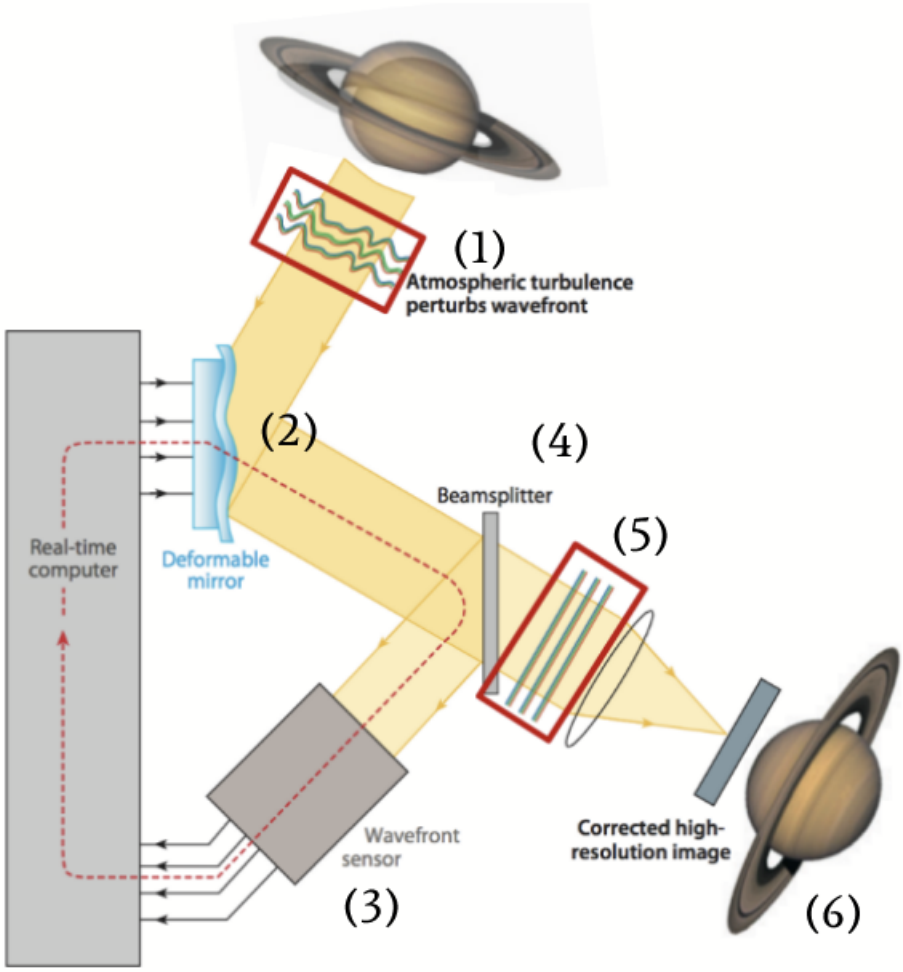

Figure 1.10: Schematic drawing of how an AO system works to produce an image with better resolution than what first enters the telescope. (1) Wavefront distorted by atmospheric turbulence. (2) Deformable mirror which constantly changes to counteract and correct the distorted wavefront. (3) Wavefront sensor which, with the real-time computer, calculates the distortion in the wavefront and programs the deformable mirror. (4) Beamsplitter, which separates the incoming light into two parts, the first of which goes through the wavefront sensor, the second of which is the corrected wavefront that is observed by the camera. (6) The corrected image taken by the camera. (Adapted from Davies and Kasper (2012).)

from the star. High-contrast imaging also allows for companions to be studied beyond the 5-10AU separation limitation of radial velocity measurements (Oppenheimer and Hinkley, 2009; Bowler, 2016). One way to minimize the amount of starlight in the image is to use coronagraphy (i.e. Lyot (1939), Sivaramakrishnan *et al.* (2001)), along

with various post-processing techniques that will be discussed in Chapter 3.

A coronagraph is a physical piece of instrumentation made of two masks that are placed in front of the aperture of the detector and aligned to block light from the center of the star (Oppenheimer and Hinkley, 2009; Sivaramakrishnan *et al.*, 2001). This serves to block out much of the starlight from the star and allows for longer observation times, even though the star is still saturated since coronagraphs are not completely opaque. Observing instruments also usually have coronagraphs of different sizes for different observations.

1.7 Thesis Overview

This thesis presents the data reduction and analysis of images of 49 stars from the night of 04 June 2014 and the data reduction of 53 stars from the night of 17 December 2014 that were directly imaged in an effort to detect brown dwarfs. Chapter 2 presents the sample used in this survey and details of the observations. Chapter 3 reports on the methods used in the data reduction of the images. Chapter 4 presents the number of candidates found and their properties. Chapter 5 concludes the thesis and discusses the next steps for the project.

Chapter 2

OBSERVATIONS AND SAMPLE

2.1 Observations

Observations for this survey were done using the NIRC2 instrument on the 10-meter Keck II telescope at the W. M. Keck Observatory on top of Mauna Kea in Hawaii over four nights between 2013[1] and 2014[2]. Only the images taken on 04 June 2014 and 17 December 2013 are discussed in this thesis. Images were taken in the K- and Ks- bands, which range from 2.028-2.364μm and 1.991-2.302μm[3], respectively. These wavelengths are in the near infrared (NIR) part of the electromagnetic spectrum. The use of this particular telescope, instrument, and observing wavelengths provide the resolution and sensitivity needed to detect brown dwarf companions within 8 arcsecs from the star.

The resolution of a telescope can be calculated based on the Rayleigh criterion for resolving two point sources, $\theta = 1.22\lambda/D$, where λ is the observing wavelength and D is the diameter of the telescope. For the Keck II telescope at K- and Ks- band wavelengths, the average resolution is 0.0548 arcseconds. The images were taken with the narrow band camera, which has a field of view of 10x10 arcsec and a pixel scale of 0.009942 $\pm$ 0.00005 arcsecond/pixel[4].

With NIRC2, a coronagraph, an AO system, a large telescope, reference differential imaging, and PSF subtraction, we can also achieve the sensitivity necessary to detect brown dwarfs around these young bright stars. Before the survey was con-

[1]Keck Project # H209N2, PI:Eric L.Nieslen
[2]Keck Project # H2668N2, PI: Eric L. Nielsen
[3]NIRC-2 General Specifications,https://www2.keck.hawaii.edu/inst/nirc2/genspecs.html
[4]NIRC-2 General Specifications,https://www2.keck.hawaii.edu/inst/nirc2/genspecs.html

ducted, contrast curves such as the one presented in Figure 2.1 were created from existing NIRC2 data to demonstrate the predicted sensitivity of this survey. The mass scale shown on the right y-axis is dependent on the age and K-magnitude of the star. For this plot, the age was assumed to be 100 Myr for an A0 type star. Figure 2.1 also shows that this survey, due to the larger telescope and the longer exposure times, should be able to detect companions of masses much lower than the VAST Survey (De Rosa et al. 2011) and will be able to detect companions such as HR 8799b. This companion is approximately $7M_{Jup}$ and is approximately 68AU from the host star, which is within the range of companions we are aiming to detect.

The observations were taken in vertical angle mode, where the instrument was in a fixed position while the sky rotated. A 600 milliarcsecond (mas) coronagraph diameter was also used to block all but 0.22% of the light from the core of star[5]. Vertical angle mode is used to keep the PSF stable and prevent the diffraction spikes from moving from image to image. Images were taken with the coronagraph at exposure times of 30 seconds for brighter stars and 60 seconds for dimmer stars for less read noise. In these images the stars are saturated, so unsaturated images were taken at exposure times of less than 10 seconds in order to accurately calculate their fluxes. These times were chosen for a number of reasons. First, with such short exposure times and with all stars being observed far from transit, the sky does not move measurably, so any candidate companions do not smear. All the stars were observed far from transit to ensure minimal smearing. Second, at these observation wavelengths, the sky saturates at 10.5 minutes of exposure [6]. Short exposure times minimize the problem of having the background sky over saturated in the image. Lastly, exposure times of this length and not shorter minimizes the read noise in the detector. A total of 200 B and A

[5]NIRC-2 General Specifications,https://www2.keck.hawaii.edu/inst/nirc2/genspecs.html
[6]https://www2.keck.hawaii.edu/inst/nirc2/sensitivity.html

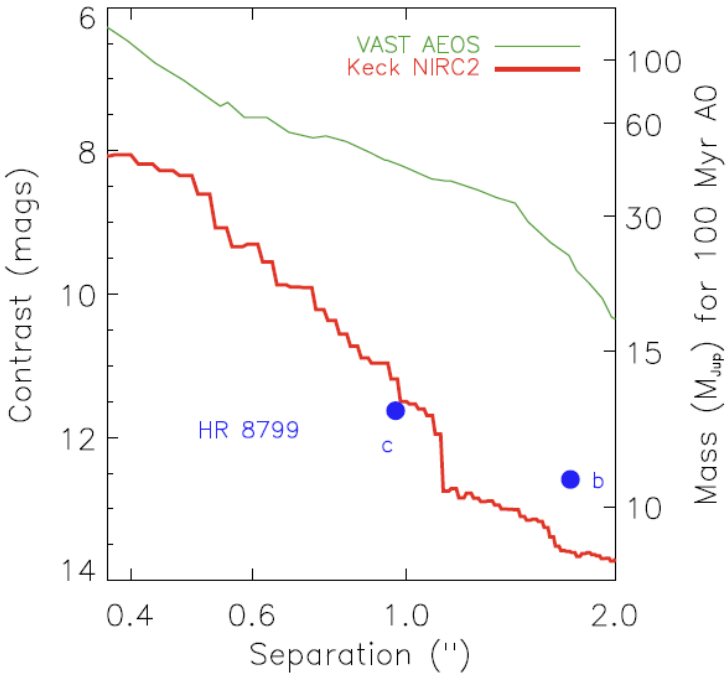

Figure 2.1: Contrast curves for the VAST survey and the NIRC2 telescope show the difference in sensitivity between the first survey and the camera used for this survey. The green line is the contrast achieved by the VAST survey (De Rosa *et al.*, 2011). The red line shows the contrast expected for this survey for a 100Myr old star created from an existing NIRC2 dataset [6]. HR 8799b is detectable with this contrast, and HR 8799 lies just below the contrast curve and would be detectable around a star that is either younger or closer. The significance of HR 8799b lying above the contrast curve is that it has properties in the range of what we are aiming to detect in this survey. (Adapted from De Rosa *et al.* (2011)).

stars were imaged over four nights for the entirety of this survey. This thesis presents analysis for 49 stars from 04 June 2014 and 53 stars from 17 Dec 2013.

2.2 Sample

The properties for the 102 B and A stars out of 200 total stars in the survey are shown in Appendix A for the nights of 04 June 2014 and 17 December 2013.

The ages were calculated using a Bayesian analysis method (Nielsen *et al.*, 2013).

[6]Keck Project # H2668N3, PI: Eric L. Nielsen

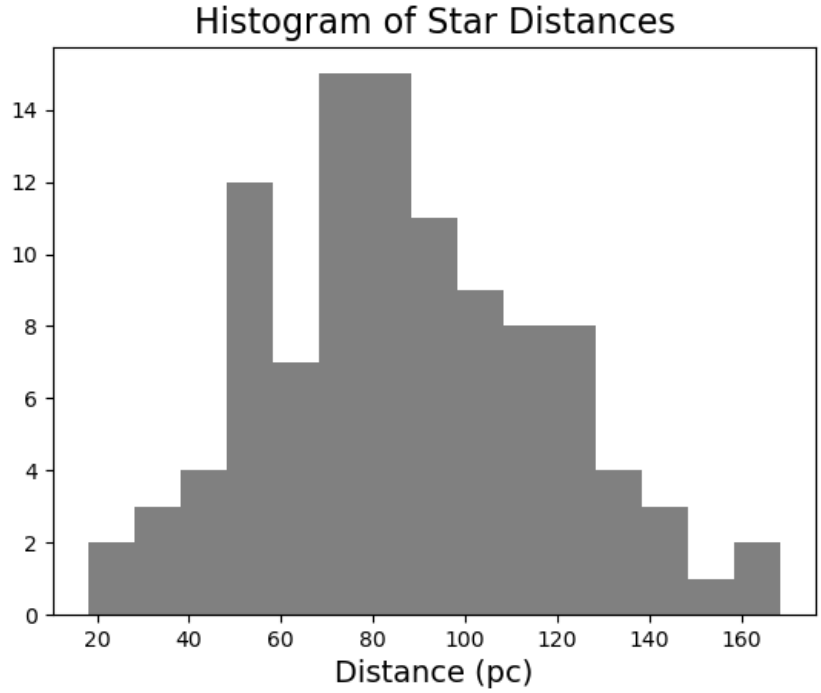

Figure 2.2: The stars chosen for this survey are all within 160pc, most being within 120pc. Stars closer to Earth were chosen deliberately. This histogram shows the range of distances in the star sample with the distribution peaking in the middle.

As stated in Chapter 1, star ages can be calculated based on several properties and their location on a color-magnitude diagram (CMD). This method, however, is not always accurate because of the degeneracy between age and metallicity of a star. Based on comparisons to the ages of stars in known clusters, such as the Pleiades, stars low on the CMD are also young. However, due to this degeneracy, the low position on the CMD could actually indicate youth or low metallicity. The method described in Nielsen *et al.* (2013) uses Bayesian inference and prior knowledge to determine the likelihoods of the different combinations of the properties age, mass, and metallicity to estimate the most likely age of the star. The ages for HIP 90752, HIP 82216, HIP 79007, HIP 68756, HIP 46813, and HIP 84012 were calculated using a slightly altered version of this method where the model grid was not allowed to go

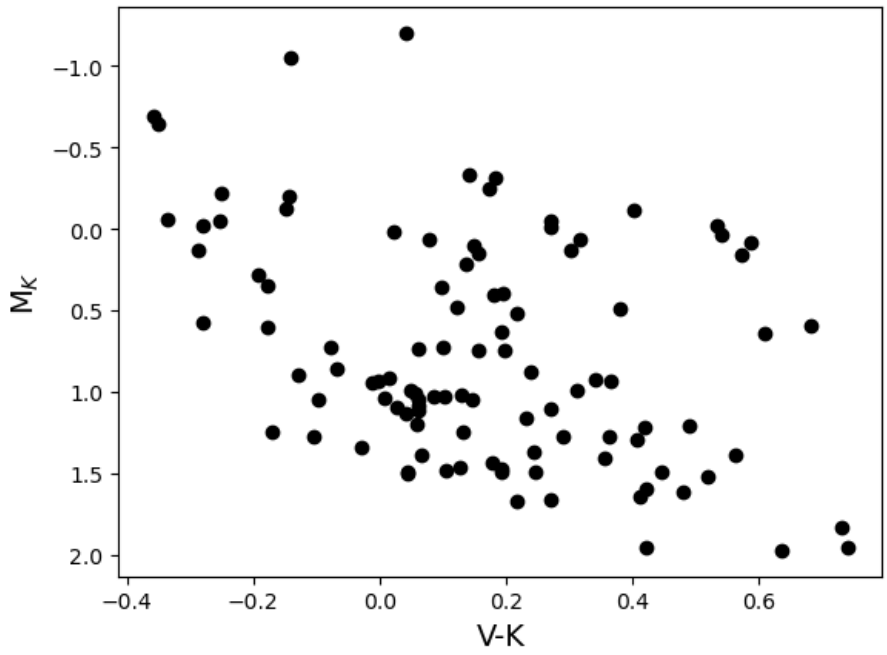

Figure 2.3: A color magnitude diagram of the stars from 04 June 2014 and 17 December 2013. The wide distribution shows that not all the stars are on the main sequence, as some have evolved off.

below 10Myr. RA, DEC, parallax, distance, V magnitude, K magnitude, and spectral type for each star are shown in Table A.1. The sources and citations for each property are also given in the Table. Errors in K magnitude of HIP 32838, HIP 24305, HIP 5542, and HIP 4436 were estimated from other stars with similar magnitudes. HIP 84012 was not reduced with the pipeline due to the fact that the observations were aborted part way through. HIP 109754, HIP 109831, and HIP 85391 were reduced but their candidates were not analyzed. HIP 109754 and HIP 109831 both do not have the necessary unsaturated images, and HIP 85391 is low in the galactic plane and has 40+ candidates and therefore was not in the scope of this thesis to analyze.

These stars were selected using a Monte Carlo code (Nielsen *et al.*, 2008; Nielsen and Close, 2010; Nielsen *et al.*, 2013) that generates simulated exoplanets and compares them to a contrast curve. This comparison determines which stars are most

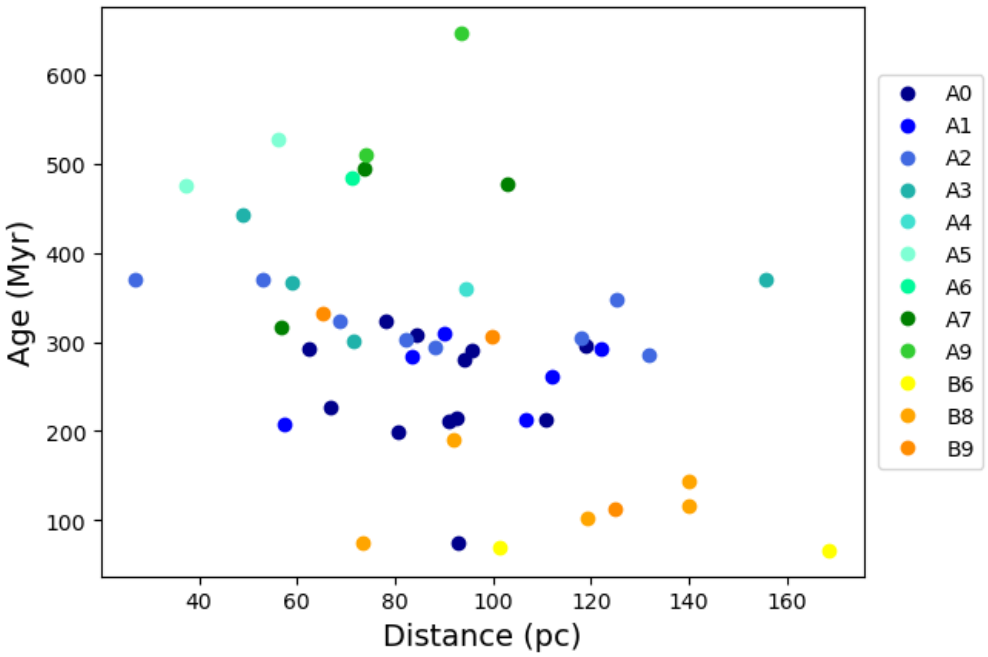

Figure 2.4: The age, distance, and spectral type distributions of the sample of stars from 04 June 2014 showing that most are young, close A stars.

likely to have detectable brown dwarfs, given the contrast curve and star properties. From the initial list of possible candidate stars, these were chosen because they are young, close, have the highest likelihood of hosting detectable brown dwarfs, and have not yet been observed at high contrast. Most of the stars in this sample are closer than 120 pc (as shown in Figure 2.2) and younger than 1 Gyr. The advantage of observing early type stars, is that even though they are younger, they will be brighter, which makes it easier to detect low mass companions. Later type stars will be older, but also intrinsically fainter. Another reason B and A stars were chosen in particular is because the frequency of stellar companions is greater among higher mass stars (Duchêne and Kraus, 2013; Sana *et al.*, 2014).

Chapter 3

DATA REDUCTION

A custom pipeline was written for this survey in order to reduce raw images dominated by the stellar halo to PSF-subtracted images where candidate companions can be easily identified. An example of a raw image from HIP 81634 can be seen in Figure 3.1a. This section will discuss the pipeline process which includes correction for dark current, differing pixel quantum efficiencies, bad pixels, instrument distortion, and overwhelming starlight through dark subtraction, flat field division, bad pixel correction, distortion correction, reference differential imaging (RDI), and PSF subtraction.

3.1 Darks, Flats, Bad Pixels, and Distortion Correction

The first step in the pipeline is subtracting a dark image (seen in Figure 3.1b) from each science image of the stars. In an ideal environment where the telescope could be cooled to a relatively low temperature, when an image is taken with the shutter on the camera, all pixels should read zero counts because no light is hitting the detectors. However, not all pixels record zero counts due to background thermal energy that excites the electrons in the detector creating false signals. The dark images were taken with a dark filter at the same exposure times as the science observations. Each science image is matched with a dark of the same exposure time for the subtraction.

Figure 3.2 shows a flat field, where an image is taken with the camera pointed at either a uniformly illuminated screen or a uniform area of the sky. This survey used the uniformly illuminated screen, and with the corograph in place, images were taken at the same exposure times as the science images. As with the dark subtraction, each

science image is matched with the flat field of the same exposure time. With a perfect array, each pixel would count the same number of photons. Some pixels have different amounts of counts than others due to quantum efficiency variations. To correct for this, the science image is divided by the flat field.

Even with these corrections, there are still several bad pixels that need to be corrected. In order to correct these pixels, each one is examined individually and if the photon count for that pixel is three standard deviations more than the average of the neighboring pixels, that bad photon count is set to the average of those neighboring pixels. Using this method, a bad pixel mask is created in order to correct each science image.

The last step in this part of the pipeline is to correct for optical distortion from the camera. Two types of optical distortions can affect the images and are shown as exaggerated depictions in Figure 3.3. The first is barrel distortion, where the field is pushed outward from the middle. The second is pincushion distortion, where the field is pushed inward. In order to correct for these optical distortions, the UCLA Galactic Center Group published a distortion model for the NIRC2 instrument (Yelda *et al.*, 2010). This model was constructed by taking several images of the globular cluster M92 and comparing to HST images. For all of the stars that appear in each image, a model can be made using their positions in the image and actual positions that have been previously measured. This model was then tested on images of the Galactic Center and the model proved effective (Yelda *et al.*, 2010). We used this distortion map to correct our images. The partially reduced image created after application of dark subtraction, flat fielding, bad pixel correction, and distortion correction is shown in Figure 3.4b and can be compared to the raw image in Figure 3.4a which shows that these reduction steps were able to remove the bad pixels from the image.

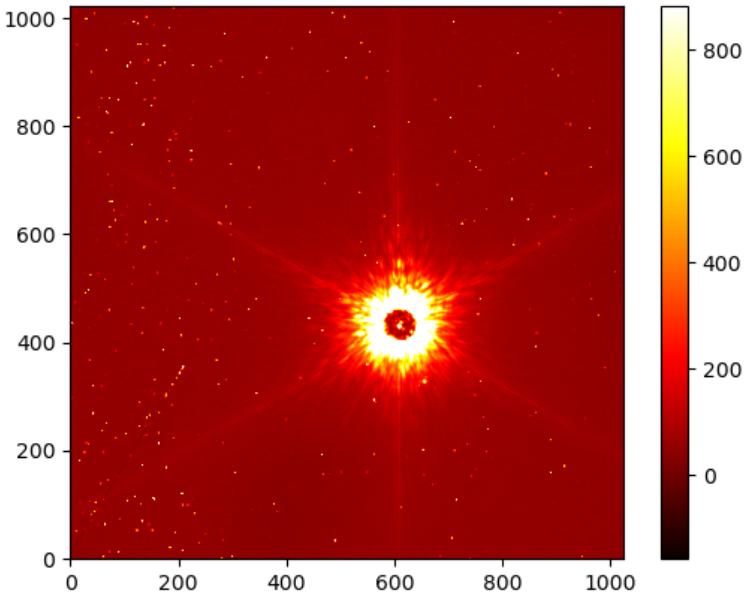

(a) Raw image of HIP 81634.

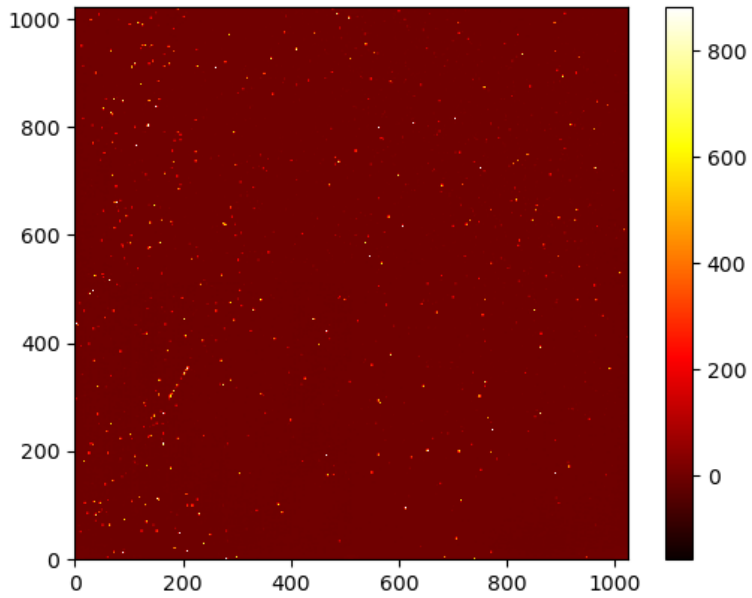

(b) Dark Image

Figure 3.1: Top image shows an example raw image before data reduction. Bottom image shows a dark with a median count of 2.5.

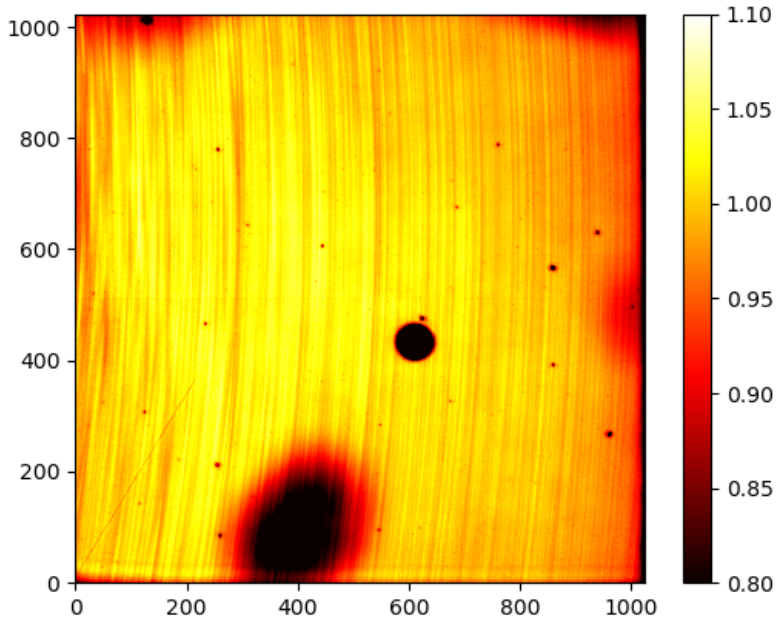

Figure 3.2: Example flat field image with the coronagraph (black circle in the middle). Counts are normalized to one and the black area in the lower part of the image has counts of approximately 0.8.

3.2 Centering and Smoothing

The next step in the reduction process is shifting the center of each star in all the images from one night to the same location. This is necessary preparation for the final reduction step as the images will be stacked and are required to be aligned. The center of each star was found using radon tranforms, which uses the radial nature of the image to take line integrals and locate the center. After centering, we apply a median filter to smooth out remaining noise. The resulting image from this step in the reduction is shown in Figure 3.6a.

The last step before running the images through a package called pyKLIP is to pad the images. In the final stage of reduction the images are rotated. This rotation results in the outer parts of the image being cut off. We make the images larger by asymmetrically padding each one with zeros to ensure the entire science image

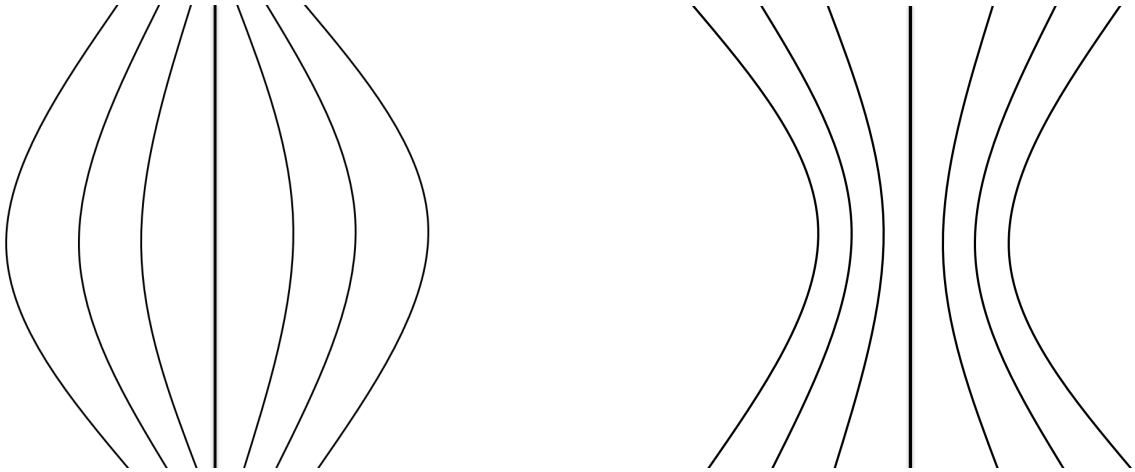

(a) Barrel Distortion. (b) Pincushion Distortion.

Figure 3.3: Two types of optical distortion common to optical telescopes. The particular distortions of the NIRC2 camera were measured by the UCLA Galactic Center group (Yelda *et al.*, 2010) and are corrected for in our images.

remains intact.

3.3 pyKLIP

The final step of the reduction is to run principal component analysis (PCA) using the Karhunen-Loéve Image Projection (KLIP) algorithm (Soummer *et al.*, 2012) implemented through a package called pyKLIP (Wang *et al.*, 2015). The KLIP algorithm and the package pyKLIP can be used with data from a few different instruments including NIRC2 and the Gemini Planet Imager. The goal of this algorithm is to create a reference image constructed from the similarities in images of the reference library, in order to subtract the reference PSF from the PSF of the target star. This will subtract out much of the bright starlight, while leaving behind more visible candidate companions. There are a few modes in which pyKLIP can be run. For this dataset, Reference Differential Imaging (RDI) was selected, which uses a reference library made of the images of all the stars taken in one night except for the specified target.

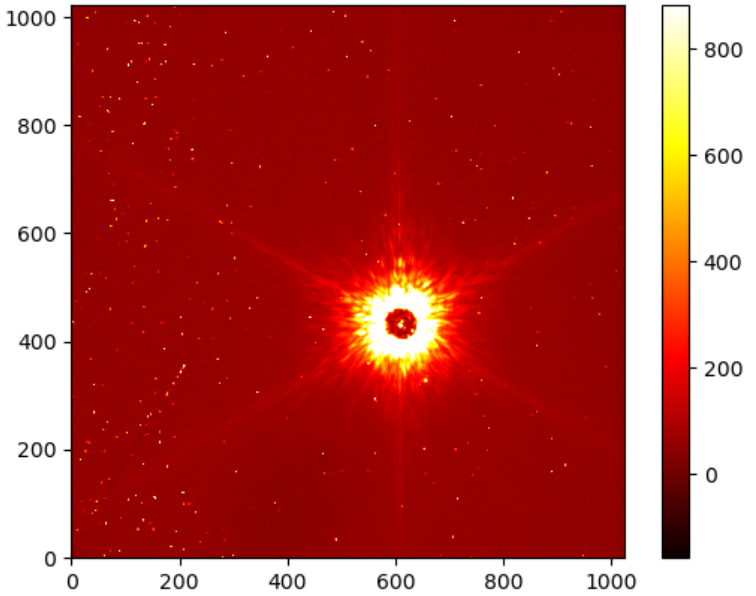

(a) Raw Image of HIP 81634

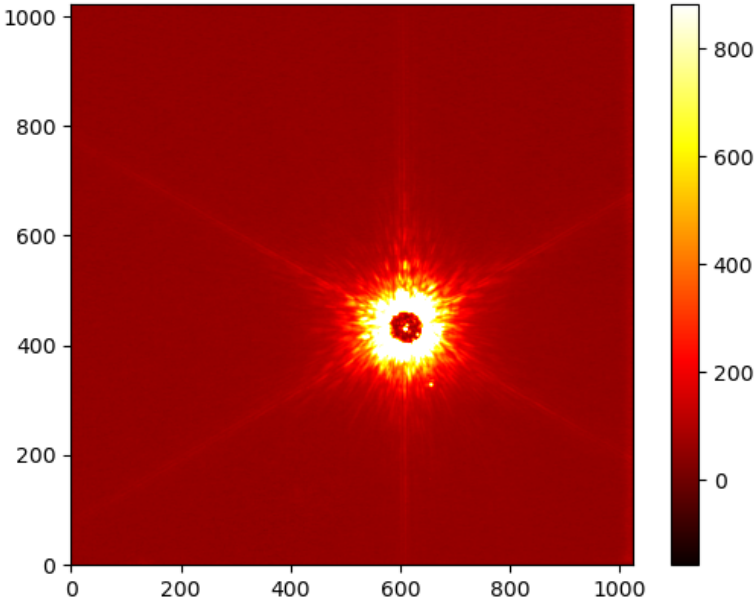

(b) HIP 81634 after dark subtraction, flat fielding, bad pixel correction, and distortion correction.

Figure 3.4: Comparison between the raw image and the partially reduced image. The lack of higher count pixels is evident in the partially reduced image.

The first step of the RDI process is to create a correlation matrix using all the images from one night, which tells the algorithm which of the images are most correlated and to be used in the reference library. Next, a set of target images is separated from the set of reference images. In each image, pyKLIP splits the image into several sections on which to run the algorithm. The number of these sections is determined by 3 parameters: number of annuli, number of subsections, and spacing of the annuli. A depiction of how pyKLIP makes these sections is shown in Figure 3.5. The annuli are concentric circles that can either have constant spacing, or spacing that increases either in a linear or log pattern outwards. The subsections are the straight lines that split the annuli into smaller sections such as the one shown in grey. This is the section, S, in which the algorithm is performed. In order to produce the optimal reduced image, determining the best parameters required experimentation. The final images were reduced with 30 annuli with log spacing and 128 subsections. The spacing of the annuli allowed for the cleanest reduction with various bright pixels being removed, and the 128 subsections allowed for an aggressive enough reduction in a reasonable amount of time.

After these parameters are specified, the algorithm separates the target images from the references images and in the area S, their respective averages are subtracted so they are mean centered. Next, the KL transforms of the reference images are calculated. This calculates the eigenvectors and eigenvalues of the section, which represent the vectors with the most variance or the most patterns in the image. These are the principal components of the image. Once the principal components are found, the number of principal components to keep in order to construct the final reference image needs to be decided. Increasing the number of principal components, or KL modes, results in a more aggressive reduction. The advantage of many KL modes is that more of the starlight and background is removed. The most important

disadvantage is that with too many KL modes the algorithm could subtract out real companions, called over-subtraction. A second reason to not use too many KL modes is that we did not see a measurable difference in the final images in the time it took for the code to run. Instead of just setting one number of KL modes to keep, pyKLIP gives the user the option to enter an array of numbers in order to determine the optimal number of principal components to use. For this survey we used 1, 5, 10, 20, and 50 KL modes.

The second to last step is to create the best estimate reference PSF from the set of reference images using the projection and scaling of the target images. The final image is then created by subtracting the estimated reference PSF from the median combination PSF from all the images of the target star. The method used to combine these images is also an adjustable parameter. We found that using a median collapse provided the best final image and removed remaining hot pixels (pixels with very large counts). The final image from our example star HIP 81634 is shown in Figure 3.6b. The two circled companions are now more easily identified than in any of the previous images generated by this reduction process.

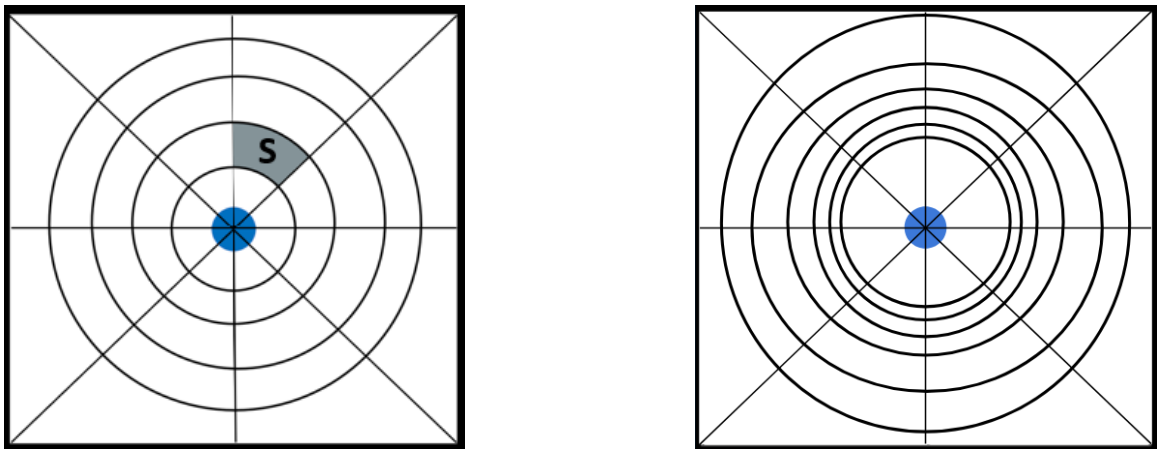

(a) (b)

Figure 3.5: Schematics of how pyKLIP separates images into annuli (concentric circles) and subsections (straight lines). S represents an example section on which the KLIP algorithm is performed. Figure 3.5a shows a constant separation of the annuli while Figure 3.5b shows progression of annuli from small to larger widths.

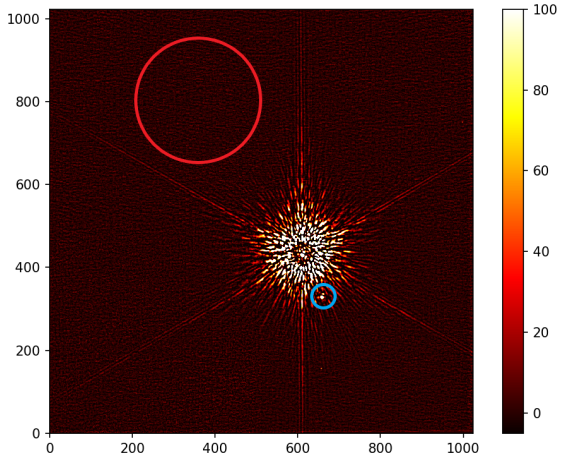

(a) Image of HIP 86134 after shifting and smoothing and before pyKLIP.

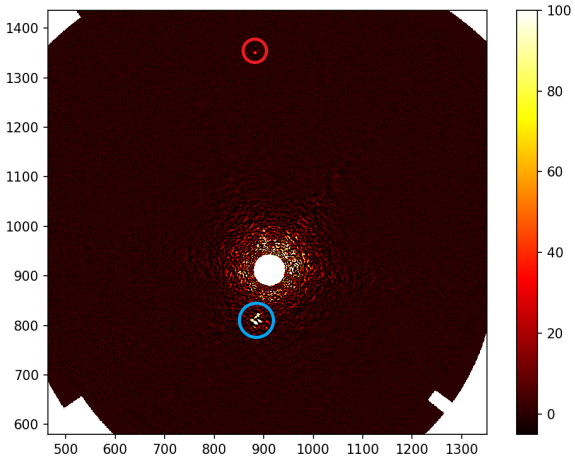

(b) Final image of HIP 86134 after running through pyKLIP.

Figure 3.6: Two images showing the star HIP 81634 before and after pyKLIP. Circles in the post-KLIP image show the two candidates found around this star. The red circle in the post-KLIP image shows one of the companions that can be seen. A similar red circle shows approximately where the dimmer companion would be in the pre-KLIP image.

Chapter 4

RESULTS AND DISCUSSION

This section presents the results of the data reduction pipeline and discusses calculations of separation, magnitude, and mass of each candidate companion.

4.1 Results of Reduction

Figure 4.1 shows an example star, HIP 81634, in the raw image and in the post-KLIP image. The post-processed image is significantly different in terms of the capacity to identify companions. After the reduction process, the images for each star had to be scanned by eye using SAOImageDS9 software (Joye and Mandel, 2003). Real objects have a specific shape called an Airy Pattern, show in Figure 4.2, and are not just random areas of higher count pixels.

Once candidates were identified, we used the procedures detailed below to calculate separation, absolute magnitude, and mass of each candidate companion from the data collected on the night of 04 June 2014. These properties of each candidate are presented in Appendix B. A total of 95 candidate companions were found around 22 stars. Only 91 of the companions were analyzed because two of the stars did not have the unsaturated images needed for the magnitude calculations. The saturation can be corrected for at a later date. From the results of the NICI survey (Nielsen *et al.*, 2013), we only expect approximately 7 candidates will be actual brown dwarf companions out of the entire survey of 200 stars, therefore the identified candidates are most likely background stars. Here we present the reduction results of 45 stars from the night of 04 June 2014. Three stars that were reduced and have candidates were not analyzed. HIP 109745 and HIP 109831 do not have unsaturated images, but are

included in the total candidate count of 95. HIP 85931 has 40+ candidates and analyzing those is beyond the scope of this thesis and these candidates are not included in the total count. All calculated and inferred candidate properties are presented in Appendix B.

4.2 Separation Calculations

In order to calculate the projected separation, between the star and candidate companion the separation in the image was calculated in pixels. The distance formula, $d = \sqrt{(x_2 - x_1)^2 + (y_2 - y_1)^2}$ was used to find the separation in the image between the center of the star and the center of the companion. The centers of the stars were found using a radon transform described in Chapter 3. The center of the companion was found using a Moffat function, where a model is fit to the companion to determine the center using the location of highest modeled photon counts. This separation was then converted into units of arcseconds using the NIRC2 pixel scale of 0.009942 $\pm$ 0.00005 arcsec/pixel. Errors for this calculation, and most calculations in this section, were computed using the standard partial derivative equation shown in Equation 4.1, where x is a function of u and v.

$$\sigma_x^2 = \sigma_u^2 \left(\frac{\partial x}{\partial u}\right)^2 + \sigma_v^2 \left(\frac{\partial x}{\partial v}\right)^2 + ... \tag{4.1}$$

A physical projected separation was then calculated in Astronomical Units (AU) using the small angle approximation, Equation 4.2, where d_{cand} is the projected separation in AU, θ is the separation previously calculated in arcseconds, and d_{star} is the distance to the star in parsecs.

$$d_{cand} = \theta * d_{star} \tag{4.2}$$

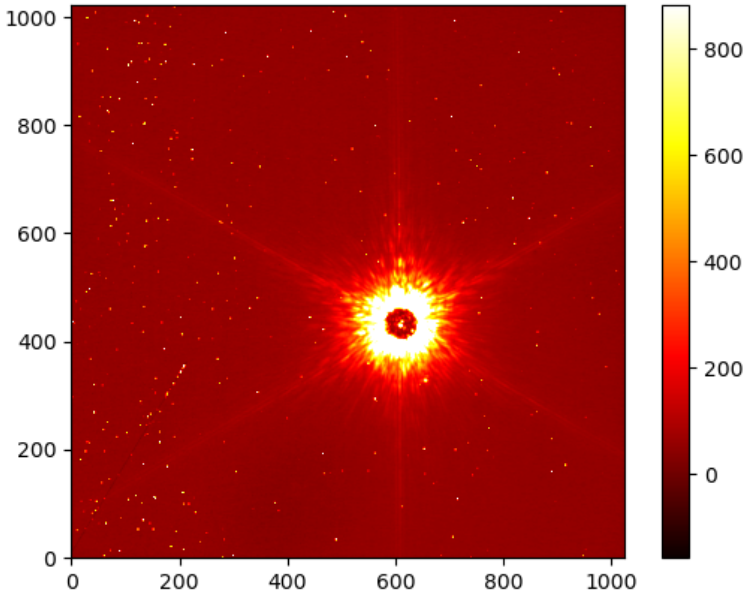

(a) Raw image of HIP 81634.

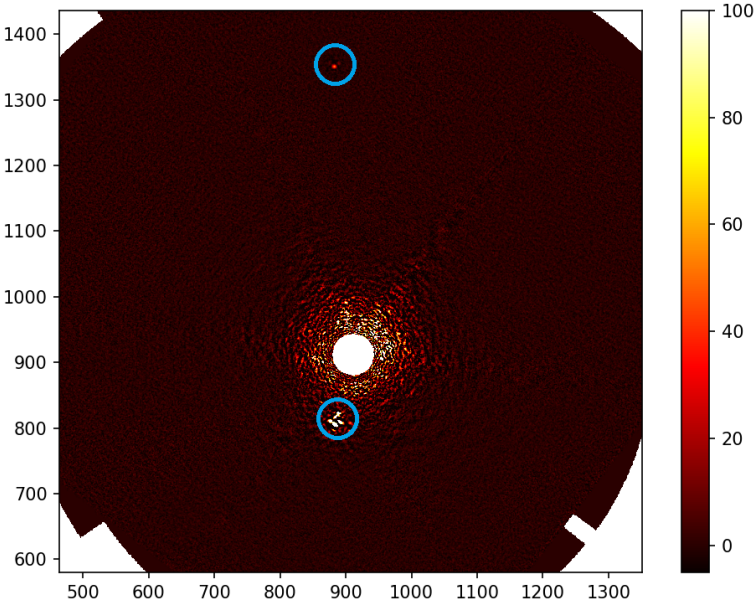

(b) Final image of HIP 86134 after running through entire data reduction pipeline.

Figure 4.1: Two images showing the star HIP 81634 before and after the reduction pipeline, showing the success of the pipeline to reduce raw images to final images where companions can be seen.

(a) (b)

Figure 4.2: Examples of two candidate companions showing their general shape and airy rings.

d_{star} was calculated using the parallax measurement of the star obtained from both the Gaia Early Data Release 3 (Gaia Collaboration, 2020) and the Hipparcos Catalogue (van Leeuwen, 2007). Parallax is given in units of milliarcsecond (mas), and d_{star} was calculated by dividing 1000 by the parallax, d_{star} =1000/parallax (mas). For both of the above calculations, the error was propagated using the partial derivatives method shown in Equation 4.1.

4.3 Magnitude Difference Calculations

The magnitude difference (Δm) between the host star and the candidate was also calculated. The Δm between two astronomical point sources can be found using Equation 4.3, where F_{cand} is the flux of the candidate companion and $F_\star$ is the flux of the host star.

$$\Delta m = m_{cand} - m_{star} = -2.5 log_{10} \left(\frac{F_{cand}}{F_{star}} \right) \tag{4.3}$$

F_{cand} was found by using the Moffat fit model to estimate the maximum number of counts in the companion. $F_\star$ was more complicated to calculate because the star is blocked in the final images and saturated in the higher exposure images. The

lower exposure images, 10s or less, were used to calculate the flux of the star in the final pyKLIP image. This was done by first finding the modelled maximum number of counts in the star in the unsaturated images, which was calculated again using the Moffat fit model. The number of counts was then multiplied by the ratio of the saturated image exposure time divided by the unsaturated image exposure time. Finally, because the unsaturated images still included a coronagraph over the star, the images were divided by 0.0022, the transmission rate of the 600 mas coronagraph as stated in Section 2.1. Figure 4.3 shows the results of these calculations vs. separation in arcseconds. The error was calculated using Equation 4.1.

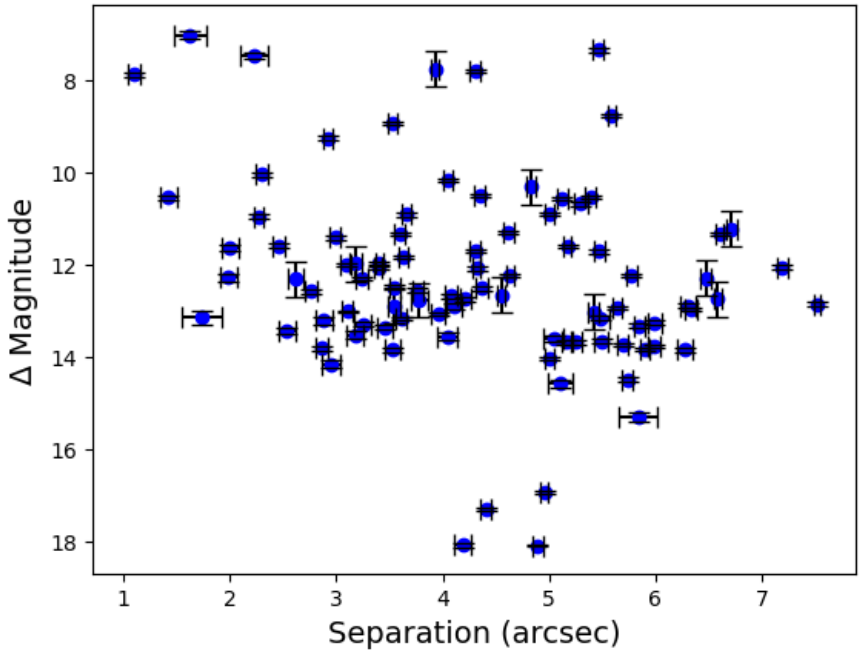

Figure 4.3: Δ Magnitude vs. Separations for all candidate companions found from the night of 04 June 2014 showing the range of properties of these candidates.

Figure 4.4 shows examples of two contrast curves for HIP 101716 and HIP 105282 and their companions. Contrast curves show the sensitivity of the observations. In order for a candidate to be detected, it must lie above the curve. For these two examples, all the companions do lie above the curve. These contrast curves were

made by creating concentric annuli around the star and finding the Δm limits for a companion that is 5σ from the median of the annulus. Each annulus was also sigma-clipped so that any counts above a σ of 9 from the median of the annulus were not included in the calculation. This was done to mask the candidate companions, as they produce spikes in the curves. Figure 4.5 shows all of the candidate data plotted on all of the contrast curves of the 43 stars from the night of 04 June 2014 that were reduced and had unsaturated images.

Figure 4.6 shows the median contrast curve from Figure 4.5 (dashed line) and the contrast curves of HIP 84880 and HIP 90241 (solid lines), which are much lower. Also included are the companions to these two stars. In investigating the difference between these two stars and the median of the other stars, we found that these two stars were saturated even in the lower exposure images. A saturated image of HIP 84880 with an exposure time of 0.726s and a non-saturated image of HIP 101421 with an exposure time of 1s are shown in Figure 4.7. According to the NIRC2 Manual[1], if the counts reach higher than 10,000, the detector is saturated, and counts are no longer recorded linearly. Scaling the unsaturated counts to the saturated image for calculating Δ magnitude assumes that the star is not saturated.

The PSF of a star that is saturated usually has an irregular pattern at the peak instead of a point. One possible solution to this saturation problem would be to fit the wings of the PSF to correctly construct the middle to estimate a more accurate number of counts for the peak of the star. Another possible solution is that to use another object in the image that is not saturated in order to scale the number of counts. This solution, although simpler, can be difficult as most stars do not have other visible objects in the background. There is a similar saturation problem with the night of 17 December 2013, so the final solution will be used for both nights.

[1]https://www2.keck.hawaii.edu/inst/nirc2/sensitivity.html

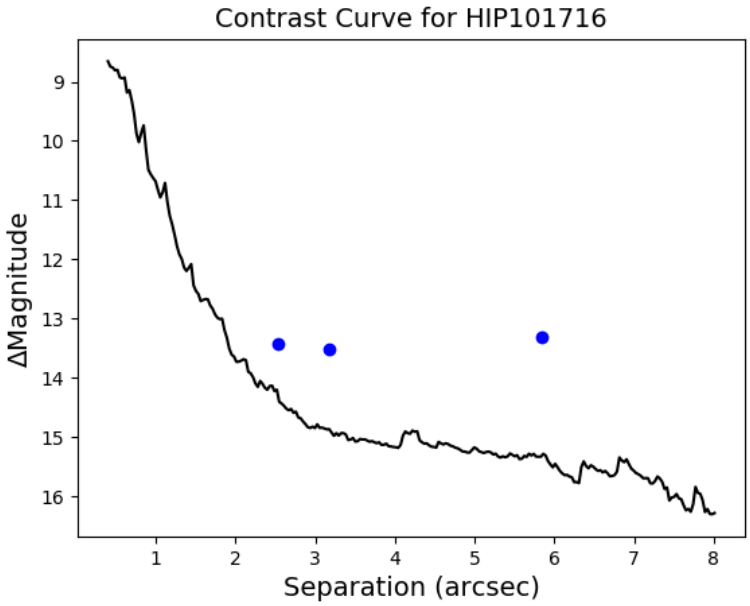

(a) Contrast Curve of HIP 101716 with candidate companions.

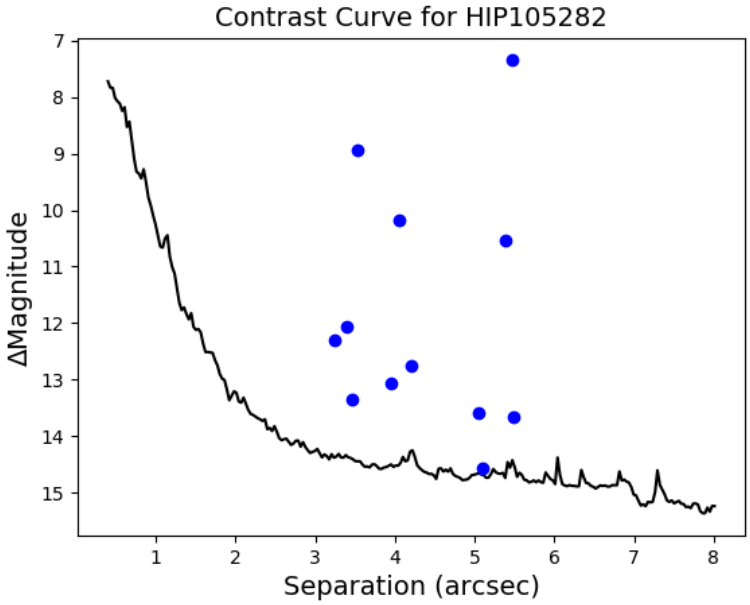

(b) Contrast Curve of HIP 105282 with candidate companions.

Figure 4.4: Examples of two contrast curves with companions showing the sensitivity of the survey as well as the fact that the candidate companions are above the necessary threshold to be observed. This implies that the candidates are real objects, though not necessarily bound companions.

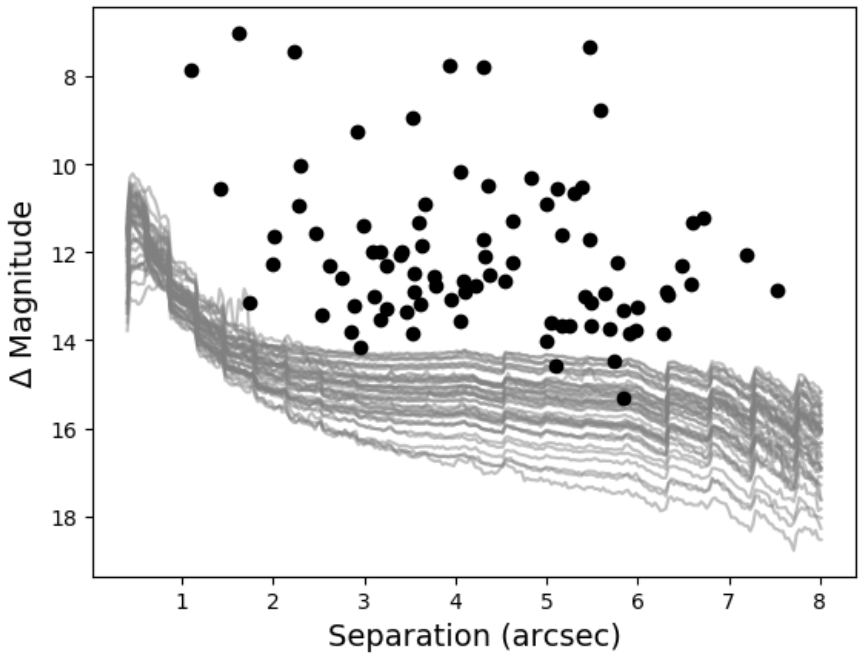

Figure 4.5: Contrast curves plotted of 43 stars that were fully reduced and analyzed from 04 June 2014 with the 91 candidates from 20 stars over-plotted.

4.4 Mass Calculations

Assuming that each candidate is bound to its host star, we used the COND evolutionary models (Baraffe *et al.*, 2003) to calculate the mass of each companion. These models provide masses with corresponding absolute magnitudes for brown dwarfs at ages 0.001, 0.005, 0.010, 0.050, 0.100, 0.120, 0.500, 1.000, 5.000, and 10.000 Gyr. The age of each star had been previously calculated and are shown in Appendix A. The remaining variable to calculate is the absolute magnitude of each candidate companion.

4.4.1 Absolute Magnitude Calculations

In order to calculate absolute magnitude of the companion, the apparent magnitude was calculated first. Since $\Delta m = m_{comp} - m_{star}$, the apparent magnitude of the

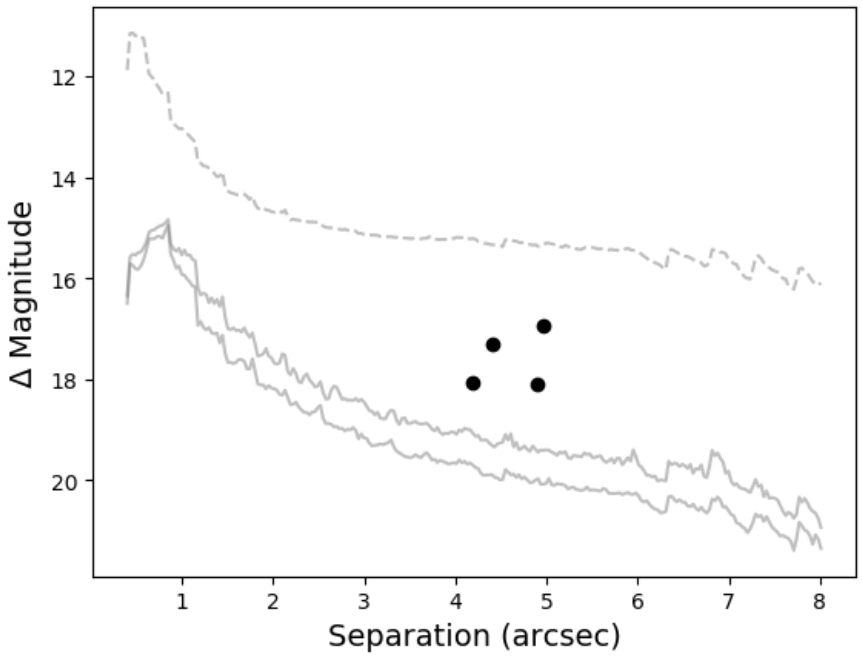

Figure 4.6: Median contrast curve from stars with unsaturated images (dashed line) and contrast curves of HIP 84880 and HIP 90241 (solid lines) and their companions. The curves from these two stars are much lower than the median due to the fact that their lower exposure images are still saturated, making additional analysis necessary to accurately create contrast curves.

candidate can be found by adding the difference in magnitude to the known apparent magnitude of the star in the K-band (Cutri *et al.*, 2003a). From the apparent magnitude, the absolute magnitudes (M_{cand}) were calculated using Equation 4.4,

$$M_{comp} = m_{comp} - 5log_{10}\left(\frac{d_{star}}{10}\right) \tag{4.4}$$

where d_{star} is the distance to the star. The error for the above calculations was also found using Equation 4.1.

4.4.2 COND Model Interpolation

Once the age of the star and the absolute magnitude of each candidate companion were calculated, we used the COND evolutionary models (Baraffe *et al.*, 2003) to

calculate approximate masses for each candidate. As stated above, the model gives masses for a discreet number of absolute magnitudes in the K-band for a discreet number of ages. Two interpolations were performed to extract the masses of our candidates from this model.

First, for each unique mass used in the model, an interpolation was performed over the corresponding magnitudes and ages. Figure 4.8a shows the discreet points of absolute magnitude vs. age for 42 M_{Jup}. Figure 4.8b shows examples of the interpolation done between the points. This interpolation was then used to find the absolute magnitude for each mass line at the specific age of the candidate companion in question. For this specific age, mass vs. absolute magnitudes could then be plotted, which is shown in Figure 4.9 for a candidate companion in a system that is 347^{+65}_{-54}Myr old and has an absolute magnitude of 11.97 $\pm$ 0.06.

With a second interpolation between the points, the mass at this particular magnitude was found to be 35^{+2}_{-4} M_{Jup}. This was done for each candidate and the errors were estimated using the error in absolute magnitude and the error in mass to make the most conservative estimate for the maximum mass and minimum mass of each candidate.

Figure 4.10 shows a plot with all of the candidate masses and projected separations. The blue lines show the brown dwarf mass limits. It is possible that the candidates that are above the 75 M_{jup} limit are low mass stars, possibly binaries. Most likely however, is that most if not all of these candidate companions are actually background stars, not bound to the host star.

Figure 4.11 shows the contrast curves for each star as well as all the companions below 75 M_{jup} in order to keep the scale small enough to see the curves. This shows the observations can achieve enough contrast to detect brown dwarfs.

4.5 Attempted Reduction of 17 Dec 2013

The reduction pipeline was also run on all the stars from 17 Dec 2013 shown in Appendix A. Only 5 of the stars have clear candidate companions in the post-KLIP images. For many of the other stars, the candidate companions that are visible in the pre-KLIP images are either not seen in the post-KLIP image or are seen as black spots, which means they are being subtracted out. An example of this can be seen in Figure 4.12. Figure 4.12a is an image of HIP 14544 from the stage of the pipeline immediately before running pyKLIP. There is a very obvious companion on the bottom left of this image. Figure 4.12b shows this same star after pyKLIP, and the companion is a black artifact in the upper right hand corner.

We have found that for the stars with companions that are being subtracted out, the position of the companion actually moves from image to image of the same star. Since pyKLIP rotates the science images and then stacks them at the end this should not cause a problem. However, we found that the current parallactic angles that pyKLIP is using for the images is incorrect, which leads to an incorrect rotation and the companions disappear when the images are stacked using a median combination. The next step is to correct the parallactic angle calculations and re-run pyKLIP on this night.

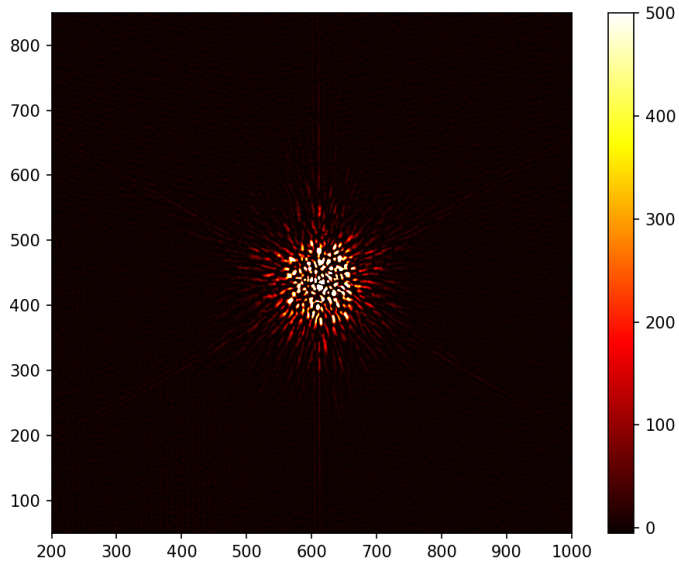

(a) HIP 84880, saturated star.

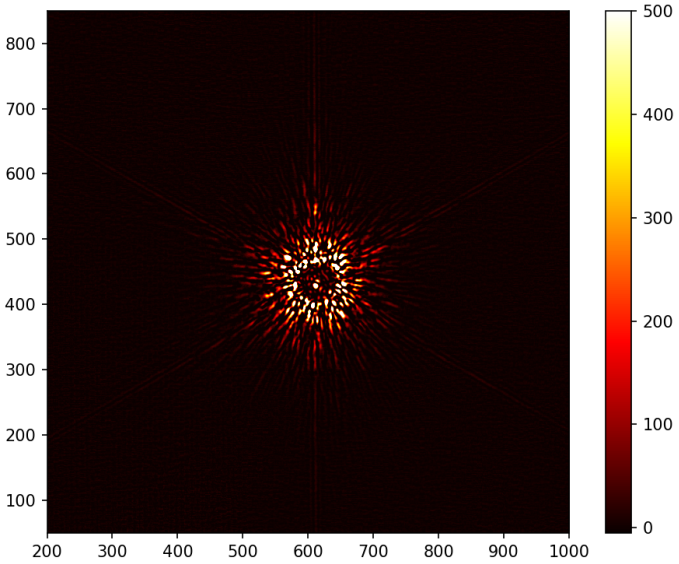

(b) HIP 101421, unsaturated star.

Figure 4.7: The left image shows HIP 84880 taken with an exposure time of 0.726s. The maximum counts in the center of the star is approximately 32154, well above the 10,000 count limit for NIRC2. The right image shows HIP 101421 taken with an exposure time of 1s. The maximum counts for this star is approximately 2345, well below the saturation limit. These two images also show that when the star is unsaturated, the coronagraph blocks most of the star light except for a spot in the center where the star is the brightest. For the saturated star, the coronagraph cannot be seen in the image and is not blocking most of the light from the star.

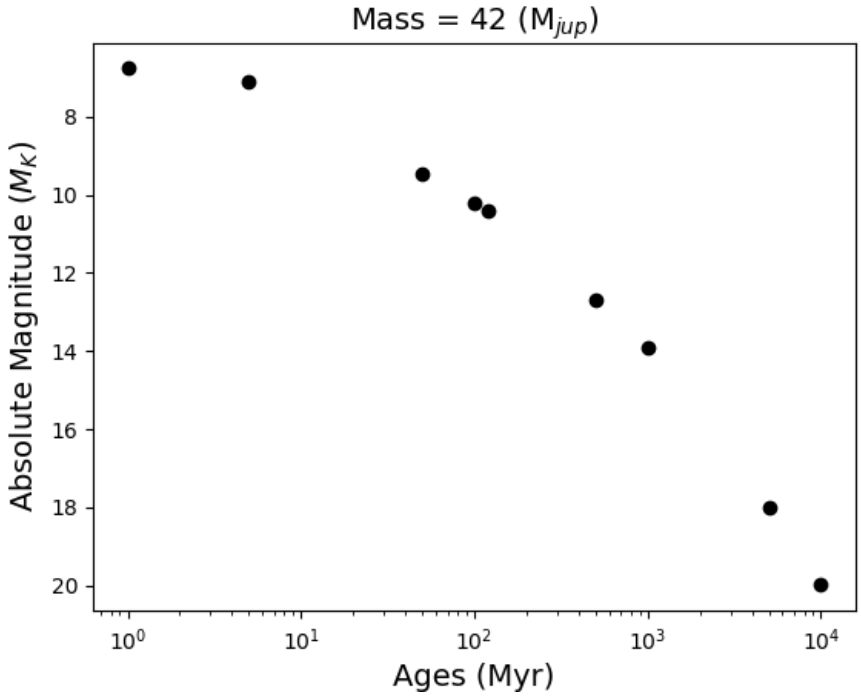

(a) Absolute magnitude vs. Age for a 42 M_{Jup} planet from the COND models.

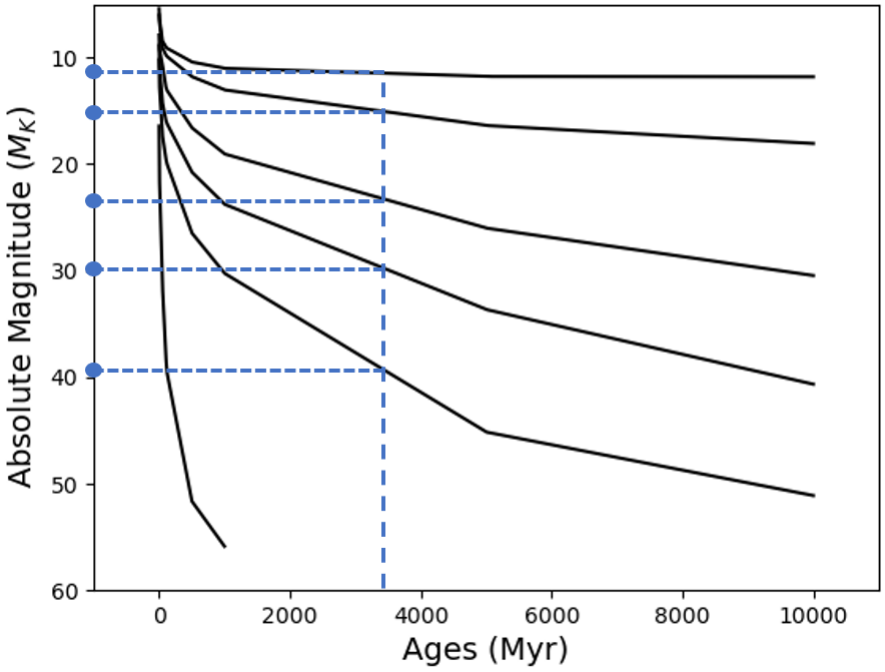

(b) Examples of interpolations done to find all the absolute magnitudes that correspond to a specific age and a specific mass. Dashed blue lines shows examples of how absolute magnitudes are matched to specific ages at specific masses (black solid lines).

Figure 4.8: First interpolation to find all the absolute magnitudes for one age and one mass.

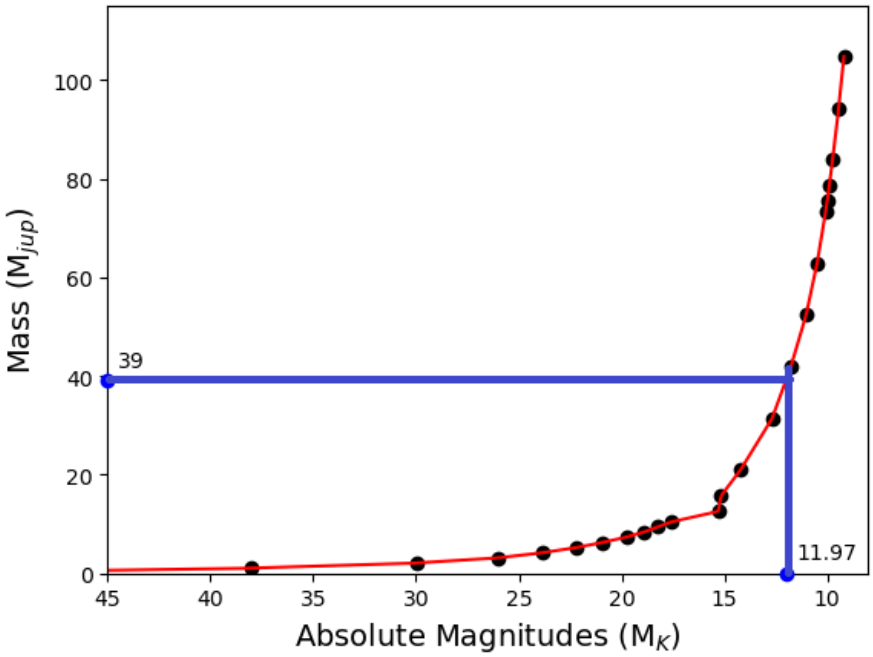

Figure 4.9: The second interpolation used to find mass given a specific age. Red line is the interpolation between the black data points and the blue lines represent how the absolute magnitude for a given star at a given age is matched with a mass using this interpolation.

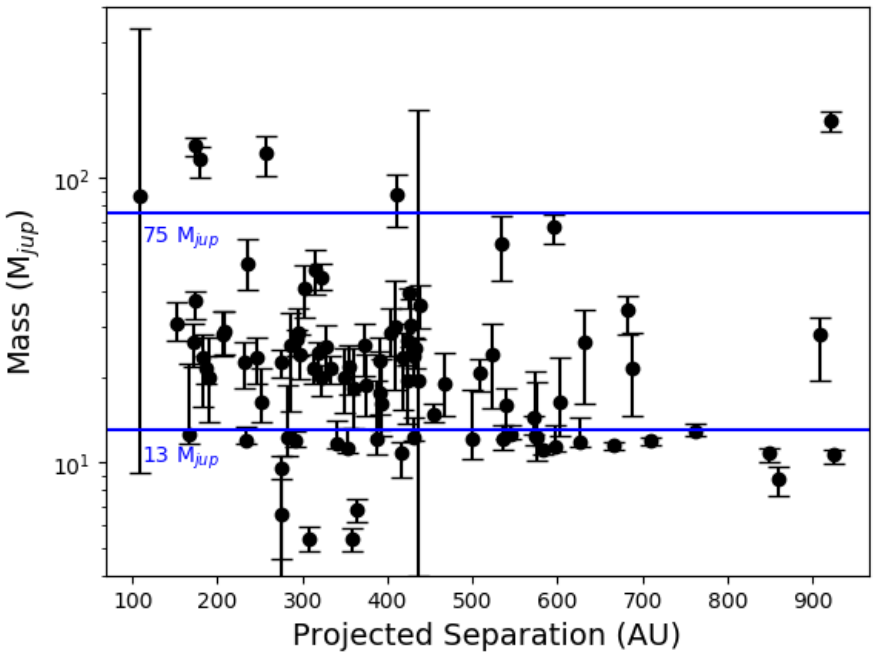

Figure 4.10: Masses and projected separations for all 91 candidate companions from 04 June 2014, most of which are likely background stars. Follow-up observations are necessary to determine which, if any, are bound companions. The blue lines represent the brown dwarf mass limits.

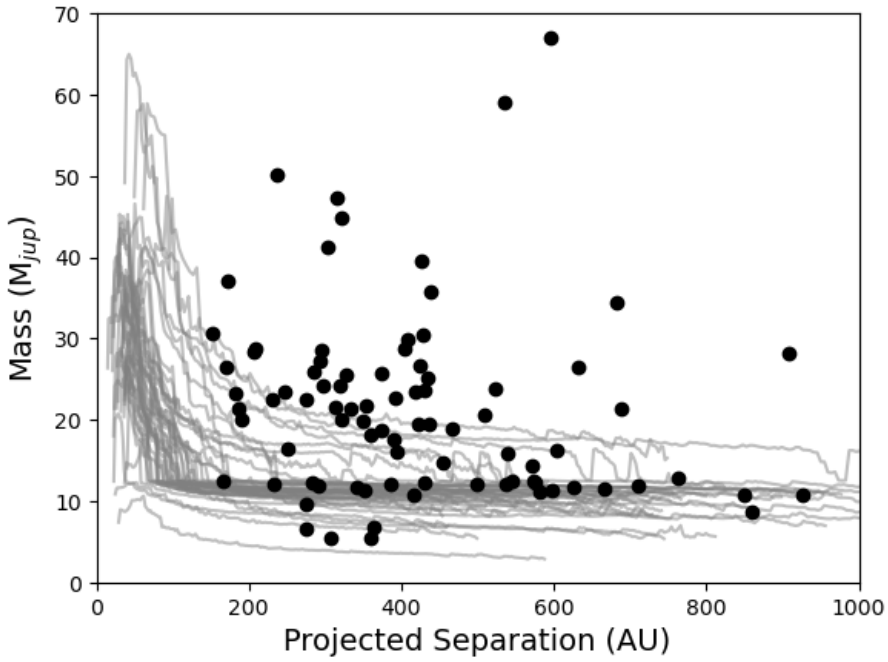

Figure 4.11: Contrast curves of all stars from the night of 04 June 2014 with and without companions showing the sensitivity achieved by this survey. These contrast curves show that this survey is able to detect candidate companions down to the $13M_{Jup}$ lower limit of brown dwarf mass.

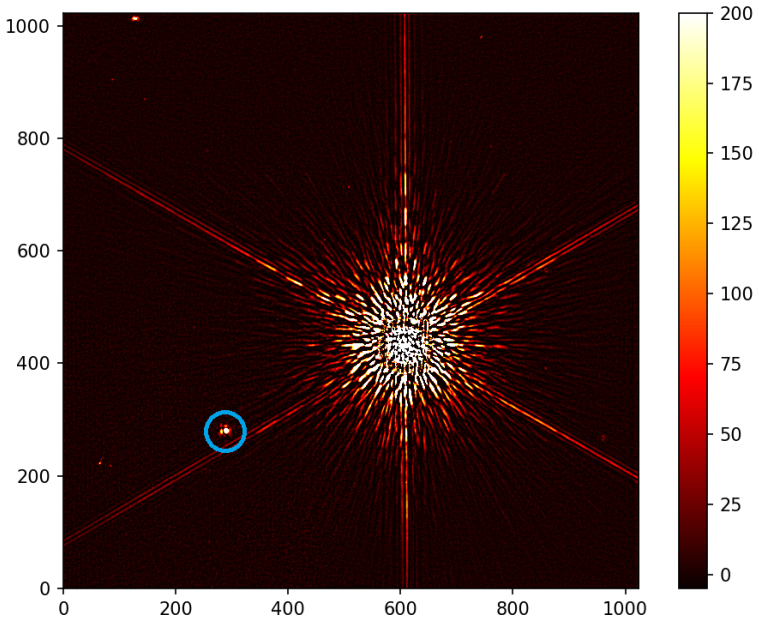

(a)

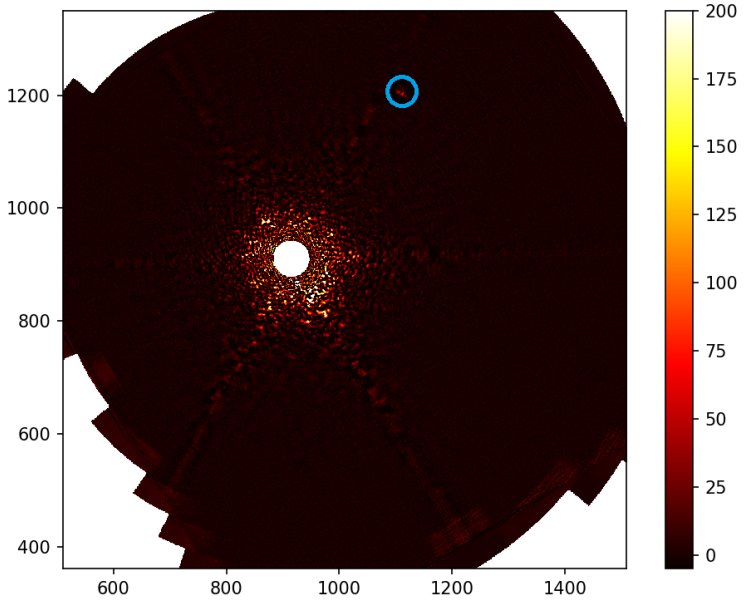

(b)

Figure 4.12: The left figure shows the pre-KLIP image of the star HIP 14544 from the night of 17 Dec 2013. The right image shows the post-KLIP image of this star. The candidate companion is clearly visible before performing the pyKLIP routine, however, afterwards it has mostly been subtracted out.

Chapter 5

SUMMARY AND FUTURE WORK

This survey found 95 candidate companions around 22 stars from the night of 04 June 2014. Separations, magnitudes and masses were calculated for 91 of these candidates around 20 stars. From this we can put an upper limit on stellar companion frequency of 6.6% and an upper limit on brown dwarf companion frequency of 93%. The stellar companion frequency was calculated by dividing the number of candidates found with masses above $75M_{Jup}$ from the night of 04 June 2014 by the number of stars observed that night. The brown dwarf companion frequency was calculated similarly, by dividing the number of candidates found with masses between $13M_{Jup}$ and $75M_{Jup}$ by the number of stars observed that night. These numbers are very high compared to literature values (e.g. $0.8^{+0.8}_{-0.5}$% from GPIES (Nielsen *et al.*, 2019)) and are also not corrected for biases due to known binary systems. Most of these candidate companions are probably background stars, so once more observations are taken, a more accurate upper limit can be calculated. The median sensitivity of this survey is a ΔK of 12.6 at 1" and a ΔK of 15.1 at 3.6". The sensitivity achieved also reaches the lower limit of brown dwarf masses ($13M_{jup}$).

Future work will require more observations of these same stars as well as archive searches for existing observations in order to determine if a candidate companion is gravitationally bound to the star. For the candidate companion to be orbiting the star it must move with the same proper motion as as its host. This can only be known by using second observations of each star with candidates at least a few years after the initial observations. Table 5.1 shows the proper motion for each star that has candidates as well as their anticipated motion in pixels from the date of

observation 8 years ago. A Keck proposal[1] has already been submitted to obtain more observations of the 32 stars, including the ones identified in this survey that have candidate companions. The Keck Archive of more than 300 stars will also be searched as second observations of the stars of interest may already exist. Appendix C includes fully reduced images of each of the 45 stars in the night of 04 June 2014. This represents 1/4 of the full survey.

The reduction pipeline presented in this thesis will be used to reduce the new observations as well as the rest of the data currently available once the pyKLIP rotation problem is corrected. Follow-up observations will need to occur as more stars are found to have candidate companions.

[1]NASA-Keck Project #74, Semester 2022B, PI: Marah Brinjikji

Table 5.1: Proper motions of stars with candidates from 04 June 2014

Target	RA Proper[B] Motion (mas/yr)	DEC Proper[B] Motion (mas/yr)	Anticipated Motion (RA) (pixels)	Anticipated Motion (DEC) (pixels)	Time in between epochs (yrs)
HIP90762	-31.857	-21.397	-25.4856	-17.1176	8
HIP101421	11.96[A]	-28.97[A]	9.568	-23.176	8
HIP101716	15.349	-11.775	12.2792	-9.42	8
HIP104105	19.63	29.018	15.704	23.2144	8
HIP109521	142.43	35.646	113.944	28.5168	8
HIP61558	-27.992	-20.279	-22.3936	-16.2232	8
HIP81560	-2.383	31.963	-1.9064	25.5704	8
HIP81634	0.471	-10.012	0.3768	-8.0096	8
HIP82402	51.33	-9.057	41.064	-7.2456	8
HIP84880	43.4[A]	2.61[A]	34.72	2.088	8
HIP92041	50.61[A]	1.22[A]	40.488	0.976	8
HIP92312	15.849	-17.889	12.6792	-14.3112	8
HIP98146	9.783	10.351	7.8264	8.2808	8
HIP86565	-72.9[A]	-55.55[A]	-58.32	-44.44	8
HIP94833	-13.903	-25.558	-11.1224	-20.4464	8
HIP95951	-1.078	-1.54	-0.8624	-1.232	8
HIP87813	-1.602	-72.684	-1.2816	-58.1472	8
HIP97416	6.569	13.611	5.2552	10.8888	8
HIP90806	-4.892	-21.92	-3.9136	-17.536	8
HIP105282	14.398	2.137	11.5184	1.7096	8

[A]van Leeuwen (2007),[B]Gaia Collaboration (2020)

The HIPPARCOS and TYCHO catalogues. Astrometric and photometric star catalogues derived from the ESA HIPPARCOS Space Astrometry Mission, vol. 1200 of *ESA Special Publication* (1997).

Abt, H. A. and N. I. Morrell, "The Relation between Rotational Velocities and Spectral Peculiarities among A-Type Stars", **99**, 135 (1995).

Arcos, C., S. Kanaan, J. Chávez, L. Vanzi, I. Araya and M. Curé, "Stellar parameters and H α line profile variability of Be stars in the BeSOS survey", **474**, 4, 5287–5299 (2018).

Baraffe, I., G. Chabrier, T. S. Barman, F. Allard and P. H. Hauschildt, "Evolutionary models for cool brown dwarfs and extrasolar giant planets. The case of HD 209458", **402**, 701–712 (2003).

Basri, G., "The Lithium Test for Young Brown Dwarfs (invited review)", in "Brown Dwarfs and Extrasolar Planets", edited by R. Rebolo, E. L. Martin and M. R. Zapatero Osorio, vol. 134 of *Astronomical Society of the Pacific Conference Series*, p. 394 (1998).

Basri, G., "Observations of Brown Dwarfs", **38**, 485–519 (2000).

Beckers, J. M., "Adaptive Optics for Astronomy: Principles, Performance, and Applications", **31**, 13–62 (1993).

Boss, A. P., "Gas Giant Protoplanet Formation: Disk Instability Models with Thermodynamics and Radiative Transfer", **563**, 1, 367–373 (2001).

Bowler, B. P., "Imaging Extrasolar Giant Planets", **128**, 968, 102001 (2016).

Burrows, A., W. B. Hubbard, J. I. Lunine and J. Liebert, "The theory of brown dwarfs and extrasolar giant planets", Reviews of Modern Physics **73**, 3, 719–765 (2001).

Cannon, A. J. and E. C. Pickering, "VizieR Online Data Catalog: Henry Draper Catalogue and Extension (Cannon+ 1918-1924; ADC 1989)", VizieR Online Data Catalog p. III/135A (1993).

Carroll, B. W. and D. A. Ostlie, *An introduction to modern astrophysics, second edition* (2017).

Chesneau, O., L. Dessart, D. Mourard, P. Bério, C. Buil, D. Bonneau, M. Borges Fernandes, J. M. Clausse, O. Delaa, A. Marcotto, A. Meilland, F. Millour, N. Nardetto, K. Perraut, A. Roussel, A. Spang, P. Stee, I. Tallon-Bosc, H. McAlister, T. ten Brummelaar, J. Sturmann, L. Sturmann, N. Turner, C. Farrington and P. J. Goldfinger, "Time, spatial, and spectral resolution of the Hα line-formation region of Deneb and Rigel with the VEGA/CHARA interferometer", **521**, A5 (2010).

Cutri, R. M., M. F. Skrutskie, S. van Dyk, C. A. Beichman, J. M. Carpenter, T. Chester, L. Cambresy, T. Evans, J. Fowler, J. Gizis, E. Howard, J. Huchra, T. Jarrett, E. L. Kopan, J. D. Kirkpatrick, R. M. Light, K. A. Marsh, H. McCallon, S. Schneider, R. Stiening, M. Sykes, M. Weinberg, W. A. Wheaton, S. Wheelock and N. Zacarias, "VizieR Online Data Catalog: 2MASS All-Sky Catalog of Point Sources (Cutri+ 2003)", VizieR Online Data Catalog p. II/246 (2003a).

Cutri, R. M., M. F. Skrutskie, S. van Dyk, C. A. Beichman, J. M. Carpenter, T. Chester, L. Cambresy, T. Evans, J. Fowler, J. Gizis, E. Howard, J. Huchra, T. Jarrett, E. L. Kopan, J. D. Kirkpatrick, R. M. Light, K. A. Marsh, H. McCallon, S. Schneider, R. Stiening, M. Sykes, M. Weinberg, W. A. Wheaton, S. Wheelock and N. Zacarias, "VizieR Online Data Catalog: 2MASS All-Sky Catalog of Point Sources (Cutri+ 2003)", VizieR Online Data Catalog p. II/246 (2003b).

Davies, R. and M. Kasper, "Adaptive Optics for Astronomy", **50**, 305–351 (2012).

De Rosa, R. J., J. Bulger, J. Patience, B. Leland, B. Macintosh, A. Schneider, I. Song, C. Marois, J. R. Graham, M. Bessell and R. Doyon, "The Volume-limited A-Star (VAST) survey - I. Companions and the unexpected X-ray detection of B6-A7 stars", **415**, 1, 854–866 (2011).

De Rosa, R. J., J. Patience, P. A. Wilson, A. Schneider, N. J. McConnell, S. Wiktorowicz, C. Marois, I. Song, B. Macintosh, J. R. Graham, M. S. Bessell, R. Doyon, O. Lai and S. Thomas, "The VAST Survey - On the Multiplicity of A-type Stars", in "American Astronomical Society Meeting Abstracts #221", vol. 221 of *American Astronomical Society Meeting Abstracts*, p. 423.06 (2013).

Delfosse, X., C. G. Tinney, T. Forveille, N. Epchtein, E. Bertin, J. Borsenberger, E. Copet, B. de Batz, P. Fouque, S. Kimeswenger, T. Le Bertre, F. Lacombe, D. Rouan and D. Tiphene, "Field brown dwarfs found by DENIS", **327**, L25–L28 (1997).

Ducati, J. R., "VizieR Online Data Catalog: Catalogue of Stellar Photometry in Johnson's 11-color system.", VizieR Online Data Catalog (2002).

Duchêne, G. and A. Kraus, "Stellar Multiplicity", **51**, 1, 269–310 (2013).

Dupuy, T. J. and M. C. Liu, "Individual Dynamical Masses of Ultracool Dwarfs", **231**, 2, 15 (2017).

Filippazzo, J. C., E. L. Rice, J. Faherty, K. L. Cruz, M. M. Van Gordon and D. L. Looper, "Fundamental Parameters and Spectral Energy Distributions of Young and Field Age Objects with Masses Spanning the Stellar to Planetary Regime", **810**, 2, 158 (2015).

Gaia Collaboration, "VizieR Online Data Catalog: Gaia EDR3 (Gaia Collaboration, 2020)", VizieR Online Data Catalog p. I/350 (2020).

Gennaro, M. and M. Robberto, "HST Survey of the Orion Nebula Cluster in the H_2O 1.4 μm Absorption Band. II. The Substellar IMF Down to Planetary Masses", **896**, 1, 80 (2020).

Gray, R. O., C. J. Corbally, R. F. Garrison, M. T. McFadden, E. J. Bubar, C. E. McGahee, A. A. O'Donoghue and E. R. Knox, "Contributions to the Nearby Stars (NStars) Project: Spectroscopy of Stars Earlier than M0 within 40 pc-The Southern Sample", **132**, 1, 161–170 (2006).

Gray, R. O., C. J. Corbally, R. F. Garrison, M. T. McFadden and P. E. Robinson, "Contributions to the Nearby Stars (NStars) Project: Spectroscopy of Stars Earlier than M0 within 40 Parsecs: The Northern Sample. I.", **126**, 4, 2048–2059 (2003).

Grether, D. and C. H. Lineweaver, "How Dry is the Brown Dwarf Desert? Quantifying the Relative Number of Planets, Brown Dwarfs, and Stellar Companions around Nearby Sun-like Stars", **640**, 2, 1051–1062 (2006).

Hampson, K. M., R. Turcotte, D. T. Millers, K. Kurokawa, J. R. Males, N. Ji and M. J. Booth, "Adaptive optics for high-resolution imaging", Nat Rev Methods Primers **68** (2021).

Høg, E., C. Fabricius, V. V. Makarov, S. Urban, T. Corbin, G. Wycoff, U. Bastian, P. Schwekendiek and A. Wicenec, "The Tycho-2 catalogue of the 2.5 million brightest stars", **355**, L27–L30 (2000).

Houk, N., *Michigan Catalogue of Two-dimensional Spectral Types for the HD stars. Volume_3. Declinations -40_f0 to -26_f0.* (1982).

Houk, N. and M. Smith-Moore, *Michigan Catalogue of Two-dimensional Spectral Types for the HD Stars. Volume 4, Declinations -26°.0 to -12°.0.*, vol. 4 (1988).

Houk, N. and C. Swift, "Michigan catalogue of two-dimensional spectral types for the HD Stars, Vol. 5", Michigan Spectral Survey **5**, 0 (1999).

Hube, D. P., "The radial velocities of 335 late B-type stars", **72**, 233 (1970).

Joye, W. A. and E. Mandel, "New Features of SAOImage DS9", in "Astronomical Data Analysis Software and Systems XII", edited by H. E. Payne, R. I. Jedrzejewski and R. N. Hook, vol. 295 of *Astronomical Society of the Pacific Conference Series*, p. 489 (2003).

Kiefer, F., G. Hébrard, J. Sahlmann, S. G. Sousa, T. Forveille, N. Santos, M. Mayor, M. Deleuil, P. A. Wilson, S. Dalal, R. F. Díaz, G. W. Henry, J. Hagelberg, M. J. Hobson, O. Demangeon, V. Bourrier, X. Delfosse, L. Arnold, N. Astudillo-Defru, J. L. Beuzit, I. Boisse, X. Bonfils, S. Borgniet, F. Bouchy, B. Courcol, D. Ehrenreich, N. Hara, A. M. Lagrange, C. Lovis, G. Montagnier, C. Moutou, F. Pepe, C. Perrier, J. Rey, A. Santerne, D. Ségransan, S. Udry and A. Vidal-Madjar, "Detection and characterisation of 54 massive companions with the SOPHIE spectrograph. Seven new brown dwarfs and constraints on the brown dwarf desert", **631**, A125 (2019).

Kumar, S. S., "The Structure of Stars of Very Low Mass.", **137**, 1121 (1963).

Levenhagen, R. S. and N. V. Leister, "Spectroscopic analysis of southern B and Be stars", **371**, 1, 252–262 (2006).

Loden, L. O., "A physical study of the Ursa Major cluster (with special attention tothe peculiar A stars)", **53**, 33–42 (1983).

Lyot, B., "The study of the solar corona and prominences without eclipses (George Darwin Lecture, 1939)", **99**, 580 (1939).

Nakajima, T., B. R. Oppenheimer, S. R. Kulkarni, D. A. Golimowski, K. Matthews and S. T. Durrance, "Discovery of a cool brown dwarf", **378**, 6556, 463–465 (1995).

Nielsen, E. L. and L. M. Close, "A Uniform Analysis of 118 Stars with High-contrast Imaging: Long-period Extrasolar Giant Planets are Rare Around Sun-like Stars", **717**, 2, 878–896 (2010).

Nielsen, E. L., L. M. Close, B. A. Biller, E. Masciadri and R. Lenzen, "Constraints on Extrasolar Planet Populations from VLT NACO/SDI and MMT SDI and Direct Adaptive Optics Imaging Surveys: Giant Planets are Rare at Large Separations", **674**, 1, 466–481 (2008).

Nielsen, E. L., R. J. De Rosa, B. Macintosh, J. J. Wang, J.-B. Ruffio, E. Chiang, M. S. Marley, D. Saumon, D. Savransky, S. M. Ammons, V. P. Bailey, T. Barman, C. Blain, J. Bulger, A. Burrows, J. Chilcote, T. Cotten, I. Czekala, R. Doyon, G. Duchêne, T. M. Esposito, D. Fabrycky, M. P. Fitzgerald, K. B. Follette, J. J. Fortney, B. L. Gerard, S. J. Goodsell, J. R. Graham, A. Z. Greenbaum, P. Hibon, S. Hinkley, L. A. Hirsch, J. Hom, L.-W. Hung, R. I. Dawson, P. Ingraham, P. Kalas, Q. Konopacky, J. E. Larkin, E. J. Lee, J. W. Lin, J. Maire, F. Marchis, C. Marois, S. Metchev, M. A. Millar-Blanchaer, K. M. Morzinski, R. Oppenheimer, D. Palmer, J. Patience, M. Perrin, L. Poyneer, L. Pueyo, R. R. Rafikov, A. Rajan, J. Rameau, F. T. Rantakyrö, B. Ren, A. C. Schneider, A. Sivaramakrishnan, I. Song, R. Soummer, M. Tallis, S. Thomas, K. Ward-Duong and S. Wolff, "The Gemini Planet Imager Exoplanet Survey: Giant Planet and Brown Dwarf Demographics from 10 to 100 au", **158**, 1, 13 (2019).

Nielsen, E. L., M. C. Liu, Z. Wahhaj, B. A. Biller, T. L. Hayward, L. M. Close, J. R. Males, A. J. Skemer, M. Chun, C. Ftaclas, S. H. P. Alencar, P. Artymowicz, A. Boss, F. Clarke, E. de Gouveia Dal Pino, J. Gregorio-Hetem, M. Hartung, S. Ida, M. Kuchner, D. N. C. Lin, I. N. Reid, E. L. Shkolnik, M. Tecza, N. Thatte and D. W. Toomey, "The Gemini NICI Planet-Finding Campaign: The Frequency of Giant Planets around Young B and A Stars", **776**, 1, 4 (2013).

Oja, T., "UBV photometry of stars whose positions are accurately known. VI.", **89**, 415 (1991).

Oja, T., "UBV photometry of stars whose positions are accurately known. VII.", **100**, 591–592 (1993).

Oppenheimer, B. R. and S. Hinkley, "High-Contrast Observations in Optical and Infrared Astronomy", **47**, 1, 253–289 (2009).

Paunzen, E., B. Duffee, U. Heiter, R. Kuschnig and W. W. Weiss, "A spectroscopic survey for lambda Bootis stars. II. The observational data", **373**, 625–632 (2001).

Pecaut, M. J. and E. E. Mamajek, "Intrinsic Colors, Temperatures, and Bolometric Corrections of Pre-main-sequence Stars", **208**, 1, 9 (2013).

Raghavan, D., H. A. McAlister, T. J. Henry, D. W. Latham, G. W. Marcy, B. D. Mason, D. R. Gies, R. J. White and T. A. ten Brummelaar, "A Survey of Stellar Families: Multiplicity of Solar-type Stars", **190**, 1, 1–42 (2010).

Rebolo, R., M. R. Zapatero Osorio and E. L. Martín, "Discovery of a brown dwarf in the Pleiades star cluster", **377**, 6545, 129–131 (1995).

Royer, F., J. Zorec and A. E. Gómez, "Rotational velocities of A-type stars. III. Velocity distributions", **463**, 2, 671–682 (2007).

Sana, H., J. B. Le Bouquin, S. Lacour, J. P. Berger, G. Duvert, L. Gauchet, B. Norris, J. Olofsson, D. Pickel, G. Zins, O. Absil, A. de Koter, K. Kratter, O. Schnurr and H. Zinnecker, "Southern Massive Stars at High Angular Resolution: Observational Campaign and Companion Detection", **215**, 1, 15 (2014).

Sivaramakrishnan, A., C. D. Koresko, R. B. Makidon, T. Berkefeld and M. J. Kuchner, "Ground-based Coronagraphy with High-order Adaptive Optics", **552**, 1, 397–408 (2001).

Soummer, R., L. Pueyo and J. Larkin, "Detection and Characterization of Exoplanets and Disks Using Projections on Karhunen-Loève Eigenimages", **755**, 2, L28 (2012).

Troup, N. W., D. L. Nidever, N. De Lee, J. Carlberg, S. R. Majewski, M. Fernandez, K. Covey, S. D. Chojnowski, J. Pepper, D. T. Nguyen, K. Stassun, D. C. Nguyen, J. P. Wisniewski, S. W. Fleming, D. Bizyaev, P. M. Frinchaboy, D. A. García-Hernández, J. Ge, F. Hearty, S. Meszaros, K. Pan, C. Allende Prieto, D. P. Schneider, M. D. Shetrone, M. F. Skrutskie, J. Wilson and O. Zamora, "Companions to APOGEE Stars. I. A Milky Way-spanning Catalog of Stellar and Substellar Companion Candidates and Their Diverse Hosts", **151**, 3, 85 (2016).

van Belle, G. T. and K. von Braun, "Directly Determined Linear Radii and Effective Temperatures of Exoplanet Host Stars", **694**, 2, 1085–1098 (2009).

van Leeuwen, F., "Validation of the new Hipparcos reduction", **474**, 2, 653–664 (2007).

Vorobyov, E. I., "Formation of giant planets and brown dwarfs on wide orbits", **552**, A129 (2013).

Vorobyov, E. I. and S. Basu, "Formation of free-floating and companion brown dwarfs.", **84**, 4, 866 (2013).

Wang, J. J., J.-B. Ruffio, R. J. De Rosa, J. Aguilar, S. G. Wolff and L. Pueyo, "pyKLIP: PSF Subtraction for Exoplanets and Disks", (2015).

Wenger, M., F. Ochsenbein, D. Egret, P. Dubois, F. Bonnarel, S. Borde, F. Genova, G. Jasniewicz, S. Laloë, S. Lesteven and R. Monier, "The SIMBAD astronomical database. The CDS reference database for astronomical objects", **143**, 9–22 (2000).

Yelda, S., J. R. Lu, A. M. Ghez, W. Clarkson, J. Anderson, T. Do and K. Matthews, "Improving Galactic Center Astrometry by Reducing the Effects of Geometric Distortion", **725**, 1, 331–352 (2010).

Zorec, J., L. Cidale, M. L. Arias, Y. Frémat, M. F. Muratore, A. F. Torres and C. Martayan, "Fundamental parameters of B supergiants from the BCD system. I. Calibration of the (λ_1, D) parameters into T_{eff}", **501**, 1, 297–320 (2009).

APPENDIX A

STAR PROPERTIES FOR 04 JUNE 2014 AND 17 DEC 2013

Ages of these stars are from Nielsen *et al.* (2013). The ages for HIP 90752, HIP 82216, HIP 79007, HIP 68756, HIP 46813, and HIP 84012 were calculated using a slightly altered version of this method where the model grid was not allowed to go below 10Myr. All the RA, DEC, and parallax data is from either the Gaia Early Data Release 3 (Gaia Collaboration, 2020) or the Hipparcos Catalog (van Leeuwen, 2007). Most of the V-magnitudes are from Tycho 2 (Høg *et al.*, 2000) and most of the K-magnitudes are from the Two Micron All Sky Survey (2MASS) (Cutri *et al.*, 2003b). The remaining magnitudes are from sources listed in the footnote of the table. The spectral types for each star come from a variety of sources and studies, also listed in the footnote of the table. Errors in K magnitude of HIP 32838, HIP 24305, HIP 5542, and HIP 4436 were estimated from other stars with similar magnitudes. HIP 84012 was not reduced with the pipeline and HIP 109754, HIP 109831, and HIP 85391 were reduced but their candidates were not analyzed and are not included in the total count of 95 candidates found for 04 June 2014.

Table A.1: Star Properties

Date	Star	RA[Z]	DEC[Z]	Parallax[Z]	Distance to Star (pc)	V[L]	K[O]	SpT[K]	Age[X] (Myr)
6/4/2014	HIP106363	21:32:33.261	-24:35:25.508	13.59±0.0373	73.584±0.202	6.428 ±0.01	5.947±0.018	A7	495^{+161}_{-170}
6/4/2014	HIP107517	21:46:32.097	-11:21:57.450	11.86±0.0711	84.317±0.505	5.567 ±0.009	5.568±0.023	A0[J]	308^{+38}_{-41}
6/4/2014	HIP101469	20:33:49.379	-29:17:33.424	13.53±0.24	73.91±1.311	7.037 ±0.007	6.297±0.017	A9[B]	510^{+275}_{-264}
6/4/2014	HIP108339	21:56:56.372	+12:04:35.360	7.58±0.0259	131.926±0.451	5.533 ±0.003	5.359±0.016	A2	286^{+11}_{-285}
6/4/2014	HIP106783	21:37:43.645	+06:37:06.205	11.33±0.1305	88.261±1.017	6.177 ±0.009	6.112±0.015	A2	294^{+82}_{-83}
6/4/2014	HIP108060	21:53:37.388[S]	+19:40:06.469[S]	14.96±0.0458	66.845±0.205	5.676 ±0.01	5.631±0.024	A0	226^{+76}_{-73}
6/4/2014	HIP101421	20:33:12.771[T]	+11:18:11.741[T]	9.87±0.0977[T]	101.317±1.003	4.03 ±0.009[N]	4.381±0.02	B6[V]	70^{+5}_{-6}
6/4/2014	HIP92041	18:45:39.386[T]	-26:59:26.794[T]	13.63±0.21[T]	73.368±1.13	3.14 ±0.003	3.28±0.036	B8	74^{+3}_{-4}
6/4/2014	HIP114714	23:14:14.381	+50:37:04.420	8.41±0.19	118.906±2.686	6.31 ±0.009[E]	6.321±0.312	A0	296^{+42}_{-37}
6/4/2014	HIP109745	22:13:49.240	+45:26:26.195	12.82±0.0309	78.003±0.188	5.53 ±0.009[E]	5.473±0.018	A0	323^{+36}_{-43}
6/4/2014	HIP101716	20:37:04.672	+26:27:43.000	10.89±0.0483	91.827±0.407	5.583 ±0.009	5.712±0.016	B8*A*	191^{+30}_{-30}
6/4/2014	HIP94833	19:17:48.193	+02:01:54.245	10.99±0.1497	90.992±1.239	6.174 ±0.01	6.042±0.023	A0[J]	211^{+84}_{-77}
6/4/2014	HIP109521	22:11:09.893	+50:49:24.284	17.83±0.066	56.085±0.208	5.377 ±0.009	4.959±0.016	A5	528^{+93}_{-84}
6/4/2014	HIP90806	18:31:26.297	-18:24:09.706	15.29±0.0845	65.402±0.361	5.117 ±0.009	5.067±0.023	B9[D]	333^{+29}_{-39}
6/4/2014	HIP105282	21:19:28.750	+49:30:37.063	5.93±0.0586	168.634±1.666	5.74 ±0.001[I]	6.076±0.016	B6	66^{+10}_{-13}
6/4/2014	HIP97416	19:47:59.643	+31:30:22.597	10.45±0.0231	95.694±0.212	6.795 ±0.01	6.577±0.021	A0[G]	290^{+141}_{-143}
6/4/2014	HIP95951	19:30:45.396	+27:57:54.974	8.38±0.0781	119.332±1.112	5.11 ±0.003[N]	5.258±0.017	B8[R]	103^{+13}_{-15}
6/4/2014	HIP87813	17:56:19.035	-15:48:45.100	12.38±0.0976	80.775±0.637	5.929 ±0.01	5.698±0.02	A0[D]	199^{+91}_{-81}
6/4/2014	HIP85391	17:26:55.296	-25:56:36.478	8.01±0.0612	124.844±0.954	6.43 ±0.013[I]	6.528±0.018	B9[D]	112^{+50}_{-59}
6/4/2014	HIP97376	19:47:27.779	+38:24:27.408	7.14±0.0439	140.056±0.861	5.824 ±0.009	6.015±0.018	B8	116^{+28}_{-20}
6/4/2014	HIP86565	17:41:24.872[T]	-12:52:31.109[T]	18.83±0.25[T]	53.107±0.705	4.228 ±0.009	4.107±0.248	A2[D]	370^{+11}_{-20}
6/4/2014	HIP92312	18:48:53.386	+19:19:43.380	11.1±0.0423	90.09±0.343	5.88 ±0.009	5.82±0.016	A1	310^{+44}_{-49}
6/4/2014	HIP98146	19:56:45.172	+50:54:09.075	9.38±0.0272	106.61±0.309	6.455 ±0.01	6.484±0.018	A1	213^{+72}_{-64}
6/4/2014	HIP90762	18:31:04.448	+16:55:42.803	7.99±0.0644	125.156±1.009	5.75 ±0.009	5.479±0.02	A2	347^{+11}_{-54}
6/4/2014	HIP99655	20:13:23.866[T]	+56:34:03.800[T]	20.48±0.12[T]	48.828±0.286	4.271 ±0.009	4.078±0.378	A3	443^{+14}_{-48}
6/4/2014	HIP84880	17:20:49.661[T]	-12:50:48.753[T]	16.05±0.26[T]	62.305±1.009	4.324 ±0.009	4.188±0.021	A0[D]	292^{+53}_{-290}
6/4/2014	HIP94280	19:11:23.162	+40:25:44.731	6.42±0.1277	155.763±3.098	6.188 ±0.01	5.918±0.02	A3	370^{+11}_{-368}
6/4/2014	HIP95853	19:29:42.358[T]	+51:43:47.206[T]	26.88±0.11[T]	37.202±0.152	3.755 ±0.009	3.598±0.282	A5[W]	476^{+12}_{-11}
6/4/2014	HIP104105	21:05:29.265	+78:07:35.010	7.14±0.0622	140.056±1.22	5.907 ±0.009	6.084±0.024	B8	143^{+35}_{-27}
6/4/2014	HIP87341	17:50:48.382	+22:18:58.794	10.7±0.0208	93.458±0.182	6.13 ±0.009[E]	5.449±0.023	A9	647^{+16}_{-16}
6/4/2014	HIP85790	17:31:49.579	+28:24:27.000	11.99±0.0407	83.403±0.283	5.65 ±0.009[E]	5.642±0.031	A1	283^{+39}_{-39}
6/4/2014	HIP82216	16:47:46.420	+05:14:48.279	8.2±0.1147	121.951±1.706	5.24 ±0.003[F]	5.098±0.02	A1[H]	292^{+6}_{-7}
6/4/2014	HIP82402	16:50:19.380	+07:14:51.660	16.92±0.0604	59.102±0.211	5.469 ±0.009	5.226±0.031	A3	366^{+104}_{-110}
6/4/2014	HIP81634	16:40:35.150	+04:12:25.928	10.02±0.027	99.8±0.269	6.93 ±0.007[I]	6.659±0.031	B9[J]	306^{+154}_{-148}

Continued on next page

Table A.1 – *Continued from previous page*

Date	Star	RA^{Z}	DEC^{Z}	Parallax^{Z}	Distance to Star (pc)	V^{L}	K^{O}	SpT^{K}	Age^{X} (Myr)
6/4/2014	HIP81560	16:39:26.071	+29:13:05.615	10.64±0.0206	93.985±0.182	7.24 ±0.01	6.819±0.017	A0^{G}	281^{+195}_{-178}
6/4/2014	HIP79007	16:07:37.539	+09:53:30.265	9.72±0.203	102.881±2.149	5.635 ±0.009	5.094±0.017	A7^{U}	478^{+10}_{-10}
6/4/2014	HIP80809	16:30:06.039	+48:57:39.881	8.92±0.1694	112.108±2.129	6.427 ±0.014	6.385±0.018	A1	262^{+76}_{-81}
6/4/2014	HIP76866	15:41:47.414	+12:50:51.094	14.55±0.0748	68.729±0.353	5.33 ±0.003^{F}	5.201±0.02	A2^{C}	323^{+43}_{-52}
6/4/2014	HIP76957	15:42:50.760	+52:21:39.244	10.81±0.0499	92.507±0.427	5.482 ±0.009	5.559±0.018	A0^{H}	214^{+40}_{-29}
6/4/2014	HIP68756	14:04:23.349^{T}	+64:22:33.062^{T}	10.76±0.17^{T}	92.937±1.468	3.68 ±0.009^{G}	3.639±0.272	A0	75^{+2}_{-1}
6/4/2014	HIP75953	15:30:46.069	+34:27:56.365	9.02±0.0254	110.865±0.312	6.809 ±0.01	6.704±0.018	A0^{G}	213^{+97}_{-91}
6/4/2014	HIP61558	12:36:47.354	-05:49:54.841	14.0±0.0477	71.429±0.243	5.88 ±0.003^{I}	5.703±0.017	A3^{M}	301^{+92}_{-103}
6/4/2014	HIP74505	15:13:31.870	+22:59:00.221	8.47±0.1436	118.064±2.002	6.298 ±0.01	6.101±0.02	A2	305^{+88}_{-96}
6/4/2014	HIP69650	14:15:16.995	+52:32:09.324	10.59±0.0223	94.429±0.199	6.56 ±0.01	6.367±0.021	A4^{S}	359^{+97}_{-103}
6/4/2014	HIP71618	14:38:50.225	+44:24:16.198	17.39±0.1516	57.504±0.501	5.387 ±0.009	5.26±0.02	A1	207^{+91}_{-80}
6/4/2014	HIP66200	13:34:07.931^{T}	+03:39:32.274^{T}	17.65±0.2^{T}	56.657±0.642	4.94 ±0.002^{F}	4.879±0.02	A7^{J}	317^{+43}_{-51}
6/4/2014	HIP61937	12:41:34.391	+10:25:34.568	14.05±0.0342	71.174±0.173	6.215 ±0.01	5.653±0.016	A6^{H}	485^{+155}_{-157}
6/4/2014	HIP84012	17:10:22.686^{T}	-15:43:29.664^{T}	36.91±0.08^{T}	27.093±0.059	2.42 ±0.01^{N}	2.27±0.02^{N}	A2^{Q}	371^{+10}_{-74}
6/4/2014	HIP109831	22:14:44.361	+42:57:14.039	12.1647±0.0634	82.205±0.428	5.72 ±0.009^{E}	5.659±0.029	A2	303^{+42}_{-45}
12/17/13	HIP 114984	23:17:18.898	+75:17:56.494	6.207±0.1037	161.108 ±2.692	6.34±0.009	6.185 ±0.017	A2	289^{+9}_{-287}
12/17/13	HIP 10814	02:19:10.824	+46:28:20.141	7.2162±0.0385	138.577 ±0.739	6.22±0.009^{E}	5.686 ±0.021	A4	477^{+11}_{-12}
12/17/13	HIP 10732	02:18:07.530	+19:54:04.167	7.222±0.1043	138.466 ±2.0	5.572±0.009	5.39 ±0.023	A1	291^{+7}_{-7}
12/17/13	HIP 38449	07:52:36.426	+55:12:33.976	7.2567±0.0438	137.804 ±0.832	6.37±0.009^{E}	5.783 ±0.017	A0	276^{+43}_{-45}
12/17/13	HIP 36687	07:32:49.349	-02:02:03.745	7.4228±0.0345	134.72 ±0.626	6.82±0.01	6.925 ±0.024	B9^{J}	117^{+69}_{-63}
12/17/13	HIP 46813	09:32:20.408	-19:24:01.096	8.1052±0.0584	123.378 ±0.889	5.74±0.003^{I}	5.337 ±0.015	A4^{D}	380^{+70}_{-12}
12/17/13	HIP 115033	23:17:54.213^{T}	-09:10:57.067^{T}	8.12±0.38^{T}	123.153 ±5.763	4.4±0.003^{E}	4.758 ±0.021	B5^{Y}	477^{+11}_{-12}
12/17/13	HIP 39535	08:04:45.303	+18:50:31.270	8.2402±0.0574	121.356 ±0.845	6.21±0.009^{E}	6.277 ±0.02	B9	159^{+47}_{-59}
12/17/13	HIP 51437	10:30:17.480	-00:38:13.314	8.8899±0.1477	112.487 ±1.869	5.1±0.003^{N}	5.386 ±0.018	B5^{J}	35^{+12}_{-14}
12/17/13	HIP 41578	08:28:37.339	+14:12:38.967	9.0325±0.0336	110.711 ±0.412	5.948±0.01	5.376 ±0.016	A5	472^{+14}_{-469}
12/17/13	HIP 54960	11:15:17.587	-19:38:15.144	9.0555±0.03	110.43 ±0.366	6.88±0.01	6.688 ±0.017	A3^{D}	200^{+131}_{-121}
12/17/13	HIP 10559	02:15:56.287	+33:21:32.032	9.0683±0.137	110.274 ±1.666	5.249±0.009	5.228 ±0.017	A0	285^{+17}_{-18}
12/17/13	HIP 3801	00:48:50.021	+50:58:05.394	9.1537±0.2122	109.245 ±2.533	4.891±0.009	5.144 ±0.018	B9	115^{+3}_{-6}
12/17/13	HIP 16168	03:28:20.700	+33:48:27.207	9.3697±0.1196	106.727 ±1.362	5.73±0.009^{E}	5.549 ±0.018	A2	350^{+9}_{-8}
12/17/13	HIP 43394	08:50:21.636	-28:37:03.428	9.6053±0.0385	104.109 ±0.417	6.168±0.01	6.337 ±0.018	B9^{B}	142^{+39}_{-47}
12/17/13	HIP 32838	06:50:42.303	-08:02:27.587	9.8371±0.0365	101.656 ±0.377	6.29±0.005^{N}	6.231 ±0.021	B9^{J}	253^{+65}_{-68}
12/17/13	HIP 18673	03:59:55.483	-24:00:58.377	9.9739±0.1001	100.262 ±1.006	4.66±0.002^{N}	4.803 ±0.026	B7^{D}	57^{+45}_{-33}
12/17/13	HIP 33056	06:53:07.578	+44:50:23.778	10.0833±0.0439	99.174 ±0.432	6.236±0.01	5.627 ±0.036	A8	625^{+41}_{-53}
12/17/13	HIP 117371	23:47:54.770	+67:48:24.512	10.4629±0.0746	95.576 ±0.681	5.044±0.009	4.967 ±0.023	A1	477^{+11}_{-12}
12/17/13	HIP 16611	03:33:47.276^{T}	-21:37:58.383^{T}	11.12±0.21^{T}	89.928 ±1.698	4.3±0.002^{I}	4.551 ±0.018	B9^{D}	103^{+11}_{-34}
12/17/13	HIP 14544	03:07:47.343	+47:18:31.341	11.6125±0.0393	86.114 ±0.291	6.375±0.01	5.968 ±0.02	A3	399^{+118}_{-111}

Continued on next page

Table A.1 – *Continued from previous page*

Date	Star	RA[Z]	DEC[Z]	Parallax[Z]	Distance to Star (pc)	V[L]	K[O]	SpT[K]	Age[X] (Myr)
12/17/13	HIP 50303	10:16:14.430	+29:18:37.707	11.6971±0.0923	85.491 ±0.675	5.488±0.009	5.387 ±0.017	A0	334^{+29}_{-39}
12/17/13	HIP 28899	06:06:05.539	-29:45:31.046	11.7258±0.0831	85.282 ±0.604	5.784±0.009	5.681 ±0.017	A1[B]	344^{+29}_{-46}
12/17/13	HIP 116714	23:39:10.174	+75:17:34.373	11.7781±0.0325	84.903 ±0.234	5.946±0.009	5.634 ±0.017	A3	477^{+11}_{-12}
12/17/13	HIP 45257	09:13:24.800	+03:49:28.489	11.9051±0.0256	83.998 ±0.181	7.23±0.01	6.594 ±0.017	A3[J]	449^{+331}_{-275}
12/17/13	HIP 24505	05:15:24.372	-26:56:36.629	11.9207±0.0639	83.888 ±0.45	5.04±0.002[I]	5.218 ±0.023	B9[B]	141^{+33}_{-24}
12/17/13	HIP 37609	07:43:00.415[T]	+58:42:37.295[T]	12.22±0.2[T]	81.833 ±1.339	4.947±0.009	4.629 ±0.017	A3	372^{+9}_{-9}
12/17/13	HIP 17453	03:44:28.203	+20:55:43.448	12.3772±0.049	80.794 ±0.32	6.074±0.01	6.031 ±0.023	A0[H]	191^{+92}_{-81}
12/17/13	HIP 9312	01:59:38.037	+64:37:17.760	12.6852±0.0646	78.832 ±0.401	5.278±0.009	5.218 ±9.998	A0	314^{+28}_{-37}
12/17/13	HIP 14791	03:11:00.736	+64:53:46.552	12.6864±0.027	78.825 ±0.168	6.5±0.01	6.079 ±0.02	A4	467^{+139}_{-137}
12/17/13	HIP 6061	01:17:47.956	+03:36:52.088	13.1721±0.1142	75.918 ±0.658	5.137±0.009	4.921 ±0.027	A1[J]	371^{+23}_{-30}
12/17/13	HIP 16599	03:33:39.059	+54:58:29.497	13.1723±0.0317	75.917 ±0.183	5.969±0.01	5.68 ±0.023	A3	441^{+97}_{-90}
12/17/13	HIP 27949	05:54:50.766	+55:42:25.080	13.3702±0.167	74.793 ±0.934	4.96±0.009	4.765 ±0.017	A2	361^{+17}_{-22}
12/17/13	HIP 114822	23:15:34.257	-03:29:46.962	13.435±0.0384	74.432 ±0.213	5.55±0.003[I]	5.404 ±0.023	A2[H]	477^{+11}_{-12}
12/17/13	HIP 29150	06:08:57.869	-22:25:38.616	13.4579±0.0558	74.306 ±0.308	5.48±0.009	5.453 ±0.029	A0[D]	259^{+45}_{-50}
12/17/13	HIP 36917	07:35:22.891	-28:22:09.605	13.6185±0.1393	73.43 ±0.751	4.63±0.002	4.909 ±0.018	B7[A]	25^{+17}_{-15}
12/17/13	HIP 116768	23:39:55.040	+09:40:38.269	14.0509±0.2906	71.17 ±1.472	5.96±0.009	5.471 ±0.023	A2	477^{+11}_{-12}
12/17/13	HIP 39095	07:59:52.047	-18:23:57.180	14.5984±0.038	68.501 ±0.178	4.61±0.004	4.309 ±0.027	A1[D]	372^{+9}_{-9}
12/17/13	HIP 20507	04:23:40.852	-03:44:43.685	15.5196±0.0866	64.435 ±0.36	5.165±0.009	4.926 ±0.021	A1[J]	362^{+19}_{-32}
12/17/13	HIP 27249	05:46:30.389	+56:06:56.072	16.8232±0.0352	59.442 ±0.124	5.927±0.009	5.515 ±0.02	A4	462^{+141}_{-125}
12/17/13	HIP 23554	05:03:53.271	-24:23:17.331	16.9975±0.0397	58.832 ±0.137	5.582±0.009	5.336 ±0.016	A2[D]	328^{+98}_{-117}
12/17/13	HIP 42806	08:43:17.148[T]	+21:28:06.600[T]	18.0±0.21[T]	55.556 ±0.648	4.652±0.009	4.638 ±0.024	A1	327^{+30}_{-42}
12/17/13	HIP 42313	08:37:39.367	+05:42:13.635	18.4301±0.3241	54.259 ±0.954	4.131±0.009	4.033 ±0.036	A0[H]	301^{+17}_{-25}
12/17/13	HIP 3414	00:43:28.069	+47:01:28.364	18.6293±0.1142	53.679 ±0.329	4.949±0.009	4.584 ±0.016	A5[U]	559^{+23}_{-31}
12/17/13	HIP 29997	06:18:50.776[T]	+69:19:11.231[T]	18.64±0.23[T]	53.648 ±0.662	4.757±0.009	4.672 ±0.017	A0	324^{+33}_{-44}
12/17/13	HIP 24305	05:12:55.902	-16:12:19.668	19.1775±0.3265	52.144 ±0.888	3.29±0.002[N]	3.57 ±0.017	B9[D]	57^{+54}_{-31}
12/17/13	HIP 43970	08:57:14.949	+15:19:21.959	20.3294±0.0891	49.19 ±0.216	5.22±0.01	4.865 ±0.016	A5	450^{+132}_{-112}
12/17/13	HIP 22361	04:48:50.353	+75:56:28.391	21.0142±0.0265	47.587 ±0.06	5.952±0.009	5.221 ±0.016	A9	747^{+245}_{-208}
12/17/13	HIP 53824	11:00:44.802	+06:06:05.202	21.4498±0.0911	46.62 ±0.198	4.977±0.009	4.614 ±0.016	A5	564^{+99}_{-69}
12/17/13	HIP 5542	01:11:06.162[T]	+55:08:59.647[T]	24.42±0.24[T]	40.95 ±0.402	4.33±0.009[N]	3.99 ±0.017[N]	A7	458^{+80}_{-17}
12/17/13	HIP 4436	00:56:45.212	+38:29:57.638	25.14±0.86	39.777 ±1.361	3.87±0.002[N]	3.49 ±0.023[N]	A6[H]	451^{+21}_{-18}
12/17/13	HIP 51658	10:33:13.889	+40:25:31.966	29.1453±0.1407	34.311 ±0.166	4.715±0.009	4.197 ±0.026	A7	697^{+138}_{-124}
12/17/13	HIP 116928	23:42:02.806[T]	+01:46:48.148[T]	30.59±0.19[T]	32.69 ±0.203	4.51±0.003[N]	4.064 ±0.036	A7[P]	477^{+11}_{-12}
12/17/13	HIP 8903	01:54:38.410[T]	+20:48:28.913[T]	55.6±0.58[T]	17.986 ±0.188	2.65±0.002[N]	2.38 ±0.016[N]	A5[P]	557^{+25}_{-37}

[A]Hube (1970), [B]Houk (1982), [C]Loden (1983), [D]Houk and Smith-Moore (1988), [E]Oja (1991), [F]Oja (1993), [G]Cannon and Pickering (1993), [H]Abt and Morrell (1995), [I]tyc (1997), [J]Houk and Swift (1999), [K]Wenger *et al.* (2000), [L]Høg *et al.* (2000), [M]Paunzen *et al.* (2001), [N]Ducati (2002), [O]Cutri *et al.* (2003b), [P]Gray *et al.* (2003), [Q]Gray *et al.* (2006), [R]Levenhagen and Leister (2006), [S]Royer *et al.* (2007), [T]van Leeuwen (2007), [U]van Belle and von Braun (2009), [V]Zorec *et al.* (2009),

[W] Chesneau *et al.* (2010), [X] Nielsen *et al.* (2013), [Y] Arcos *et al.* (2018), [Z] Gaia Collaboration (2020)

APPENDIX B

COMPANION PROPERTIES FOR 91 CANDIDATES FOUND FROM THE NIGHT OF 04 JUNE 2014

Table B.1: Candidate Companion Properties from 04 June 2014

Star	Separation(arcsec)	Distance to Star (pc)	Projected Separation (AU)	Δ Magnitude	M_K	Mass (M_{jup})
HIP90762	3.4 ± 0.04	125.16±0.99	426.05 ± 6.17	11.98 ± 0.04	11.97 ± 0.06	39^{+1}_{-4}
HIP101421	7.53 ± 0.03	101.32±2.16	762.57 ± 16.6	12.85 ± 0.04	12.21 ± 0.1	$13^{+1}_{-0.4}$
HIP101716	2.53 ± 0.08	91.83±0.42	232.7 ± 7.15	13.43 ± 0.08	14.33 ± 0.09	$12^{+1}_{-0.4}$
HIP101716	3.18 ± 0.08	91.83±0.42	291.53 ± 7.62	13.52 ± 0.08	14.42 ± 0.09	12^{+1}_{-1}
HIP101716	5.85 ± 0.05	91.83±0.42	536.9 ± 4.89	13.32 ± 0.06	14.21 ± 0.07	12^{+1}_{-1}
HIP104105	3.25 ± 0.08	140.06±1.14	454.8 ± 12.16	13.29 ± 0.05	13.64 ± 0.08	15^{+1}_{-1}
HIP104105	2.3 ± 0.06	140.06±1.14	322.49 ± 9.05	10.04 ± 0.05	10.39 ± 0.07	45^{+5}_{-4}
HIP105282	5.39 ± 0.05	168.63±1.69	908.63 ± 12.1	10.53 ± 0.04	10.47 ± 0.06	28^{+4}_{-9}
HIP105282	5.04 ± 0.09	168.63±1.69	850.04 ± 17.07	13.6 ± 0.06	13.54 ± 0.09	$11^{+0.4}_{-1}$
HIP105282	3.39 ± 0.04	168.63±1.69	572.01 ± 9.44	12.05 ± 0.04	11.99 ± 0.06	$14^{+0.1}_{-2}$
HIP105282	4.21 ± 0.05	168.63±1.69	710.38 ± 11.21	12.75 ± 0.04	12.69 ± 0.07	$12^{+0.3}_{-0.5}$
HIP105282	5.1 ± 0.12	168.63±1.69	860.62 ± 21.73	14.57 ± 0.08	14.51 ± 0.1	9^{+1}_{-1}
HIP105282	3.53 ± 0.04	168.63±1.69	595.13 ± 9.62	8.94 ± 0.04	8.88 ± 0.06	67^{+7}_{-8}
HIP105282	4.05 ± 0.04	168.63±1.69	682.31 ± 9.56	10.17 ± 0.04	10.11 ± 0.06	34^{+4}_{-6}
HIP105282	3.45 ± 0.07	168.63±1.69	582.53 ± 12.89	13.35 ± 0.06	13.29 ± 0.08	$11^{+0.4}_{-0.5}$
HIP105282	3.24 ± 0.06	168.63±1.69	545.83 ± 11.01	12.29 ± 0.04	12.23 ± 0.07	$13^{+1}_{-0.4}$
HIP105282	3.96 ± 0.06	168.63±1.69	667.1 ± 11.59	13.06 ± 0.04	13.0 ± 0.07	$12^{+0.3}_{-0}$
HIP105282	5.49 ± 0.07	168.63±1.69	926.0 ± 15.4	13.66 ± 0.05	13.6 ± 0.07	$11^{+0.4}_{-1}$
HIP105282	5.46 ± 0.05	168.63±1.69	921.56 ± 12.06	7.34 ± 0.04	7.29 ± 0.06	160^{+11}_{-13}
HIP109521	3.09 ± 0.05	56.08±0.21	173.26 ± 2.91	12.0 ± 0.04	13.22 ± 0.05	37^{+2}_{-5}
HIP109521	5.74 ± 0.05	56.08±0.21	321.7 ± 3.28	14.49 ± 0.04	15.7 ± 0.05	20^{+1}_{-3}
HIP109521	5.69 ± 0.05	56.08±0.21	319.26 ± 2.91	13.73 ± 0.04	14.94 ± 0.05	24^{+2}_{-4}
HIP61558	5.84 ± 0.18	71.43±0.24	417.28 ± 12.76	15.3 ± 0.1	16.73 ± 0.11	11^{+1}_{-2}
HIP81560	4.35 ± 0.05	93.98±0.18	409.0 ± 4.34	10.49 ± 0.04	12.44 ± 0.05	30^{+13}_{-12}
HIP81634	1.1 ± 0.06	99.8±0.27	109.24 ± 6.29	7.88 ± 0.05	9.54 ± 6.67	86^{+251}_{-78}
HIP81634	4.37 ± 0.06	99.8±0.27	435.82 ± 5.85	12.51 ± 0.05	14.17 ± 6.67	19^{+154}_{-15}
HIP82402	5.12 ± 0.05	59.1±0.21	302.75 ± 3.09	10.57 ± 0.04	11.94 ± 0.06	41^{+8}_{-9}
HIP84880	4.41 ± 0.05	62.3±1.01	274.54 ± 5.4	17.3 ± 0.04	17.51 ± 0.08	10^{+1}_{-9}
HIP86565	3.53 ± 0.07	53.11±0.71	187.24 ± 4.42	13.84 ± 0.05	14.32 ± 0.28	21^{+2}_{-2}
HIP86565	5.17 ± 0.05	53.11±0.71	274.58 ± 4.41	13.68 ± 0.05	14.16 ± 0.28	22^{+2}_{-3}
HIP86565	5.9 ± 0.04	53.11±0.71	313.44 ± 4.61	13.83 ± 0.03	14.32 ± 0.28	21^{+2}_{-3}
HIP86565	6.28 ± 0.07	53.11±0.71	333.58 ± 5.68	13.84 ± 0.05	14.32 ± 0.28	21^{+2}_{-2}
HIP87813	5.0 ± 0.04	80.78±0.6	404.22 ± 4.37	10.9 ± 0.04	12.06 ± 0.06	29^{+6}_{-5}
HIP87813	4.62 ± 0.05	80.78±0.6	373.03 ± 4.84	11.3 ± 0.04	12.47 ± 0.06	26^{+5}_{-6}
HIP87813	5.78 ± 0.05	80.78±0.6	466.56 ± 5.44	12.23 ± 0.04	13.39 ± 0.06	19^{+5}_{-4}

Continued on next page

Table B.1 – *Continued from previous page*

Star	Separation(arcsec)	Distance to Star (pc)	Projected Separation (AU)	Δ Magnitude	M_K	Mass (M_{jup})
HIP87813	5.3 ± 0.06	80.78±0.6	428.07 ± 5.48	10.67 ± 0.05	11.84 ± 0.07	30^{+7}_{-5}
HIP87813	4.32 ± 0.04	80.78±0.6	348.95 ± 4.22	12.08 ± 0.04	13.24 ± 0.06	20^{+5}_{-5}
HIP87813	5.17 ± 0.04	80.78±0.6	417.84 ± 4.68	11.6 ± 0.04	12.77 ± 0.06	23^{+5}_{-8}
HIP87813	2.22 ± 0.13	80.78±0.6	179.49 ± 10.43	7.46 ± 0.07	8.62 ± 0.09	117^{+11}_{-16}
HIP87813	2.92 ± 0.04	80.78±0.6	236.22 ± 3.89	9.25 ± 0.04	10.41 ± 0.07	50^{+10}_{-10}
HIP87813	3.66 ± 0.04	80.78±0.6	295.87 ± 4.1	10.91 ± 0.04	12.07 ± 0.06	29^{+6}_{-5}
HIP87813	4.63 ± 0.04	80.78±0.6	374.22 ± 4.51	12.24 ± 0.04	13.4 ± 0.06	19^{+5}_{-4}
HIP90806	3.93 ± 0.04	65.4±0.35	256.84 ± 3.08	7.75 ± 0.38	8.74 ± 0.39	122^{+17}_{-20}
HIP90806	4.83 ± 0.04	65.4±0.35	315.82 ± 3.0	10.31 ± 0.38	11.3 ± 0.39	47^{+8}_{-8}
HIP90806	6.71 ± 0.05	65.4±0.35	439.13 ± 4.12	11.23 ± 0.38	12.22 ± 0.39	36^{+6}_{-6}
HIP90806	3.18 ± 0.06	65.4±0.35	208.13 ± 4.35	11.98 ± 0.38	12.97 ± 0.4	29^{+5}_{-4}
HIP90806	2.62 ± 0.07	65.4±0.35	171.22 ± 4.84	12.31 ± 0.38	13.3 ± 0.4	26^{+4}_{-4}
HIP90806	3.78 ± 0.08	65.4±0.35	247.03 ± 5.11	12.76 ± 0.38	13.75 ± 0.4	23^{+4}_{-4}
HIP90806	3.54 ± 0.06	65.4±0.35	231.44 ± 4.2	12.89 ± 0.38	13.88 ± 0.39	23^{+4}_{-4}
HIP90806	6.59 ± 0.04	65.4±0.35	430.87 ± 3.48	12.74 ± 0.38	13.73 ± 0.39	24^{+4}_{-4}
HIP90806	6.48 ± 0.05	65.4±0.35	423.73 ± 4.0	12.29 ± 0.38	13.28 ± 0.39	27^{+4}_{-4}
HIP90806	5.42 ± 0.05	65.4±0.35	354.6 ± 3.95	13.02 ± 0.38	14.0 ± 0.39	22^{+4}_{-4}
HIP90806	4.55 ± 0.04	65.4±0.35	297.58 ± 3.25	12.66 ± 0.38	13.65 ± 0.39	24^{+4}_{-5}
HIP92041	4.96 ± 0.04	73.37±1.02	363.61 ± 5.93	16.93 ± 0.03	15.88 ± 0.34	7^{+1}_{-1}
HIP92041	4.89 ± 0.05	73.37±1.02	358.93 ± 6.22	18.08 ± 0.03	17.04 ± 0.34	$5^{+0.5}_{-0.5}$
HIP92041	4.19 ± 0.08	73.37±1.02	307.65 ± 7.12	18.08 ± 0.05	17.03 ± 0.35	$5^{+1}_{-0.5}$
HIP92312	5.64 ± 0.04	90.09±0.33	508.12 ± 4.18	12.94 ± 0.03	13.98 ± 0.05	21^{+2}_{-3}
HIP92312	5.98 ± 0.06	90.09±0.33	539.14 ± 5.45	13.76 ± 0.04	14.8 ± 0.05	16^{+2}_{-4}
HIP94833	2.76 ± 0.06	90.99±1.15	251.1 ± 6.24	12.58 ± 0.05	13.82 ± 0.08	16^{+5}_{-2}
HIP94833	3.1 ± 0.05	90.99±1.15	282.53 ± 5.63	13.01 ± 0.03	14.26 ± 0.07	12^{+6}_{-2}
HIP94833	4.3 ± 0.05	90.99±1.15	391.68 ± 6.85	11.71 ± 0.04	12.95 ± 0.07	23^{+4}_{-8}
HIP94833	3.6 ± 0.05	90.99±1.15	327.51 ± 6.11	11.32 ± 0.03	12.57 ± 0.07	26^{+4}_{-5}
HIP94833	2.0 ± 0.08	90.99±1.15	182.23 ± 7.34	11.63 ± 0.06	12.87 ± 0.09	23^{+4}_{-8}
HIP94833	2.27 ± 0.05	90.99±1.15	206.61 ± 5.57	10.95 ± 0.04	12.2 ± 0.07	28^{+5}_{-5}
HIP94833	5.49 ± 0.08	90.99±1.15	499.32 ± 9.8	13.16 ± 0.05	14.41 ± 0.08	12^{+5}_{-2}
HIP94833	6.34 ± 0.06	90.99±1.15	576.45 ± 9.31	12.96 ± 0.04	14.21 ± 0.08	12^{+6}_{-2}
HIP95951	5.25 ± 0.05	119.33±1.16	626.73 ± 8.19	13.68 ± 0.04	13.55 ± 0.06	12^{+2}_{-4}
HIP95951	3.61 ± 0.05	119.33±1.16	430.86 ± 6.84	13.17 ± 0.04	13.04 ± 0.06	$12^{+2}_{-0.4}$
HIP95951	2.86 ± 0.06	119.33±1.16	341.14 ± 8.18	13.81 ± 0.05	13.68 ± 0.07	$12^{+2}_{-0.4}$
HIP95951	3.63 ± 0.04	119.33±1.16	433.69 ± 6.19	11.84 ± 0.03	11.72 ± 0.06	25^{+2}_{-4}
HIP95951	3.55 ± 0.05	119.33±1.16	423.09 ± 6.89	12.48 ± 0.04	12.36 ± 0.06	19^{+2}_{-6}

Continued on next page

Table B.1 – *Continued from previous page*

Star	Separation(arcsec)	Distance to Star (pc)	Projected Separation (AU)	Δ Magnitude	M_K	Mass (M_{jup})
HIP95951	2.46 ± 0.06	119.33±1.16	293.52 ± 7.69	11.58 ± 0.04	11.46 ± 0.07	27^{+2}_{-3}
HIP95951	5.0 ± 0.05	119.33±1.16	597.12 ± 8.28	14.03 ± 0.04	13.91 ± 0.06	$11^{+2}_{-0.4}$
HIP95951	2.95 ± 0.09	119.33±1.16	352.4 ± 10.92	14.15 ± 0.07	14.02 ± 0.09	$11^{+2}_{-0.5}$
HIP97416	5.59 ± 0.04	95.69±0.21	534.85 ± 4.45	8.76 ± 0.04	10.43 ± 0.05	59^{+14}_{-16}
HIP97416	7.19 ± 0.05	95.69±0.21	688.4 ± 5.05	12.06 ± 0.05	13.74 ± 0.06	21^{+7}_{-7}
HIP97416	4.3 ± 0.05	95.69±0.21	411.81 ± 4.56	7.79 ± 0.04	9.47 ± 0.05	87^{+16}_{-20}
HIP97416	6.6 ± 0.04	95.69±0.21	631.97 ± 4.08	11.33 ± 0.04	13.0 ± 0.05	26^{+8}_{-10}
HIP97416	5.47 ± 0.05	95.69±0.21	523.69 ± 4.63	11.7 ± 0.05	13.38 ± 0.06	24^{+7}_{-8}
HIP97416	1.99 ± 0.08	95.69±0.21	190.08 ± 8.09	12.27 ± 0.08	13.94 ± 0.09	20^{+7}_{-6}
HIP97416	4.11 ± 0.07	95.69±0.21	393.23 ± 6.36	12.91 ± 0.06	14.58 ± 0.06	16^{+7}_{-3}
HIP97416	2.99 ± 0.05	95.69±0.21	286.18 ± 4.47	11.4 ± 0.05	13.07 ± 0.05	26^{+7}_{-10}
HIP97416	3.76 ± 0.05	95.69±0.21	360.01 ± 5.28	12.56 ± 0.05	14.24 ± 0.06	18^{+7}_{-5}
HIP97416	6.31 ± 0.07	95.69±0.21	603.88 ± 6.54	12.88 ± 0.06	14.56 ± 0.07	16^{+7}_{-3}
HIP97416	5.99 ± 0.07	95.69±0.21	573.45 ± 7.05	13.25 ± 0.06	14.92 ± 0.07	12^{+8}_{-1}
HIP97416	4.08 ± 0.06	95.69±0.21	390.3 ± 5.8	12.67 ± 0.05	14.34 ± 0.06	18^{+7}_{-4}
HIP97416	1.74 ± 0.19	95.69±0.21	166.37 ± 17.75	13.14 ± 0.15	14.82 ± 0.15	12^{+9}_{-1}
HIP97416	2.88 ± 0.08	95.69±0.21	275.74 ± 7.68	13.22 ± 0.07	19.79 ± 0.07	7^{+2}_{-2}
HIP97416	4.04 ± 0.09	95.69±0.21	387.03 ± 9.05	13.55 ± 0.07	15.22 ± 0.08	12^{+7}_{-1}
HIP98146	1.62 ± 0.15	106.61±0.31	173.04 ± 15.8	7.02 ± 0.09	8.36 ± 0.1	131^{+7}_{-11}
HIP98146	1.42 ± 0.08	106.61±0.31	151.67 ± 8.74	10.55 ± 0.06	11.89 ± 0.07	31^{+6}_{-3}

APPENDIX C

POST PYKLIP IMAGES AND CONTRAST CURVES FOR ALL 04 JUNE 2014 STARS

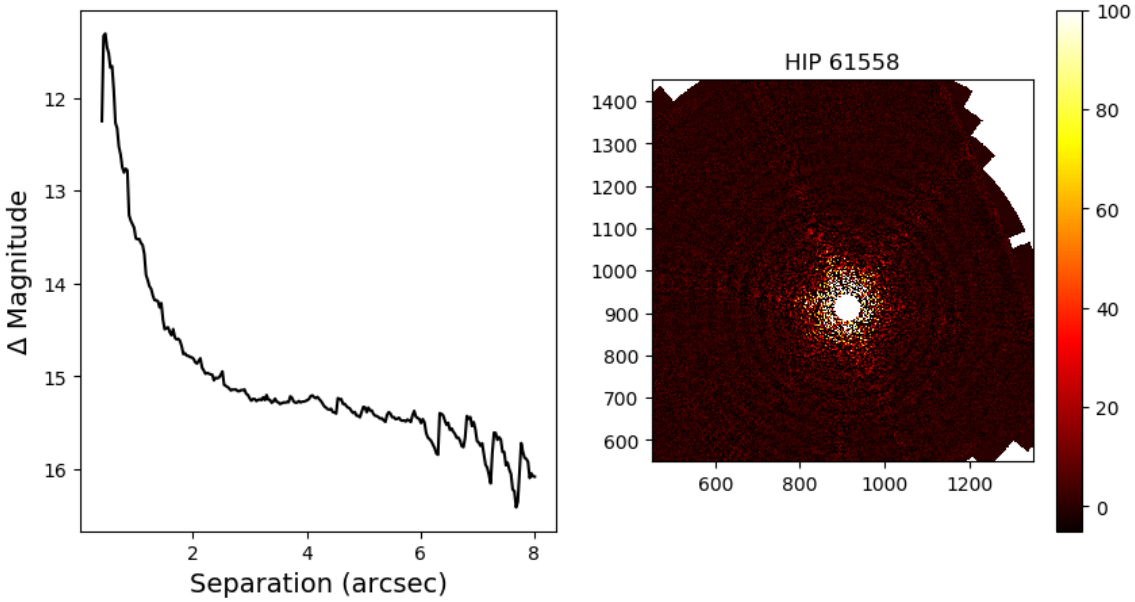
Δ Magnitude
Separation (arcsec)
HIP 61558

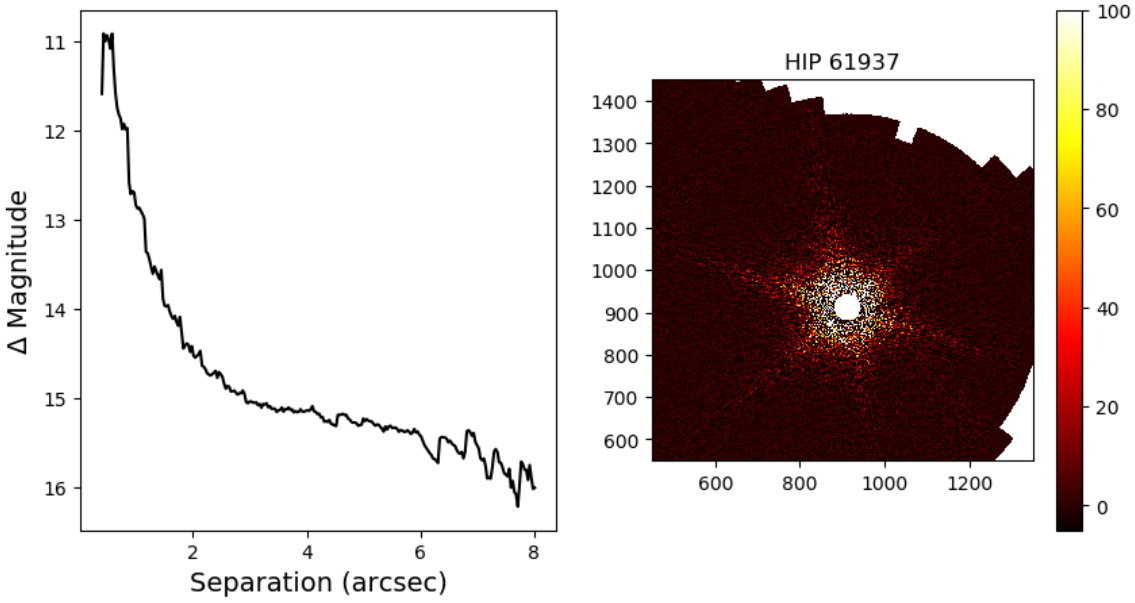
Δ Magnitude
Separation (arcsec)
HIP 61937

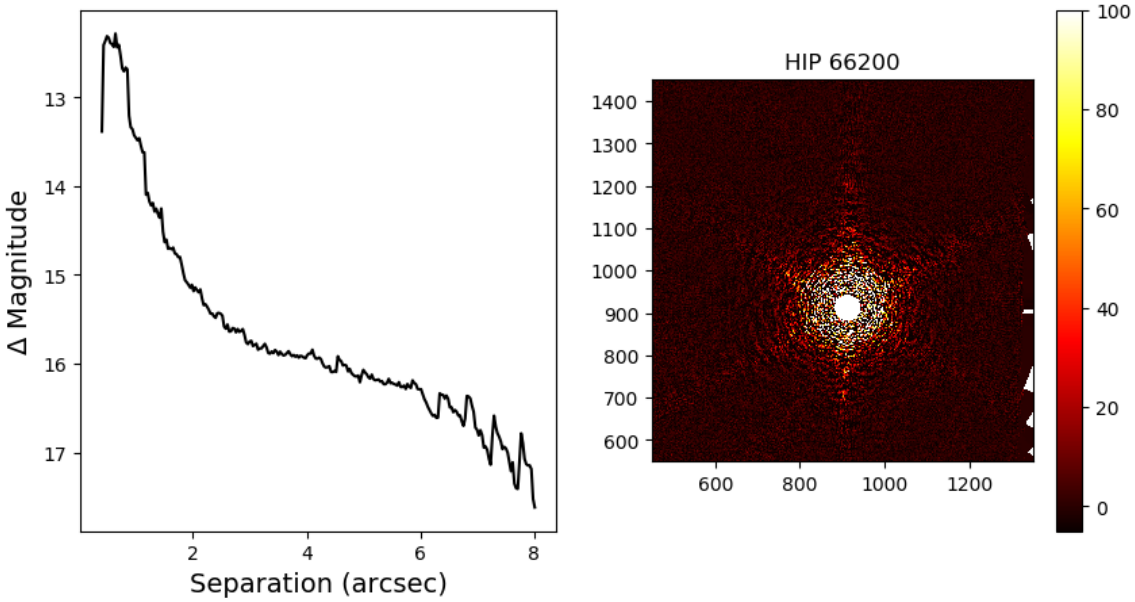
Δ Magnitude
Separation (arcsec)
HIP 66200

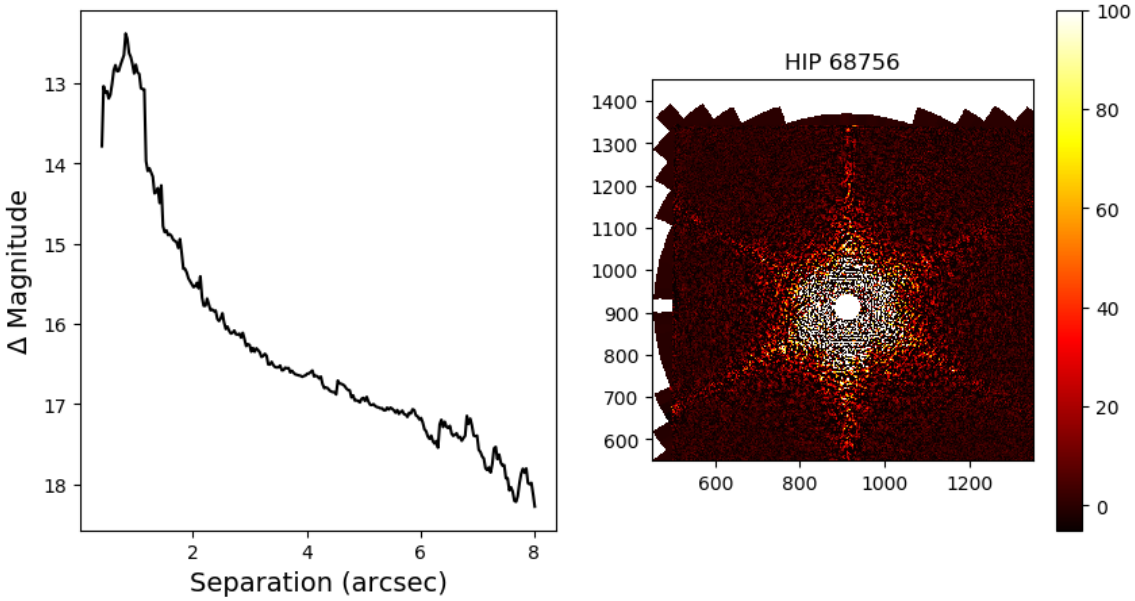
Δ Magnitude
Separation (arcsec)
HIP 68756

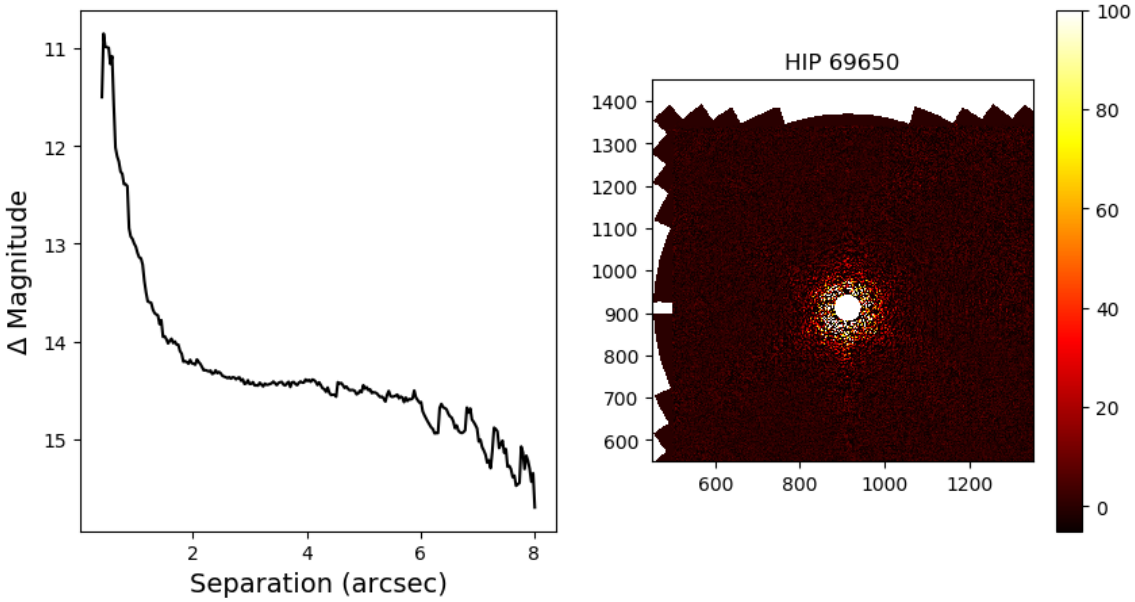
Δ Magnitude
Separation (arcsec)
HIP 69650

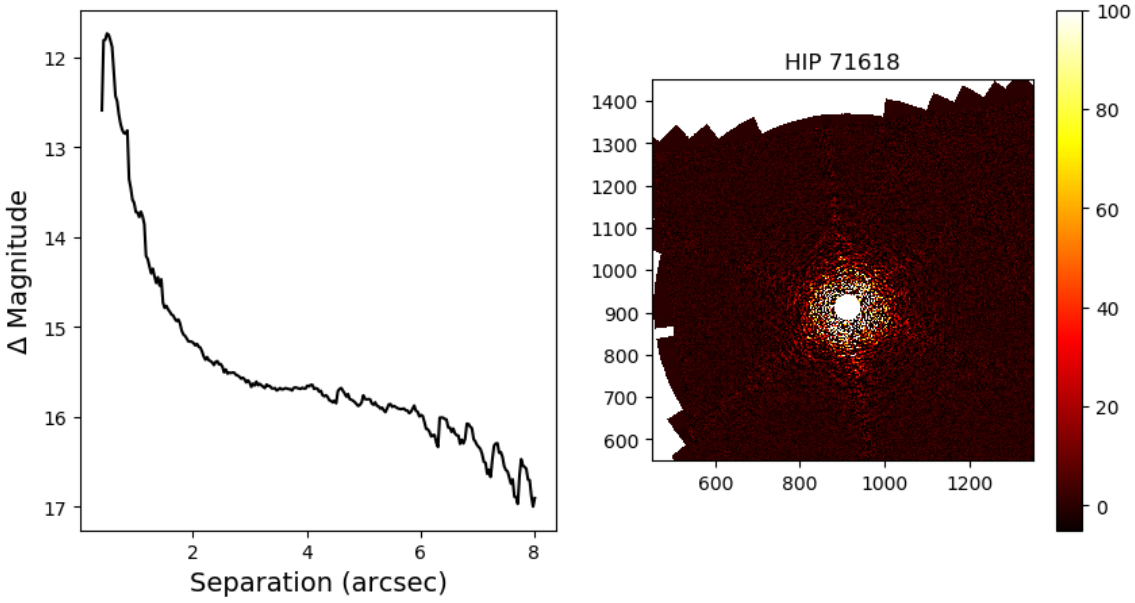
Δ Magnitude
Separation (arcsec)
HIP 71618

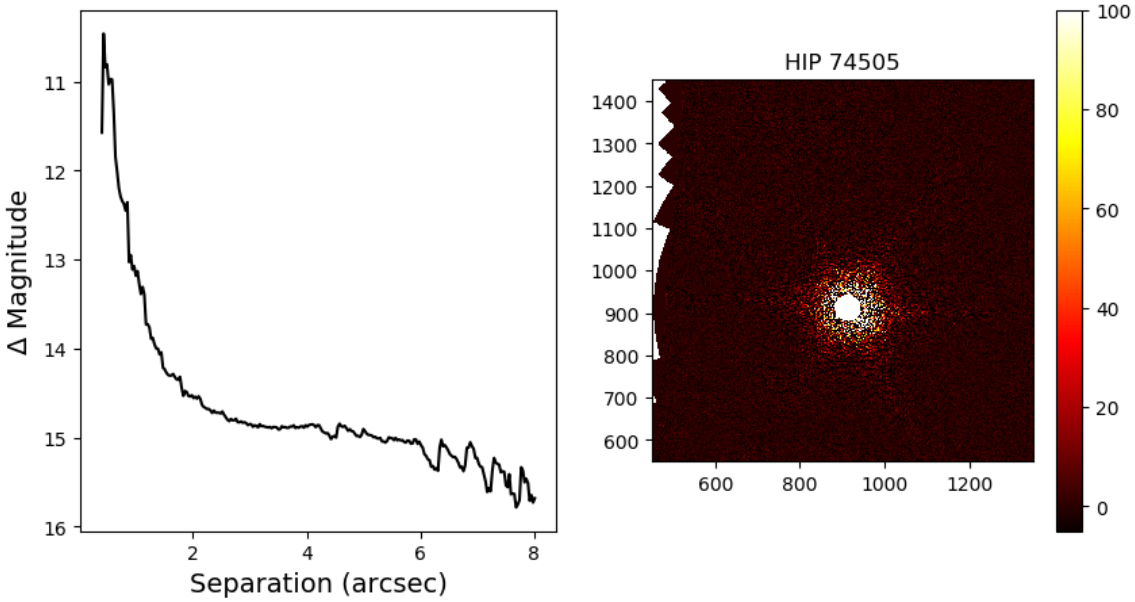
Δ Magnitude
Separation (arcsec)
HIP 74505

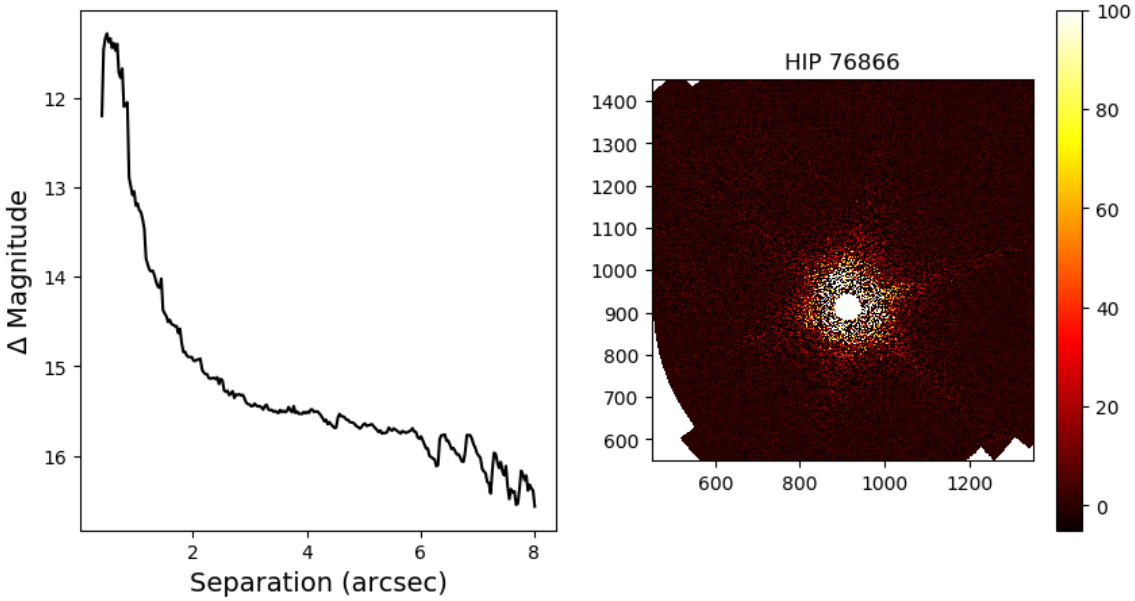
Δ Magnitude
Separation (arcsec)
HIP 76866

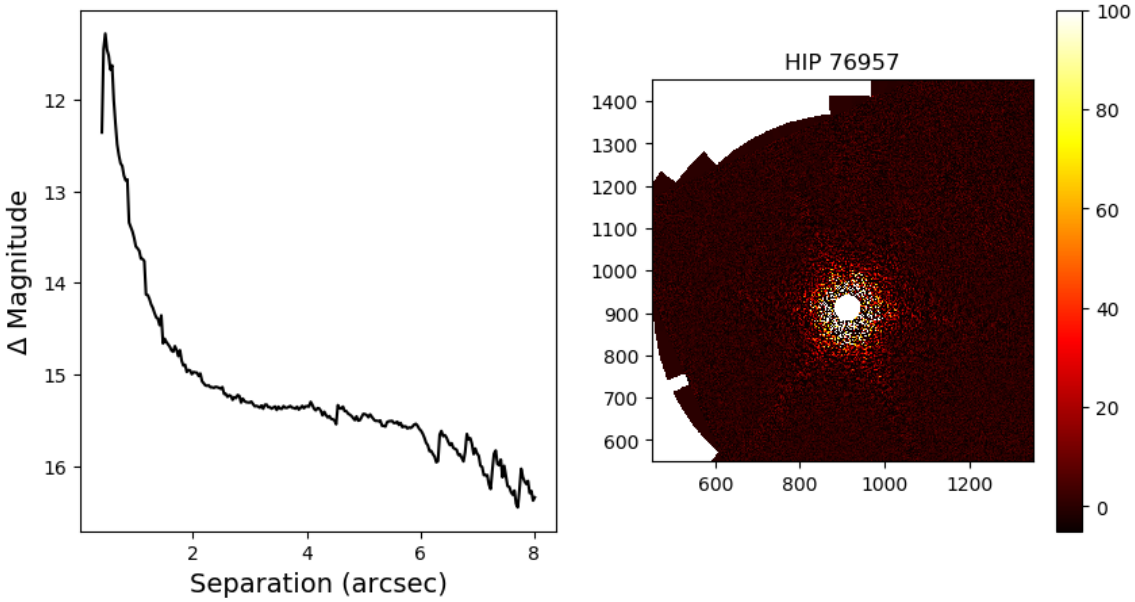
Δ Magnitude
Separation (arcsec)
HIP 76957

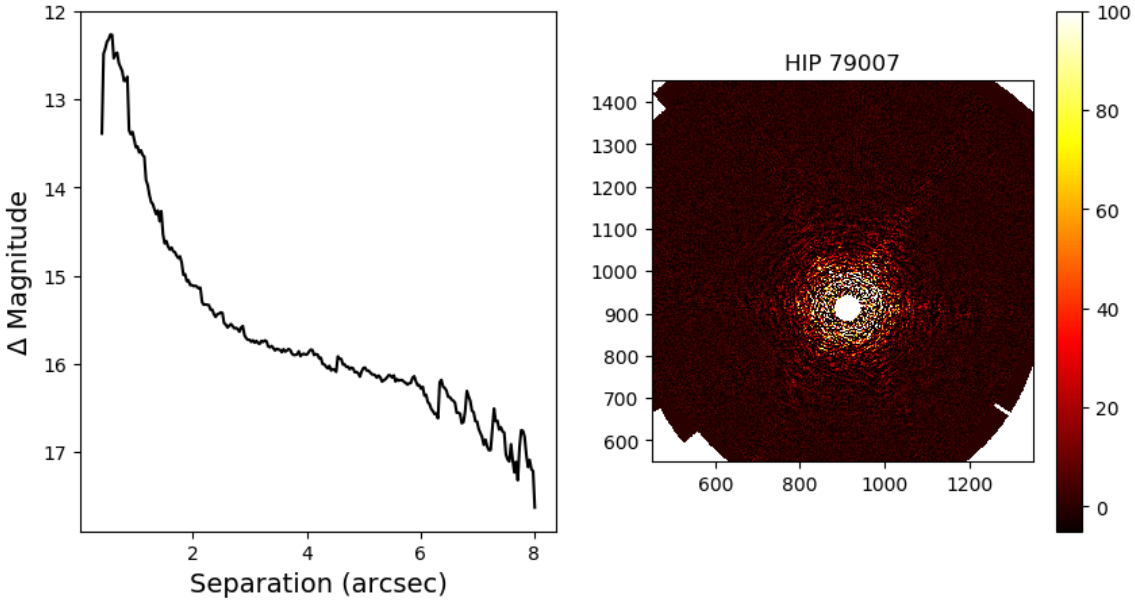
Δ Magnitude
Separation (arcsec)
HIP 79007

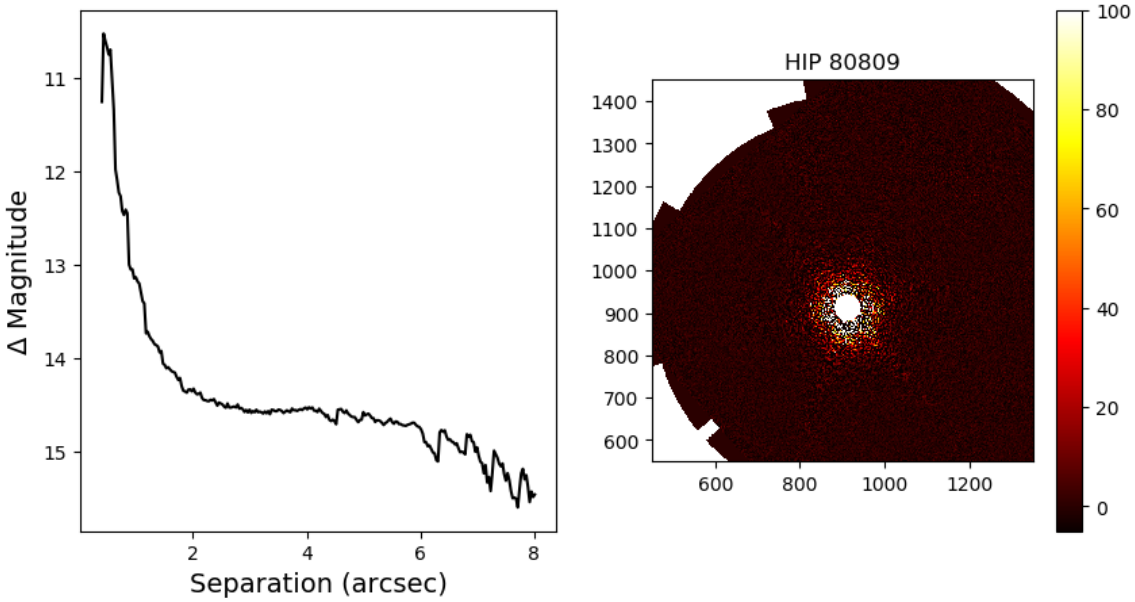
Δ Magnitude
Separation (arcsec)
HIP 80809

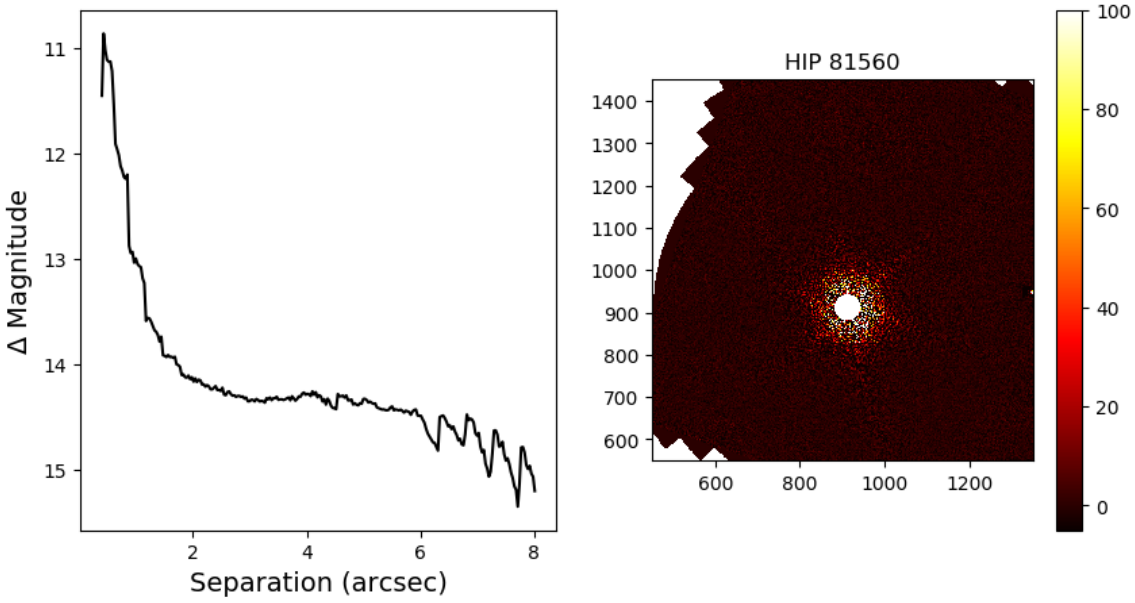
Δ Magnitude
Separation (arcsec)
HIP 81560

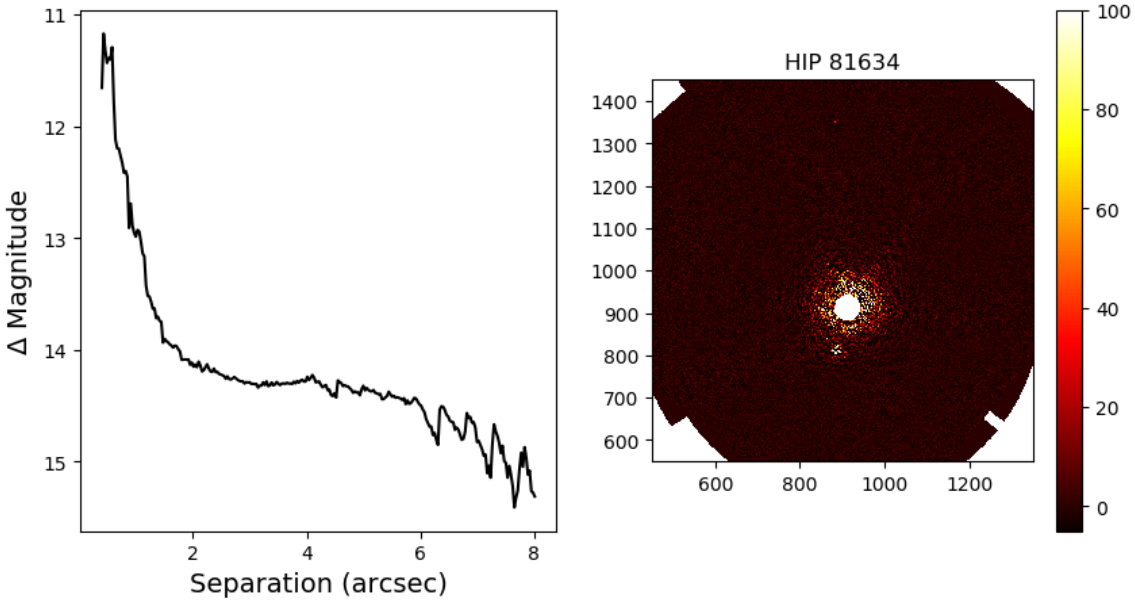
Δ Magnitude
Separation (arcsec)
HIP 81634

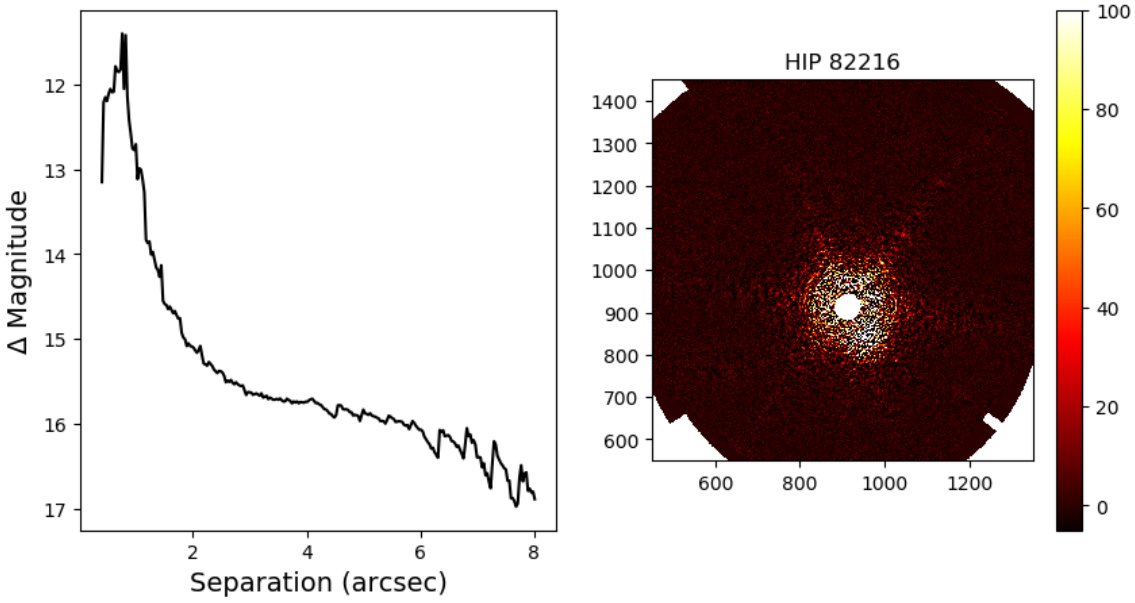
Δ Magnitude
Separation (arcsec)
HIP 82216

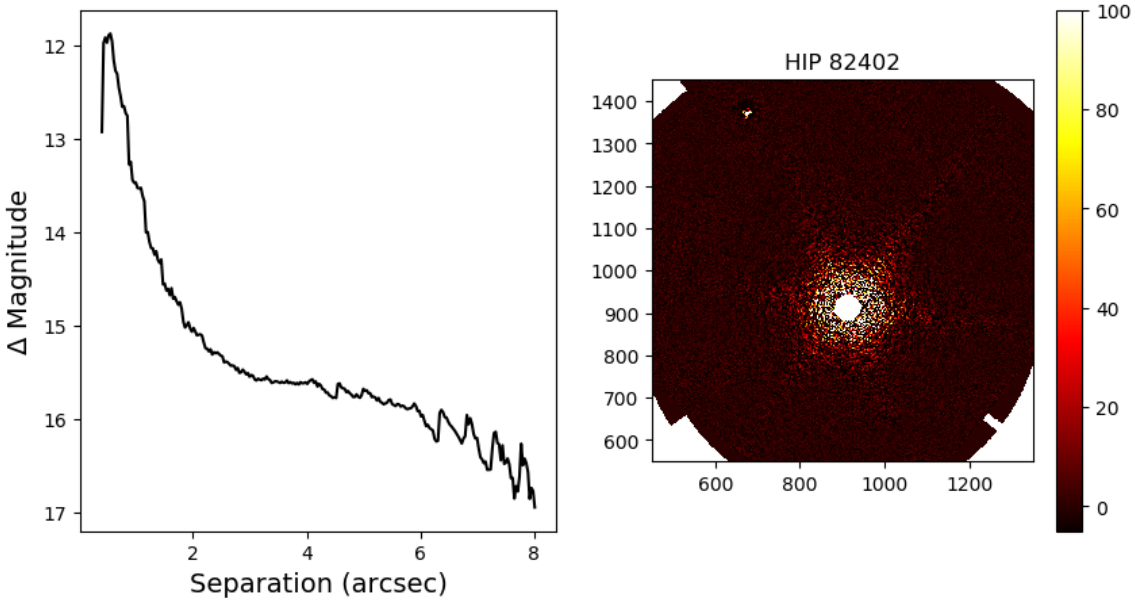
Δ Magnitude
Separation (arcsec)
HIP 82402

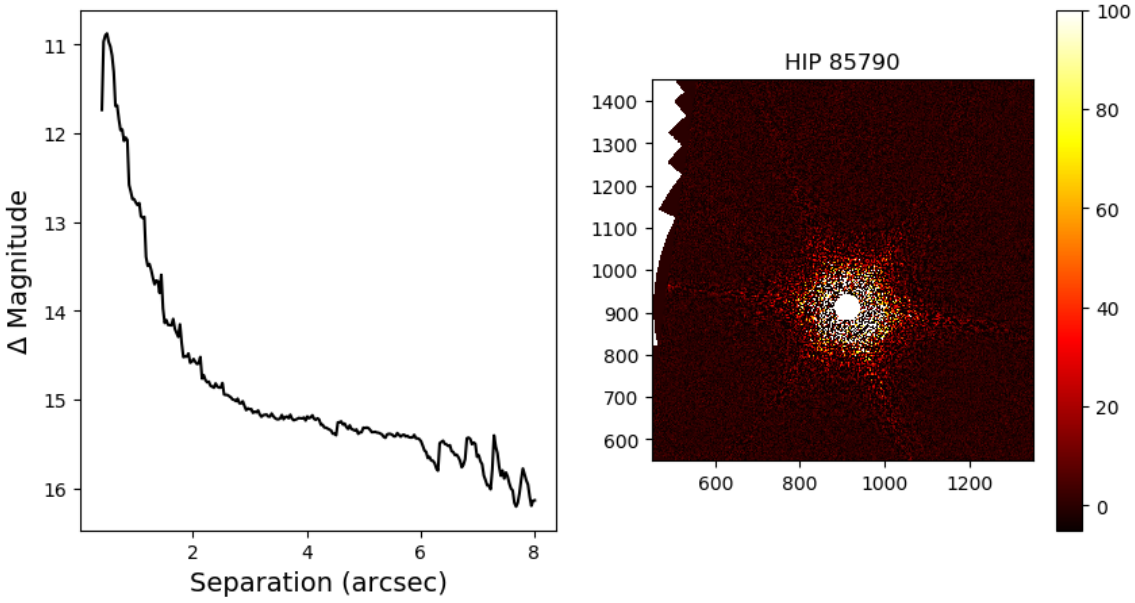
Δ Magnitude
Separation (arcsec)
HIP 85790

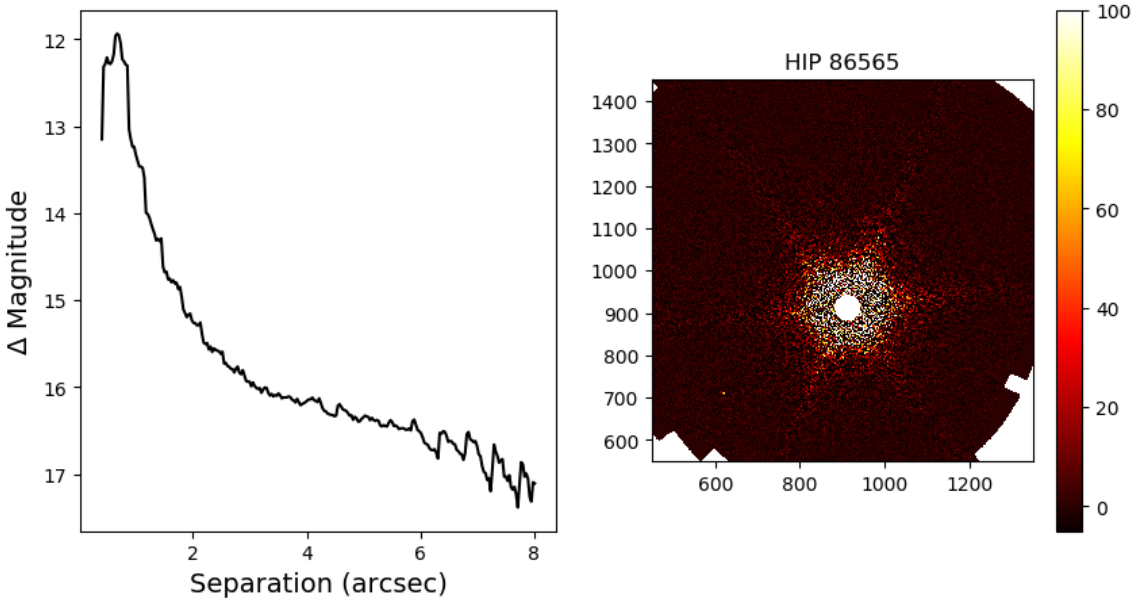
Δ Magnitude
Separation (arcsec)
HIP 86565

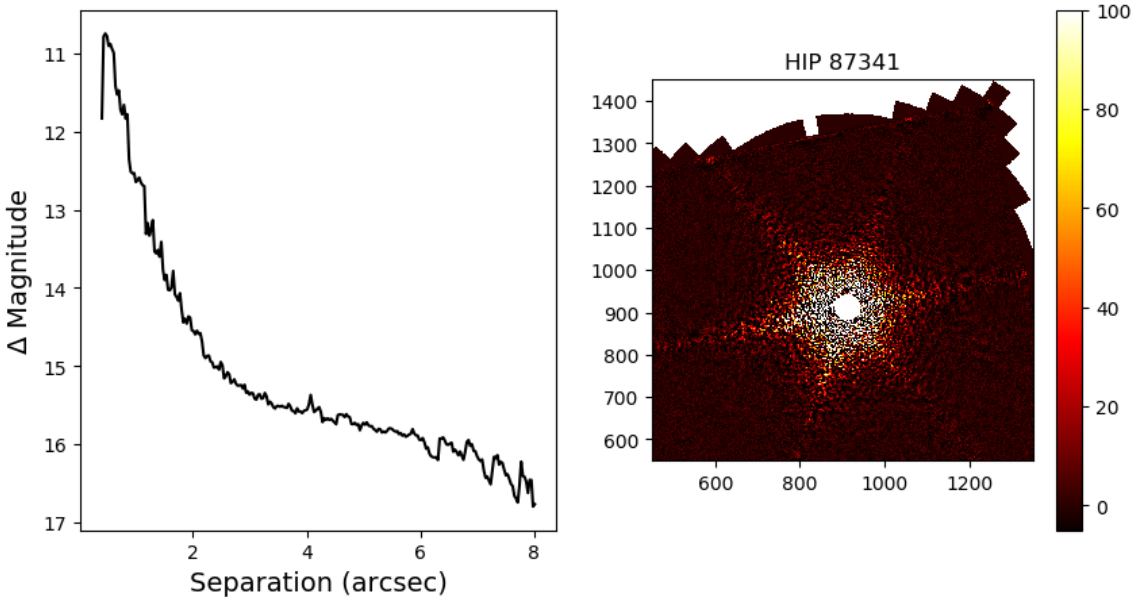
Δ Magnitude
Separation (arcsec)
HIP 87341

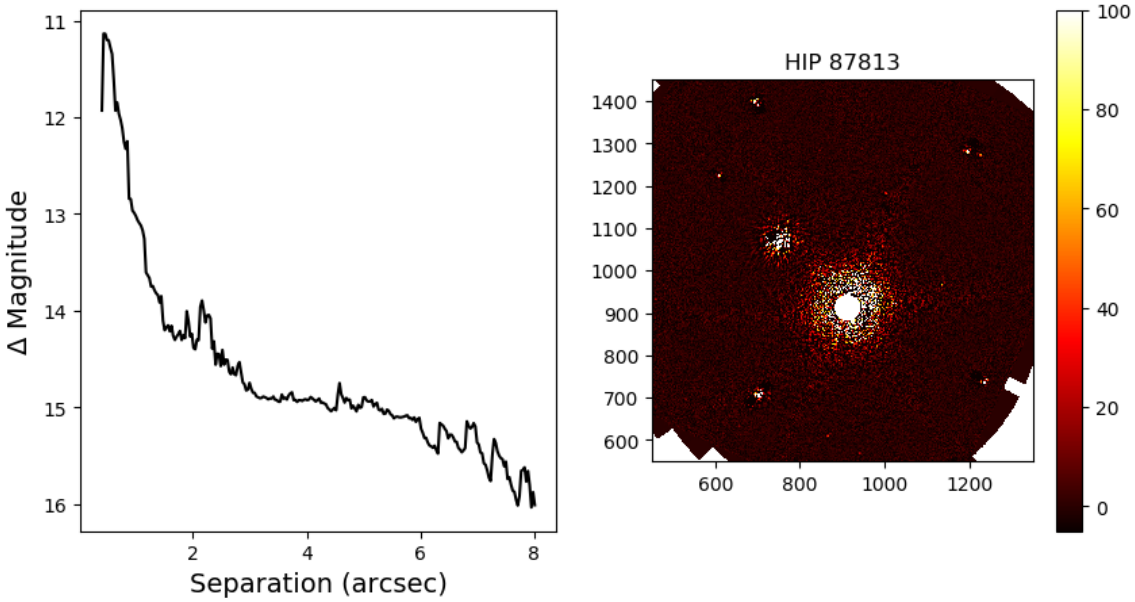
Δ Magnitude
Separation (arcsec)
HIP 87813

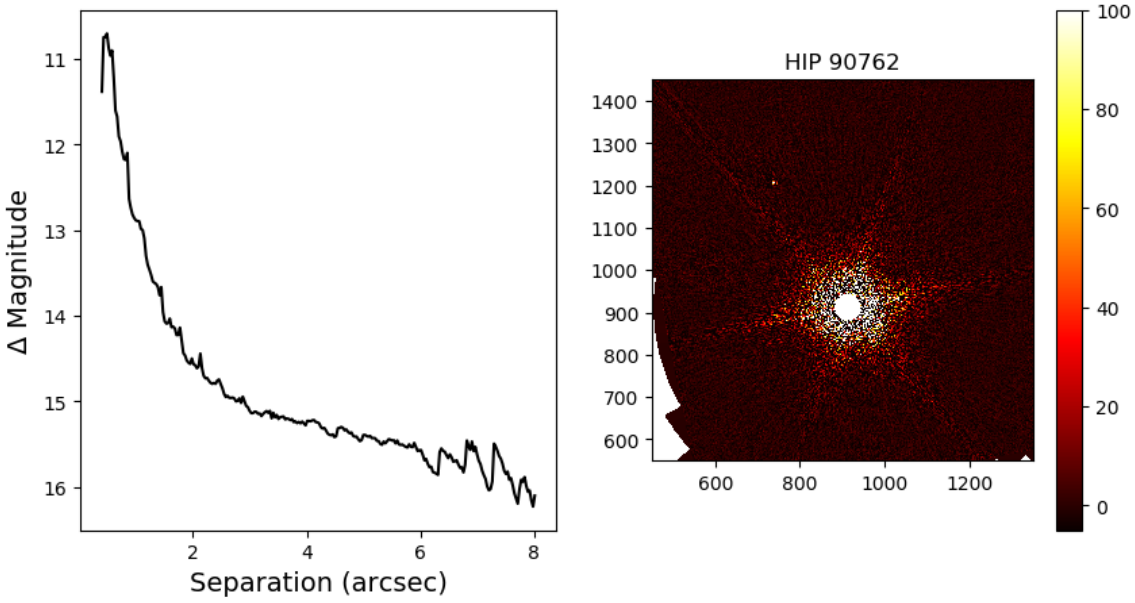
Δ Magnitude
Separation (arcsec)
HIP 90762

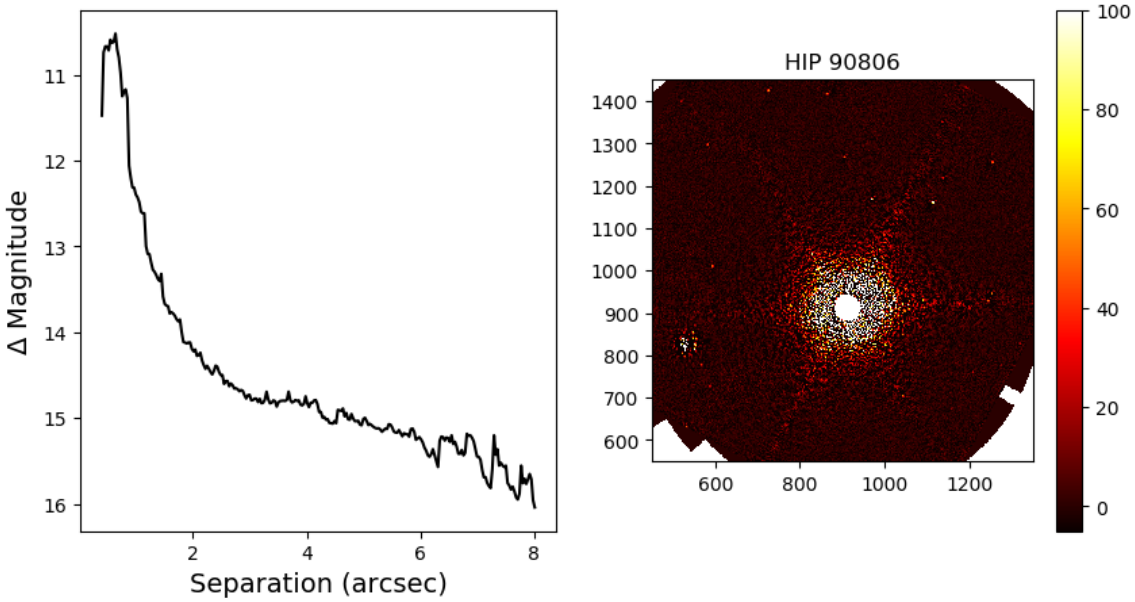
Δ Magnitude
Separation (arcsec)
HIP 90806

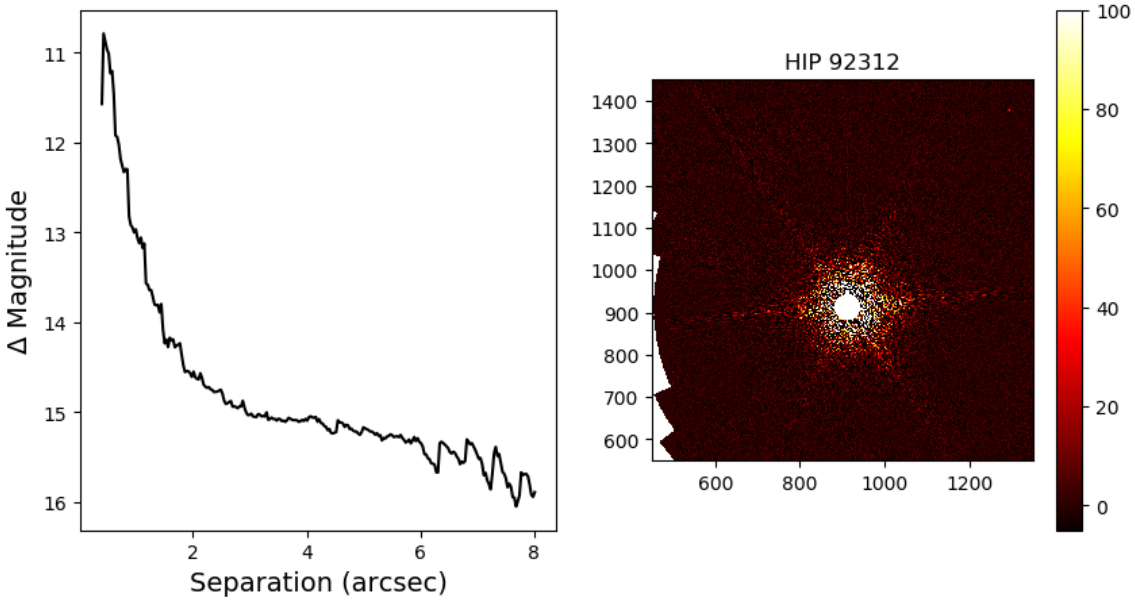
Δ Magnitude
Separation (arcsec)
HIP 92312

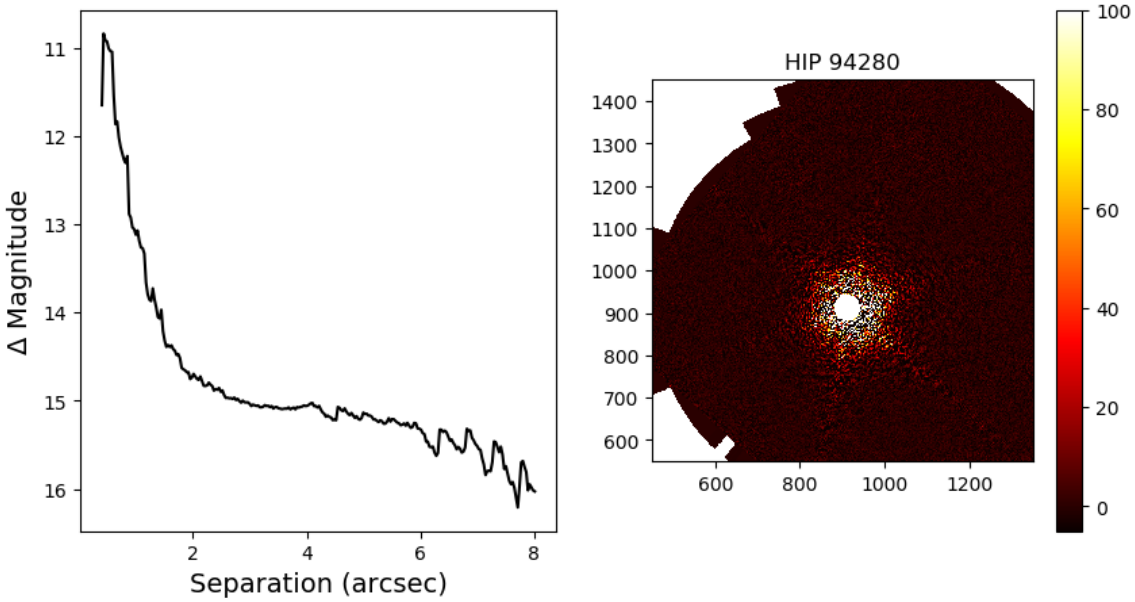
Δ Magnitude
Separation (arcsec)
HIP 94280

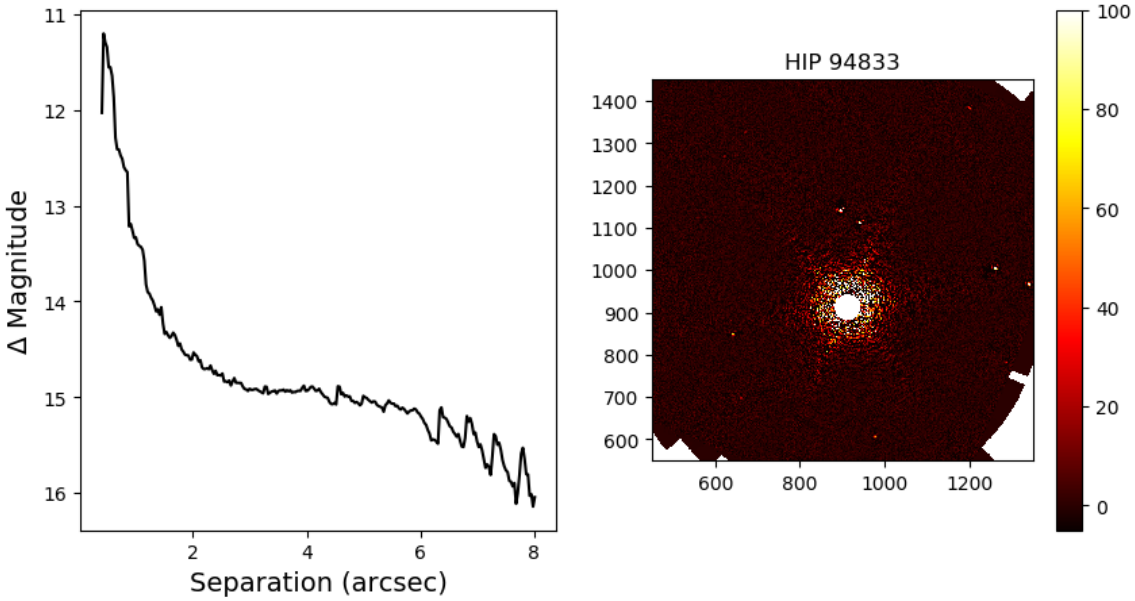
Δ Magnitude
Separation (arcsec)
HIP 94833

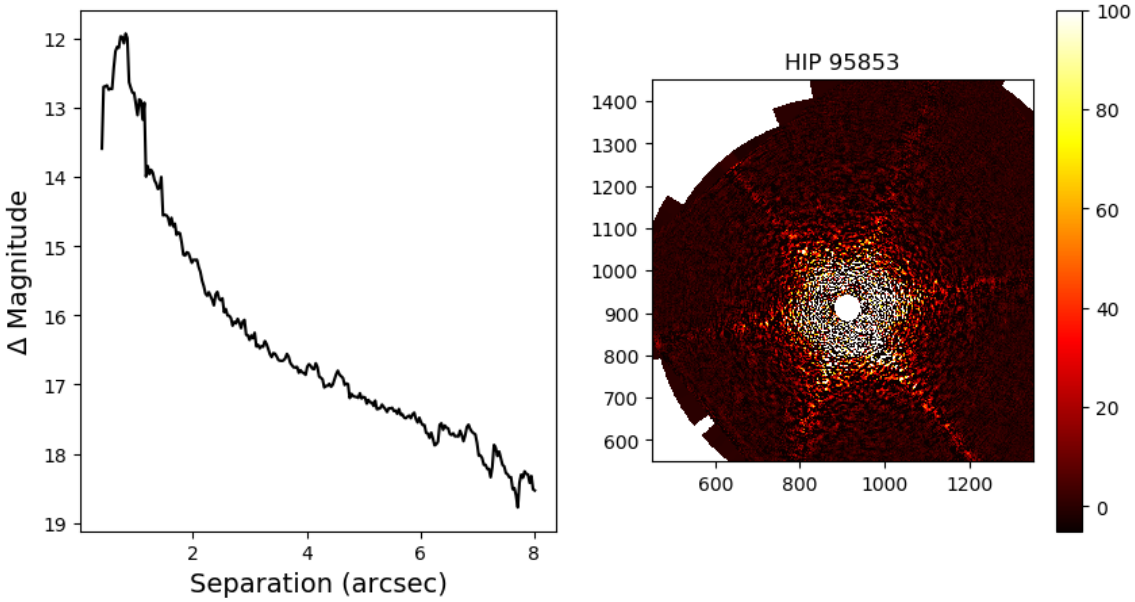
Δ Magnitude
Separation (arcsec)
HIP 95853

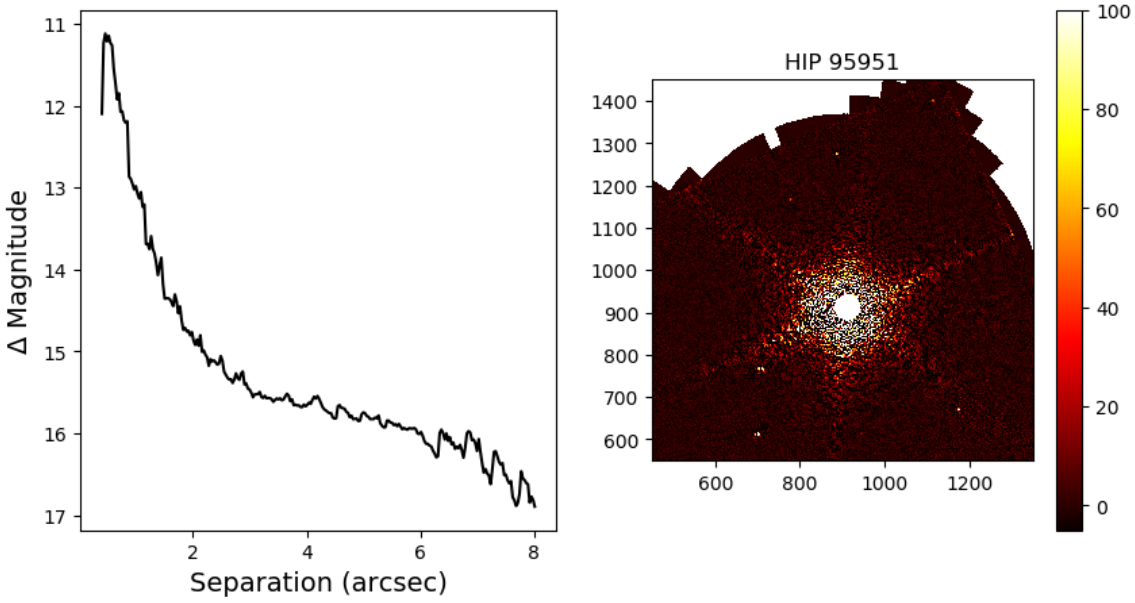
Δ Magnitude
Separation (arcsec)
HIP 95951

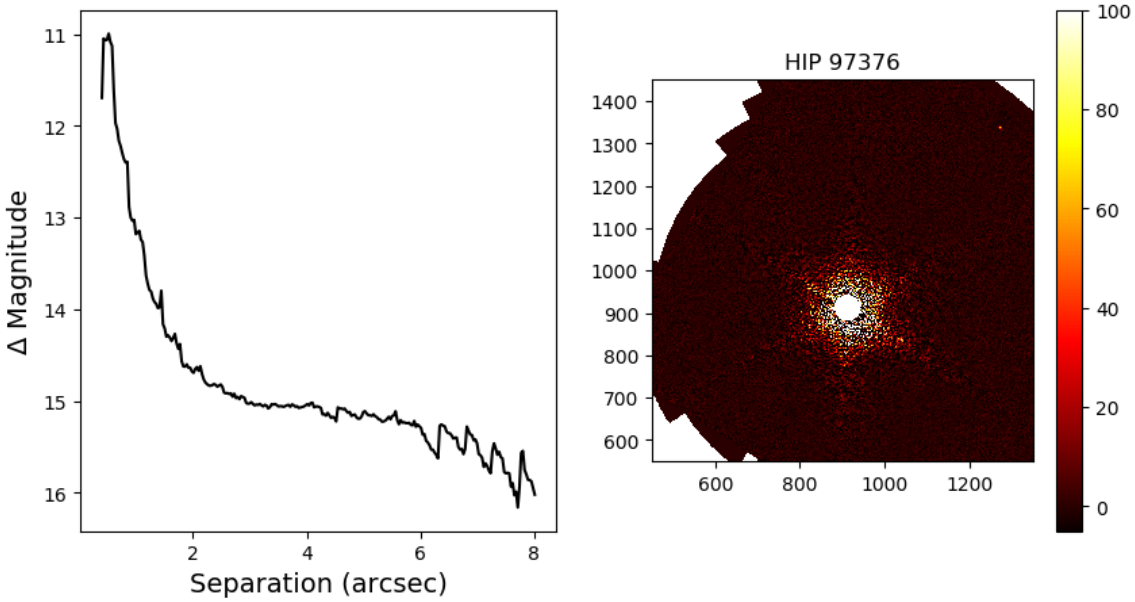
Δ Magnitude
Separation (arcsec)
HIP 97376

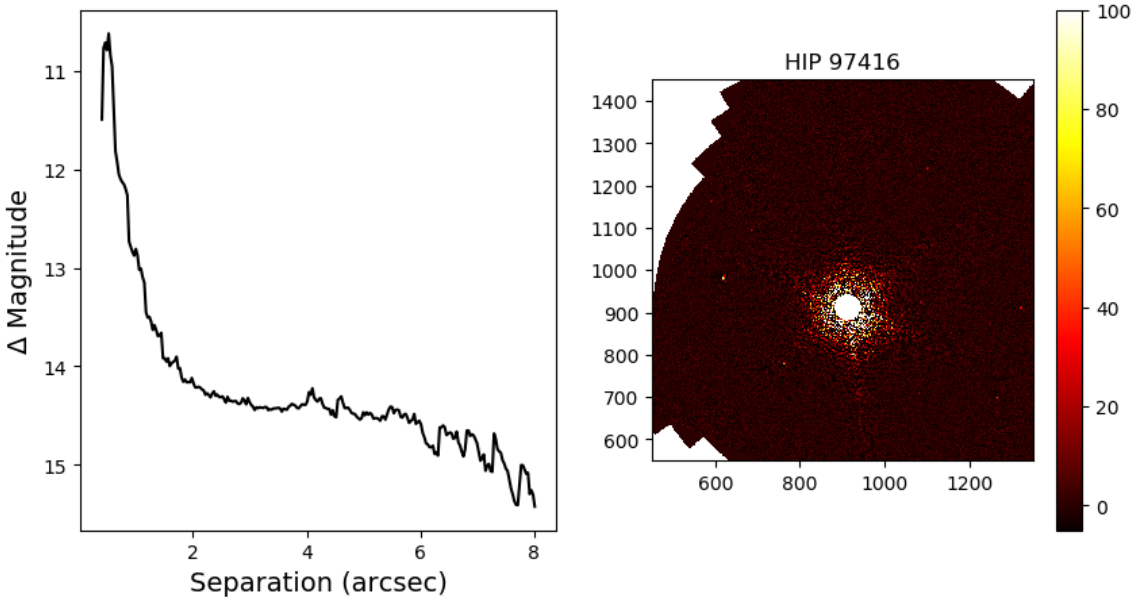
Δ Magnitude
Separation (arcsec)
HIP 97416

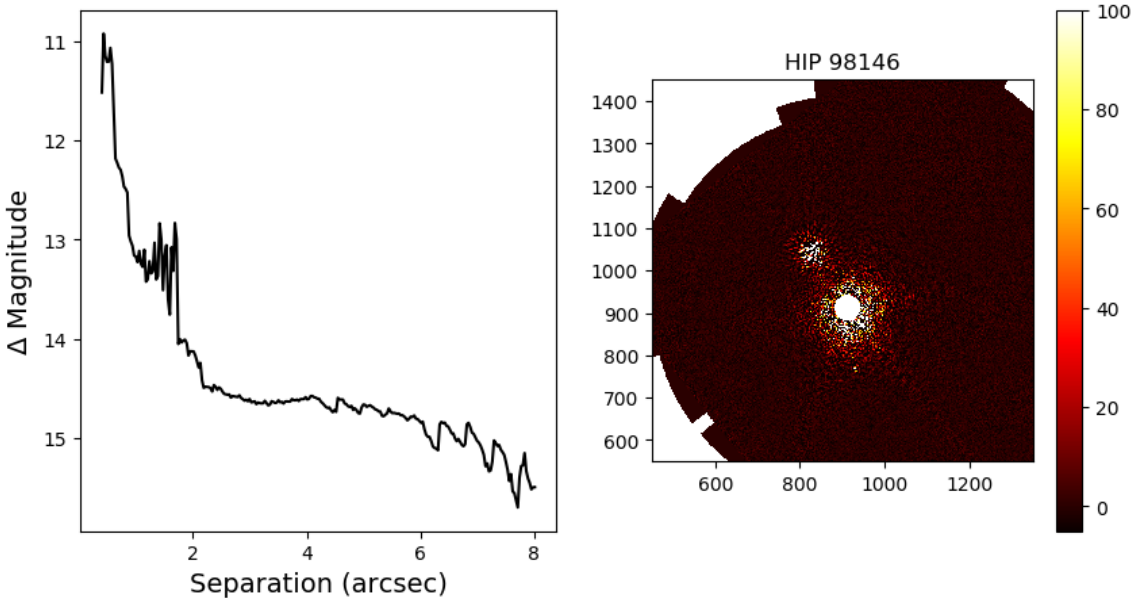
Δ Magnitude
Separation (arcsec)
HIP 98146

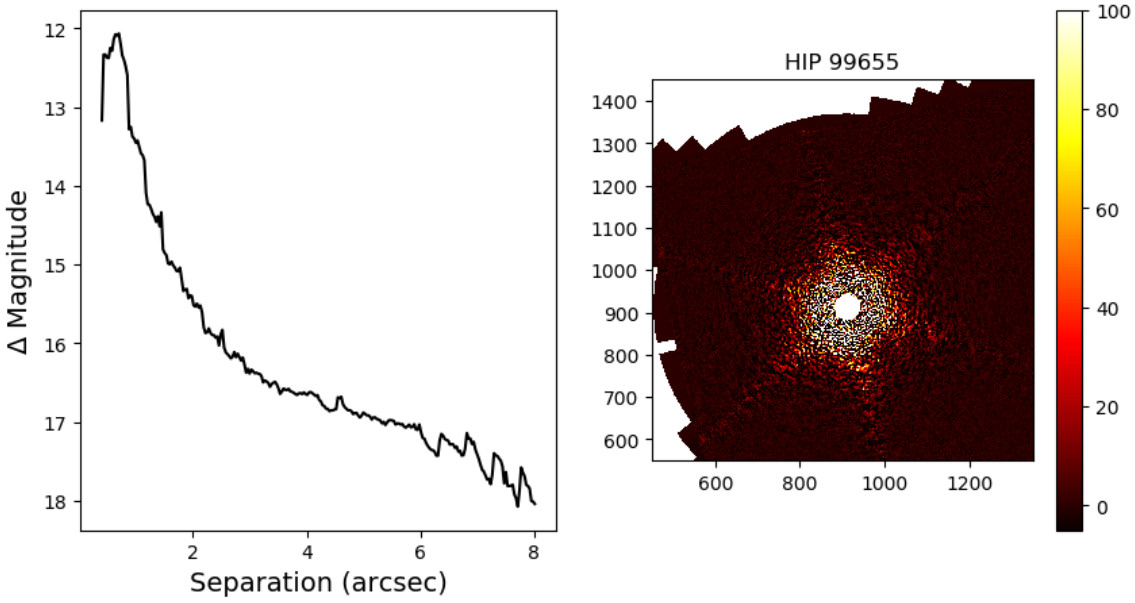
Δ Magnitude
Separation (arcsec)
HIP 99655

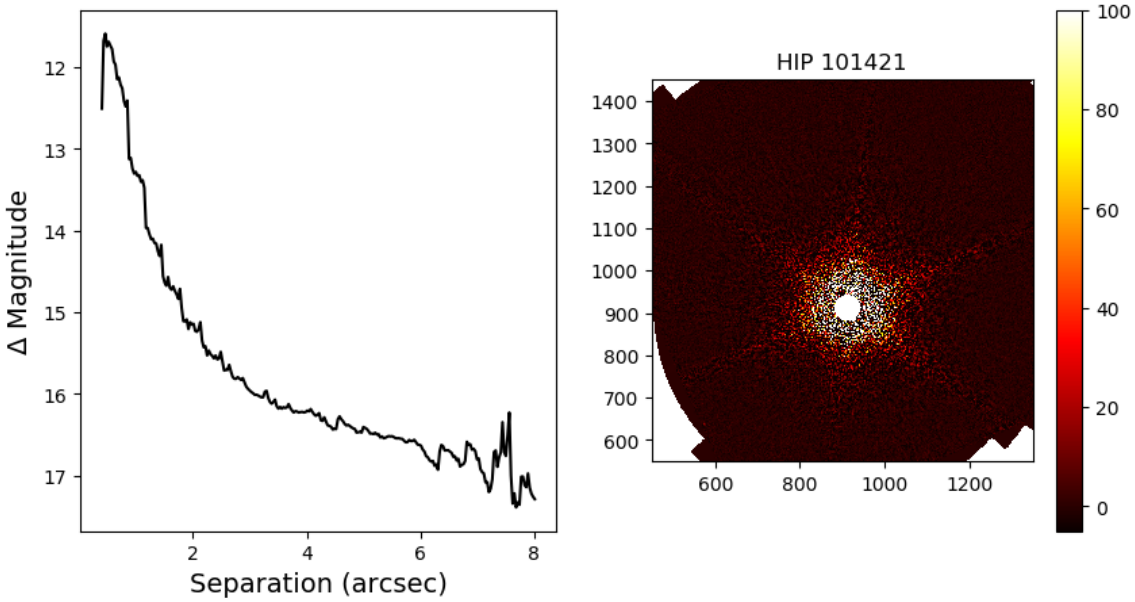
Δ Magnitude
Separation (arcsec)
HIP 101421

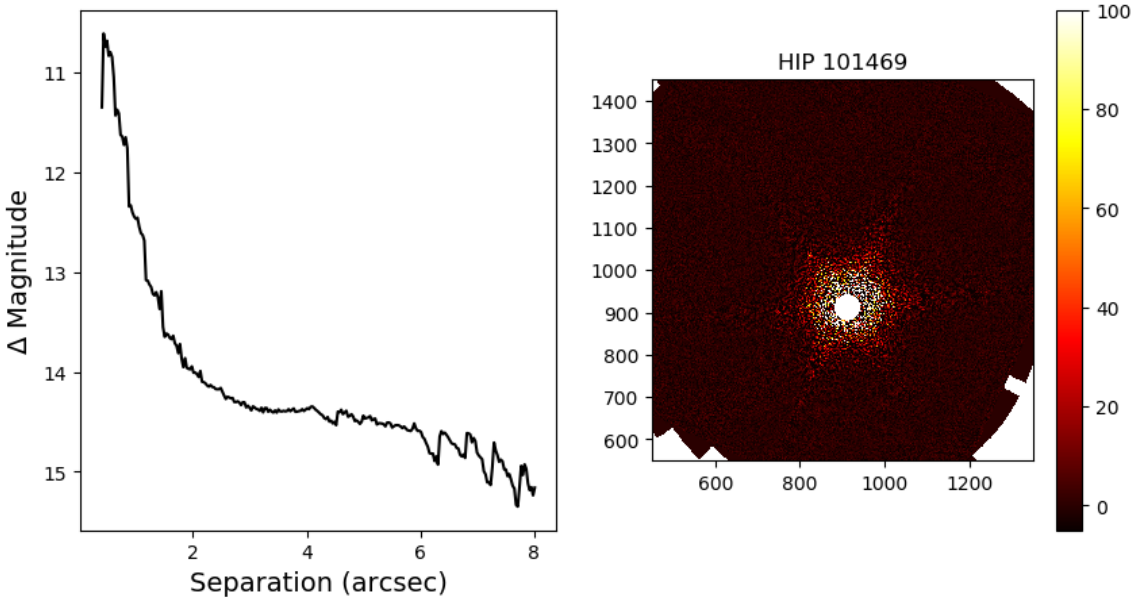
Δ Magnitude
Separation (arcsec)
HIP 101469

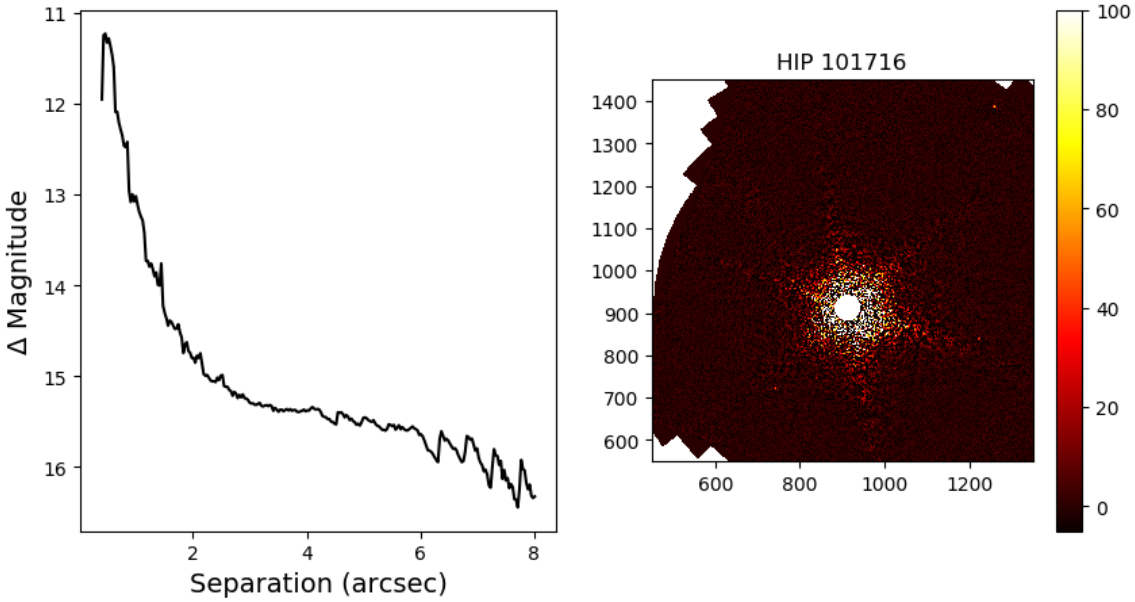
Δ Magnitude
Separation (arcsec)
HIP 101716

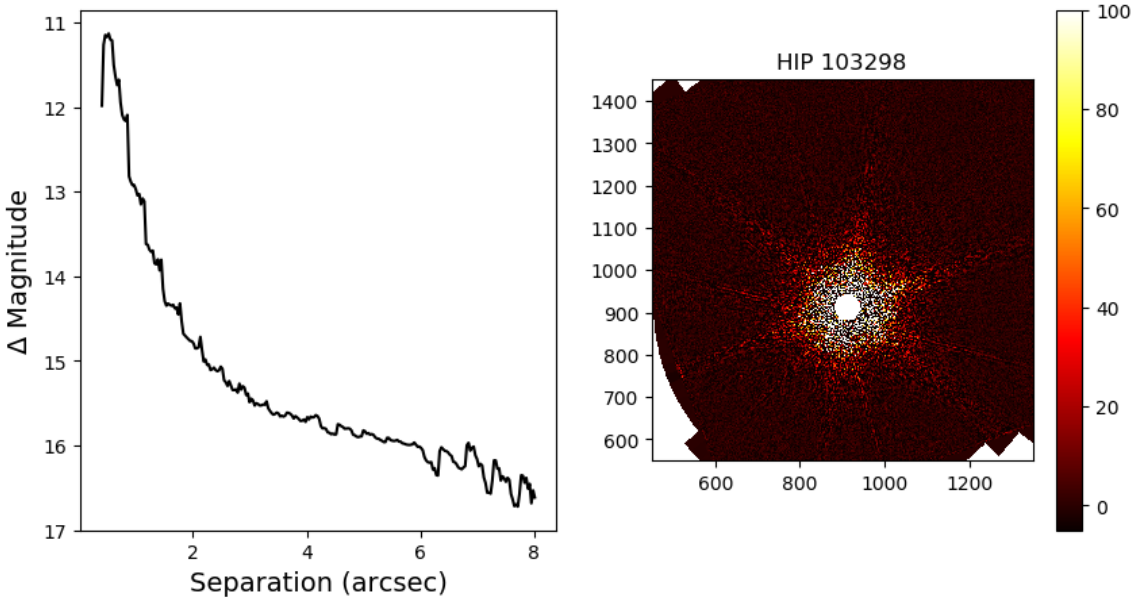
Δ Magnitude
Separation (arcsec)
HIP 103298

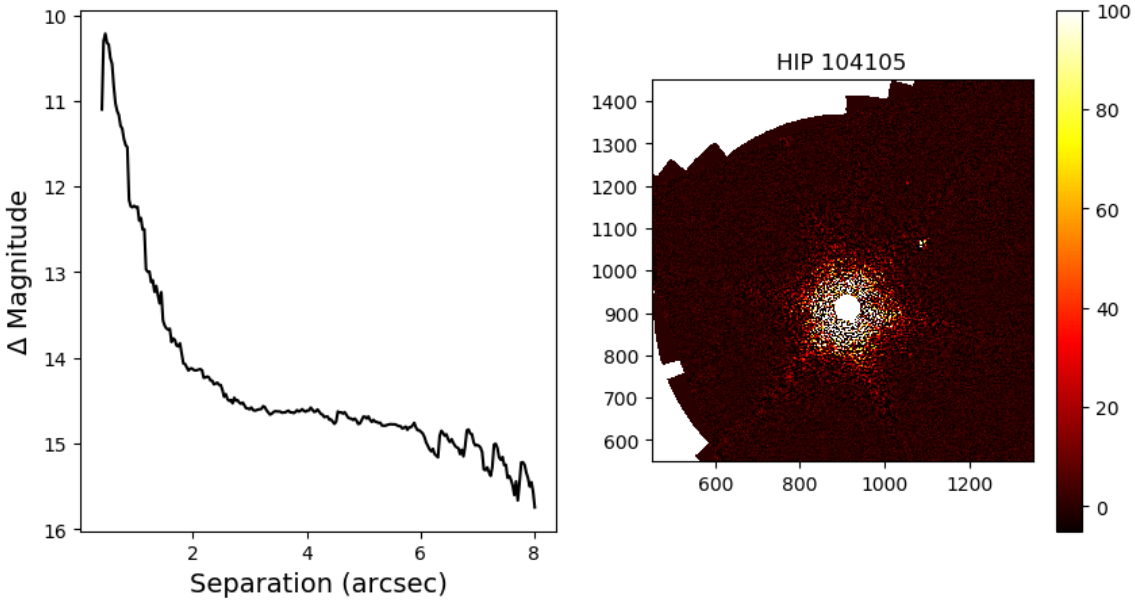
Δ Magnitude
Separation (arcsec)
HIP 104105

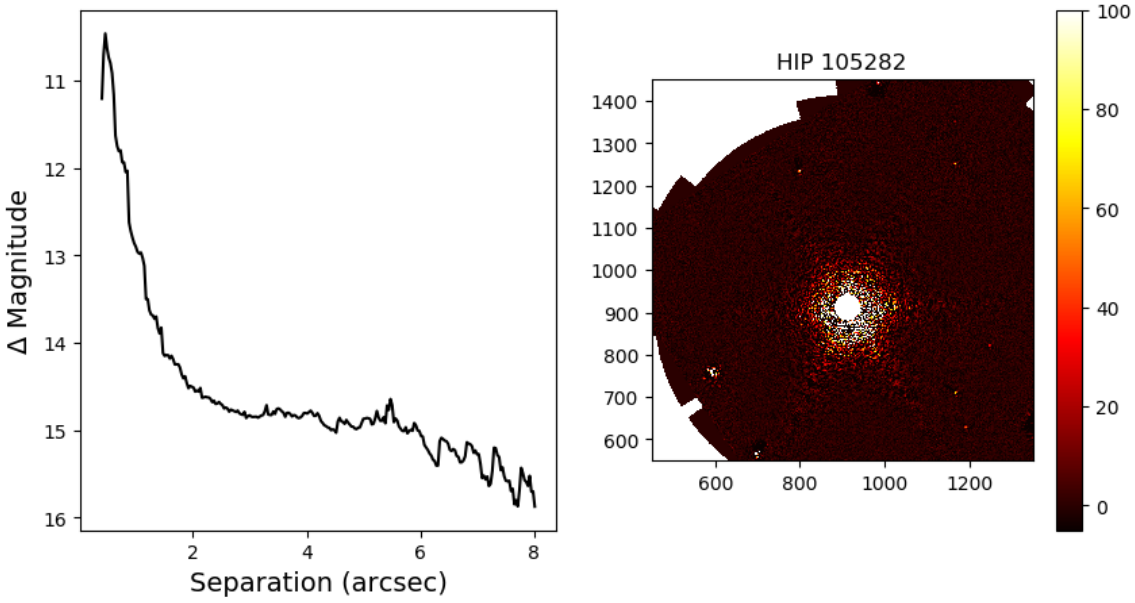
Δ Magnitude
Separation (arcsec)
HIP 105282

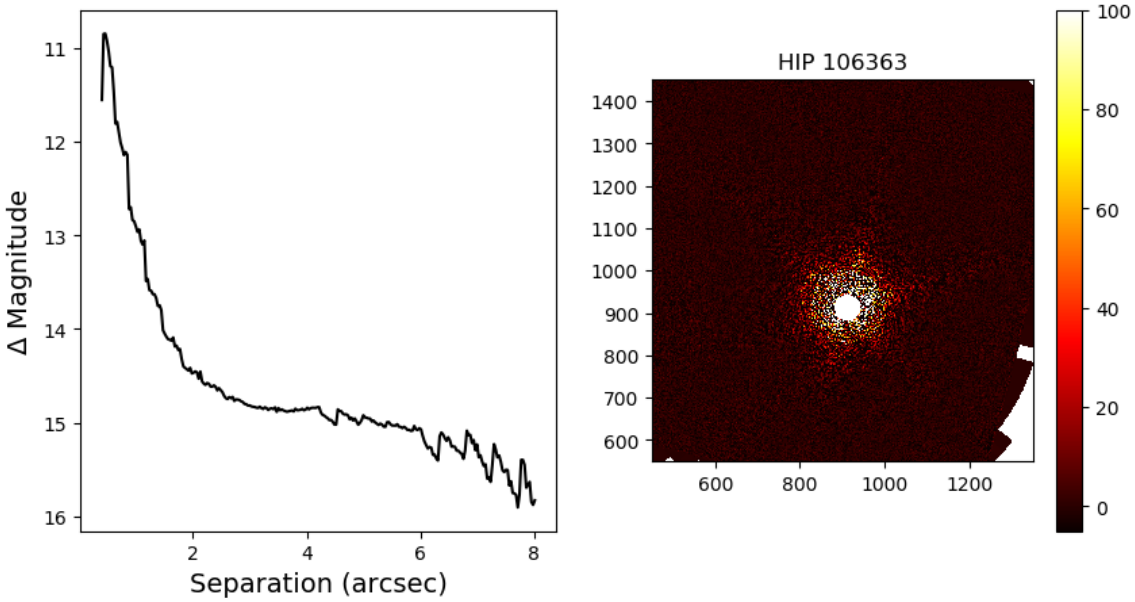
Δ Magnitude
Separation (arcsec)
HIP 106363

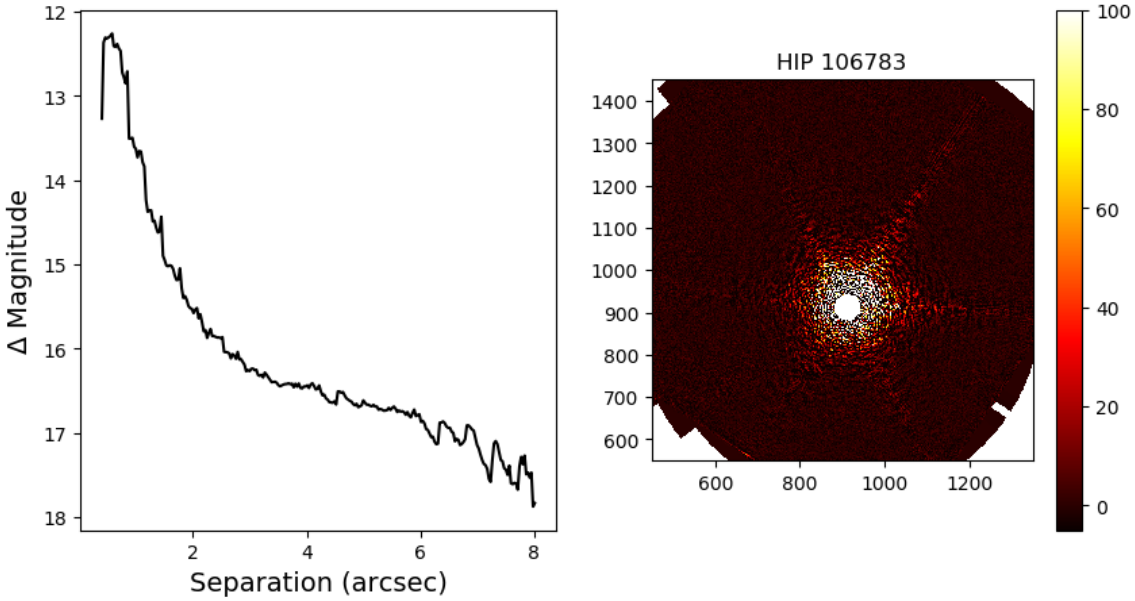
Δ Magnitude
Separation (arcsec)
HIP 106783

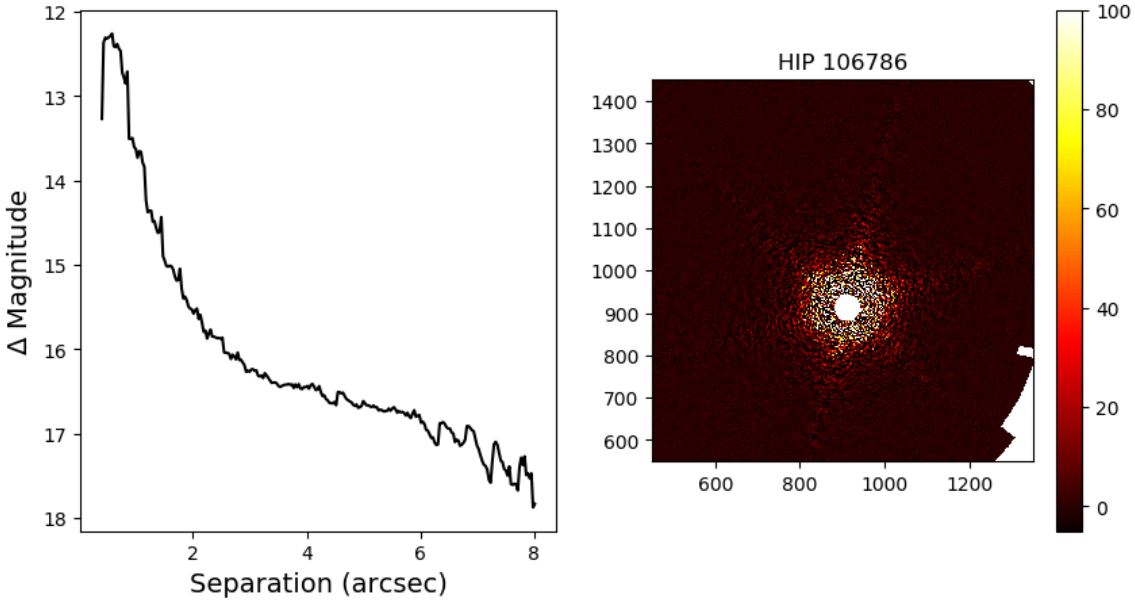
Δ Magnitude
Separation (arcsec)
HIP 106786

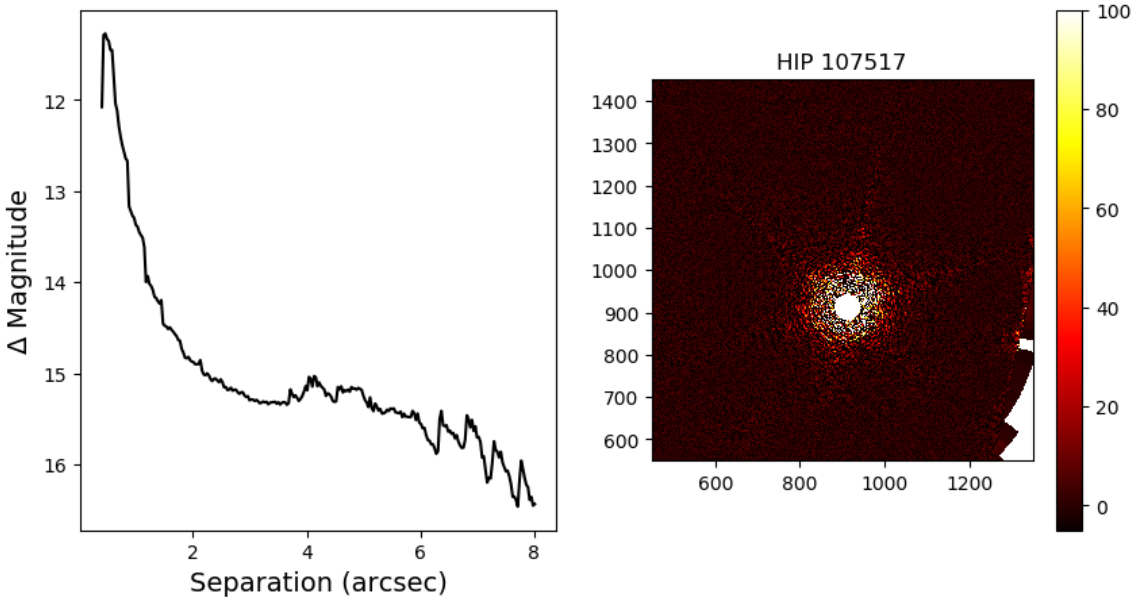
Δ Magnitude
Separation (arcsec)
HIP 107517

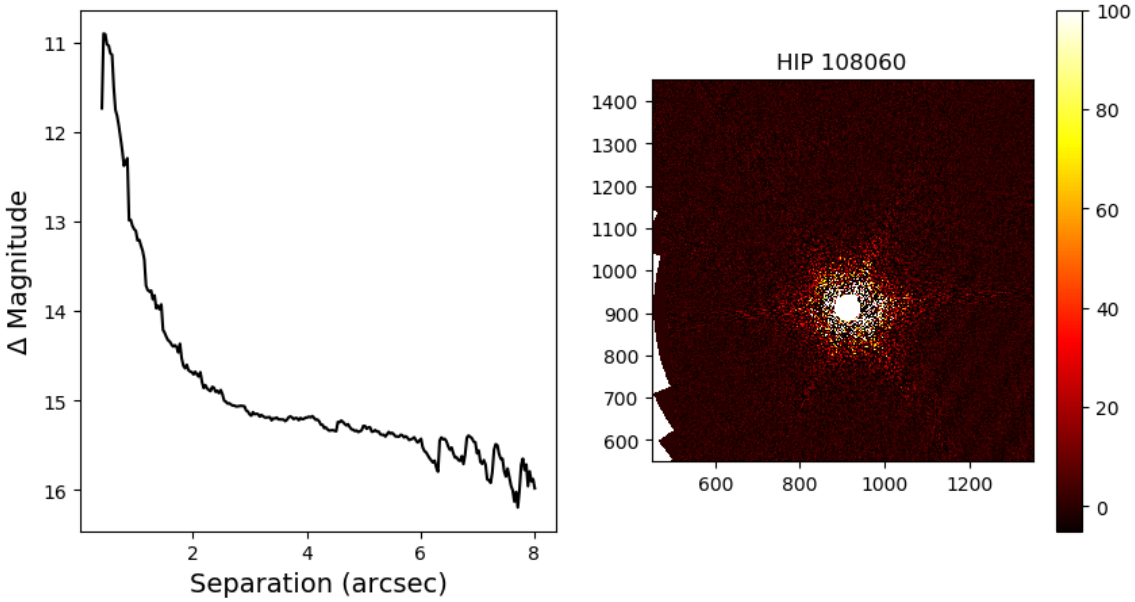
Δ Magnitude
Separation (arcsec)
HIP 108060

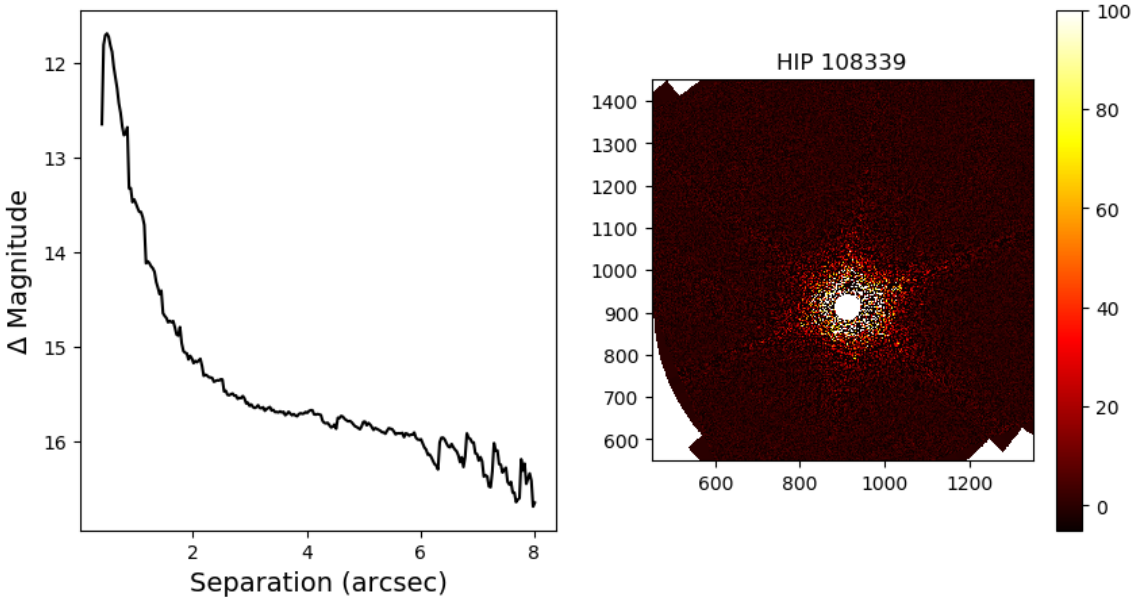
Δ Magnitude
Separation (arcsec)
HIP 108339

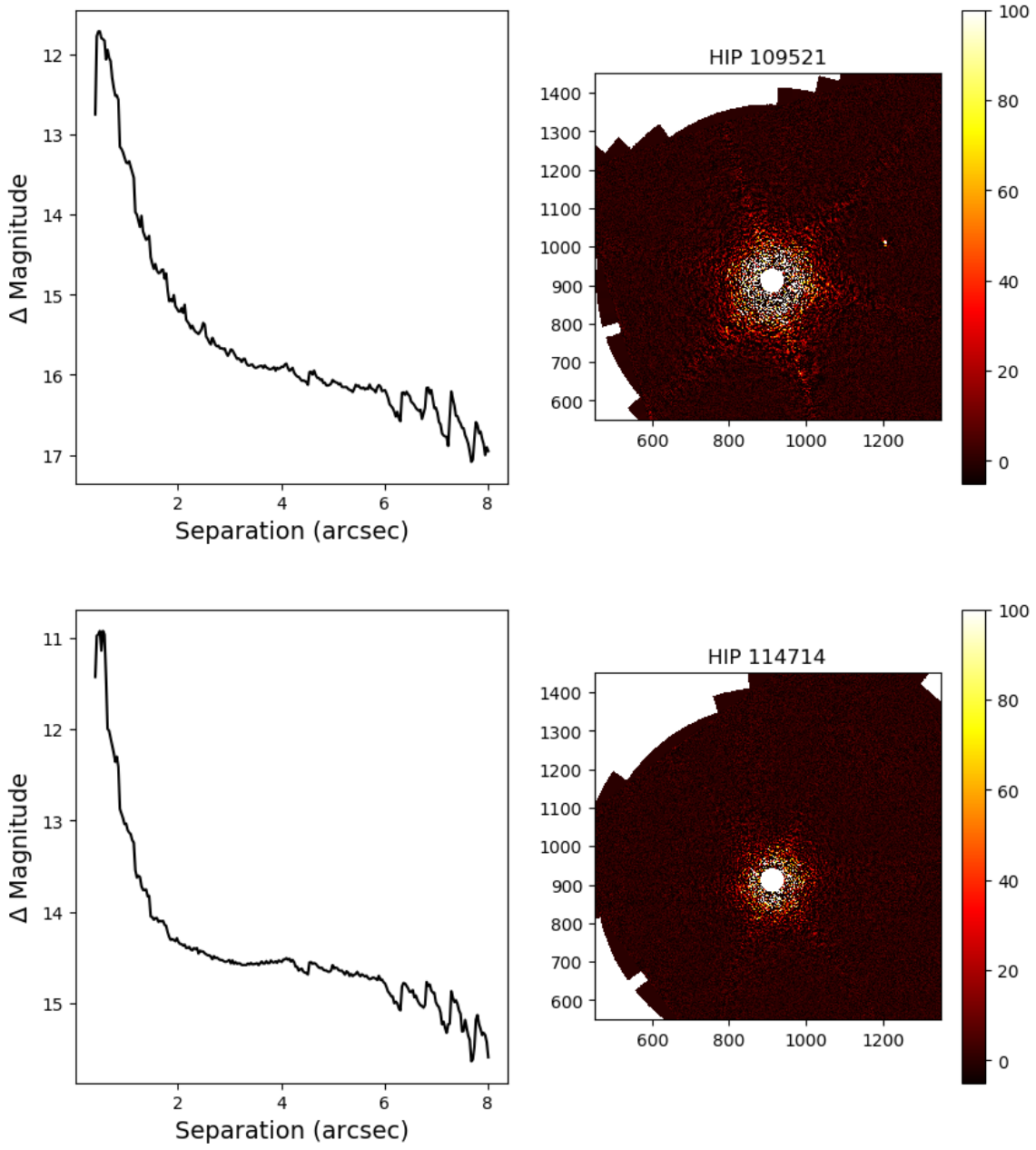

Figure C.1: Contrast curves and final images for all fully reduced, unsaturated stars from 04 June 2014.